ISSN 1991-1696

Africa Research Journal

Research Journal of the South African Institute of Electrical Engineers

Incorporating the SAIEE Transactions

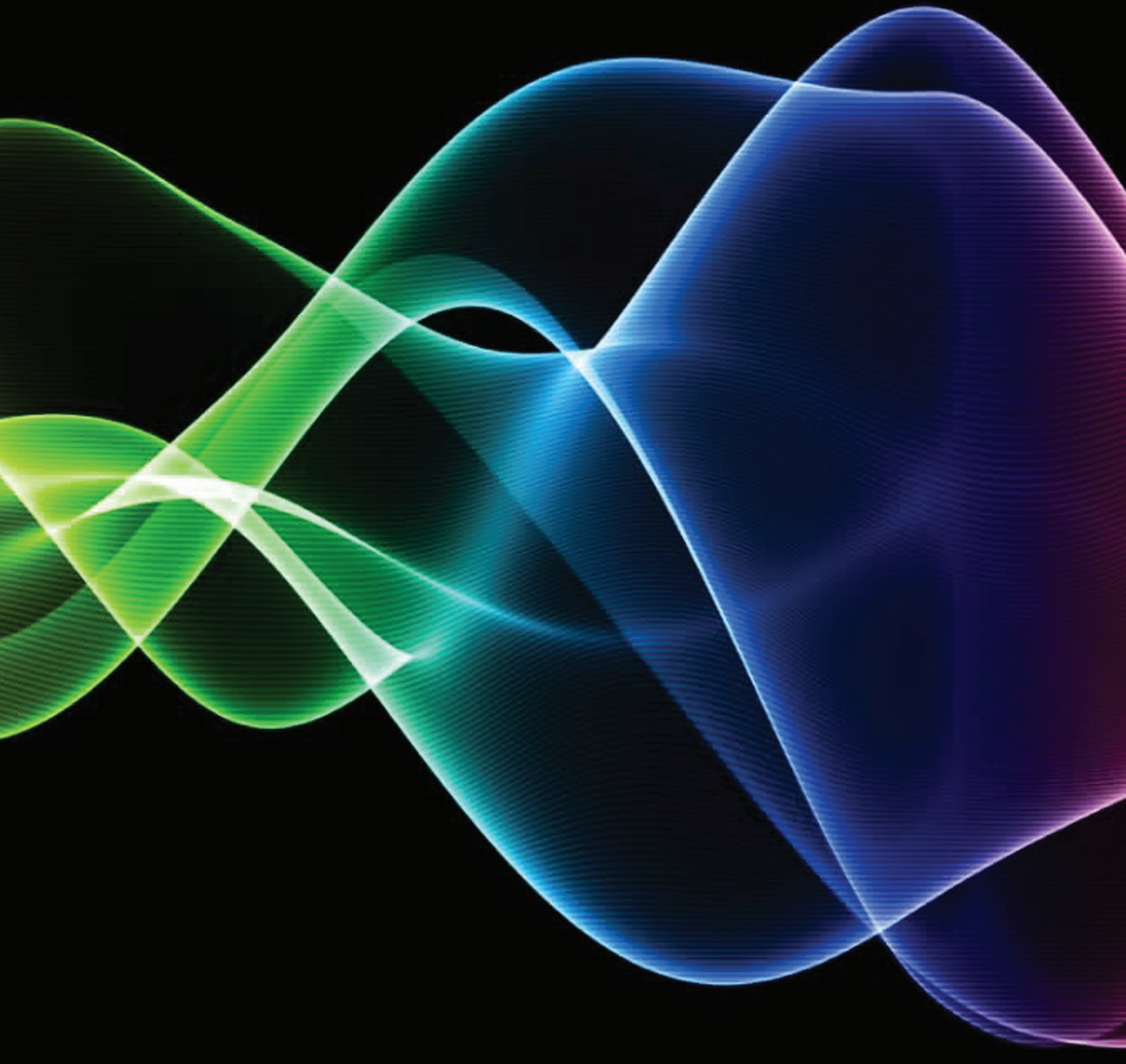

December 2015
Volume 106 No. 4

www.saiee.org.za

SAIEE AFRICA RESEARCH JOURNAL

(SAIEE FOUNDED JUNE 1909 INCORPORATED DECEMBER 1909)
AN OFFICIAL JOURNAL OF THE INSTITUTE

ISSN 1991-1696

Secretary and Head Office
Mrs Gerda Geyer
South African Institute for Electrical Engineers (SAIEE)
PO Box 751253, Gardenview, 2047, South Africa
Tel: (27-11) 487 3003
Fax: (27-11) 487 3002
E-mail: researchjournal@saiee.org.za

Published by
South African Institute of Electrical Engineers (Pty) Ltd, PO Box 751253, Gardenview, 2047
Tel. (27-11) 487 3003, Fax. (27-11) 487 3002,
E-mail: researchjournal@saiee.org.za

Additional reviewers are approached as necessary
ARTICLES SUBMITTED TO THE SAIEE AFRICA RESEARCH JOURNAL ARE FULLY PEER REVIEWED PRIOR TO ACCEPTANCE FOR PUBLICATION
The following organisations have listed SAIEE Africa Research Journal for abstraction purposes:
INSPEC (The Institution of Electrical Engineers, London); 'The Engineering Index' (Engineering Information Inc.)

VOL 106 No 4
December 2015

SAIEE Africa Research Journal

A MEASUREMENT SYSTEM TO RECORD THE ULF ELECTRIC FIELDS RELATED TO THE ELASMOBRANCH ELECTROSENSORY SYSTEM

G. J. Gibbon*

* *School of Electrical and Information Engineering, Private Bag 3, Wits, 2050, South Africa. Email: gibbon@icon.co.za*

Abstract: Numerous observations and reports indicate that sharks are often attracted to, or repelled by, the Electromagnetic (EM) Radiation from underwater electrical apparatus and man-made installations resulting in damage to the equipment and possible ecological damage. It is essential that, with the introduction of more and more man-made underwater devices, a study of "normal" electric activity in the oceans is made so this can be compared with possible increased activity from man-made systems. In this paper the development, design and implementation of an underwater electric field recorder that can be towed by a scuba diver is presented. The measurement system uses carbon fibre probes to measure three channels in the frequency range of 0.1 - 10 Hz at 64 samples/sec with a resolution of 24 bits. The input range is ± 18 mV/m with a noise floor of less than ± 30 μV/m. The system can record for up to one hour and the measurements are downloaded to a computer for analysis.

Key words: Marine electromagnetics, measurement systems, ULF, *Elasmobranch*, sharks, EM radiation, modelling.

1. INTRODUCTION

Numerous observations and reports indicate that sharks are often attracted to, or repelled by electric fields from underwater electrical apparatus and man-made installations [1]. This results in either damage to the apparatus or possible ecological damage as sharks have been reported to leave areas of high unnatural EM activity [2]. Adverse reactions by sharks to strobe flashes, video cameras and protection systems have been reported, as well as an interest in underwater electrical equipment, such as video cameras [1], SONAR arrays and telecommunication equipment [3]. This can cause "distress" to both sharks and humans (when their equipment is "attacked") and could also result in a possible decline of marine resources and tourist activities.

Renewable energy resources in the marine environment, such as offshore wind farms, tidal generators and wave generators [4, 5], could also result in unintentional ecological damage to the habitat of electrosensory fishes. Electric potentials in the marine environment are caused by ocean flow through the earth's magnetic field, non-ocean origins (geomagnetic, atmospheric and ionospheric), man-made (naval, industrial and recreational) and oceanic life [6–9]. To evaluate the possible ecological problems that may be caused by man-made equipment and electrical installations on the elasmobranchii, some idea of the "normal" electric potentials that they are subjected to must be determined.

In this paper the design and construction of a recording system to measure Ultra Low Frequency (ULF) electric potentials in the water is described. Results of the measurements are presented and analysed in terms of both the possible sources and the elasmobranchii' electrosensory system.

2. SOURCES OF ELECTRIC POTENTIALS

2.1 Natural sources

Ridgway *et al.* [6] describes the natural sources as being both internal to the ocean, caused by movement of the sea water through the earth's magnetic field, and external, caused by electromagnetic radiation produced from geomagnetic, atmospheric and ionospheric activity. Electric potentials produced by swells and surface waves, caused by local winds, have frequencies in the range of 50 to 500 mHz. As discussed by Crona *et al.* [8] the background electric fields can be denominated by electromagnetic waves caused by micropulsations in the ionosphere. In shallow-water Schumann resonances, lightning induced random phase standing waves in the ionosphere-earth cavity, have discrete peak frequencies of 8, 14, 20, 26, ... Hz. Spectral analysis from measurements taken by Crona *et al.* [8] off the western shore of Point Loma, San Diego clearly show Schumann resonances and swells in the frequency range 40 mHz to 1.8 Hz. Similar results were obtained by Sanford [9], again off the coast of San Diego.

2.2 Man-made sources

To attempt to quantify or even describe all the man-made electromagnetic sources producing electric potentials in the worlds' oceans is an impossible task. The man-made sources include:

- power-line frequencies as measured by both Crona *et al.* [8] and Sanford [9]

- shipping activity
- marine cathodic protection systems
- offshore drilling rigs
- oil pipelines
- electromagnetic surveying [10]
- telecommunication systems [3]
- naval activity both for submarine communication and warfare systems [11, 12]
- scuba diving equipment and accessories [1].

Much of the work is being conducted at military and commercial levels resulting in few of the publications being available for general access.

3. ELASMOBRANCHII' ELECTROSENSORY SYSTEM

The elasmobranchii electrosensors were first described by Lorenzini in 1687 [13] but their purpose as electrosensors was first reported by Dijkgraaf and Kalmijn in 1962 [14]. Since then a number of researchers have undertaken research programmes to model the electrosensory systems of the elasmobranchii. This includes laboratory and open water experiments [15, 16], Bastian [17] developed a model for the equivalent circuit of the system, Tricas [18] measured the sensitivity and dynamic response and Bodznick *et al.* [19] investigated the filtering of important information from a very noisy environment. The sensitivity the electrosensory system can be less than 1 μV/m [20] with a frequency range of DC to 10 Hz [16].

4. DESIGN OBJECTIVE

The design objective was to develop a system to measure the electric potentials in a recreational scuba diving environment in the sensitivity and frequency range of the elasmobranchii. The goal was to quantify and compare the electric fields produced by divers and the equipment, usually used during recreational dives, and those found without divers present. Ultimately this information could be used to design low emission equipment, thus reducing recreational divers' impact on the marine environment.

Initially a laboratory measurement system was developed, with three dimensional carbon fibre probes and low noise amplifiers to measure voltages in a salt water tank housed within a screened building [1, 21]. Carbon fibre probes were used for both the laboratory and the self contained underwater measurement system in preference to silver/silver chloride (Ag/AgCl) electrodes. Carbon fibre electrodes are more robust, easy to manufacture at a lower cost and perform as well as Ag/AgCl electrodes [22]. The electric fields from an underwater video camera, strobe flash and a dive computer were measured to get an idea of both the voltages and frequencies produced by the equipment. These results were then modelled [23] and used as the basis to design the underwater recording system.

5. LABORATORY MEASUREMENTS

No change in measurements was recorded from the dive computer whereas changes in the measured potentials were obtained from both the strobe flash and the video camera. The measurement system and results are fully described by Zachar and Gibbon [21]. A typical measurement from a strobe flash is shown in Figure 1 and shows a distinct change in the measured potentials when the flash was fired.

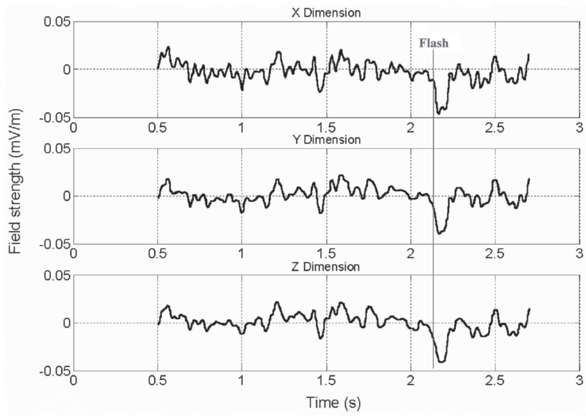

Figure 1: Measurements of a strobe flash discharge

Figure 2 shows voltages measured in the tank with (a) nothing in the water, (b) video camera, switched off (c) video camera, switched on and (d) video camera, in recording mode.

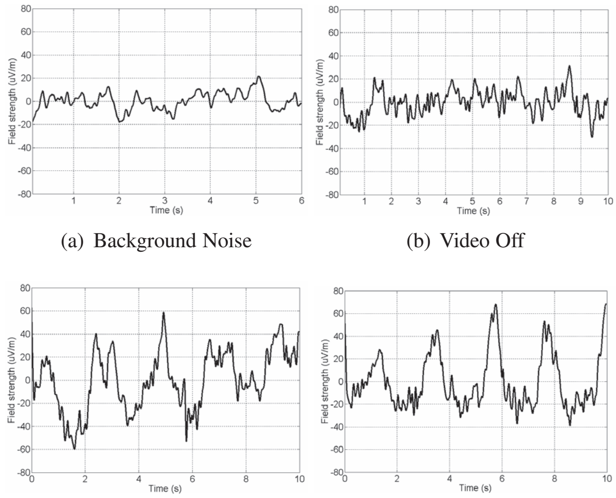

(a) Background Noise (b) Video Off

(c) Video On (d) Record On

Figure 2: Amplitude measurements with the Video Camera

Although clear changes can be seen in the time variant signals, more significant changes are apparent in the frequency content of the four recordings, as shown in Figure 3. Please note that the plots have different y-axis scales to enable discussion of the frequency in each mode of operation as follows:

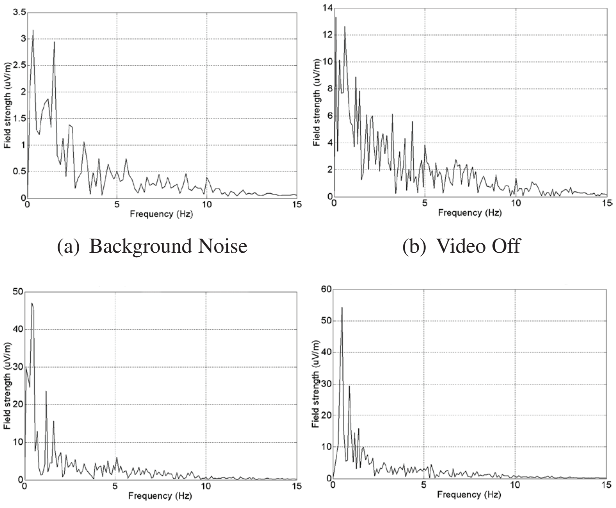

(a) Background Noise (b) Video Off

(c) Video On (d) Record On

Figure 3: Frequency response of measurements with the Video Camera

- The amplitude of signals at frequencies below 1 Hz increase by 17 times when the video camera was placed in the water. This probably due the ionisation caused by the different materials from which the housing is manufactured (stainless steel, powder coated aluminium and various plastics).
- Amplitudes increase at frequencies above 1 Hz when the camera is switched on, most likely due to radiation from the power supply and electronic circuits.
- In the record mode increased amplitude can be seen further up the frequency spectrum as a result of added radiation from the tape drive motors and controlling circuits.

Sharks will, in all probability, be aware of these changes in frequency content due to their adaptive frequency capability [19].

6. SELF-CONTAINED UNDERWATER MEASUREMENT SYSTEM

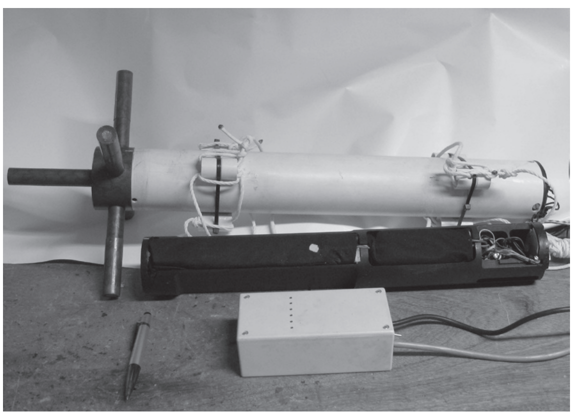

Figure 4: The underwater recording system showing the housing, internal structure and computer interface

A recording system was developed to measure electric field strengths in the ocean (see Figure 4) compact enough to be "towed" by a scuba diver on a recreational dive. The system was based on a modified electrical representation of the sharks' sensory system [1], shown in Figure 5, together with notes on how this was implemented in the recording system. The specifications of the system are given in Table 1. The system uses chopper-stabilised input amplifiers and carbon fibre probes to eliminate input drift due to ionisation in the water. Unity gain chopper-stabilised amplifiers, with a switching frequency of 200 Hz, (TC7650 [24]) were used for the input stage to minimise the input offset voltage and drift, input bias current and input noise voltage. There are no metal fittings on the casing to avoid any interference from cathodic reactions.

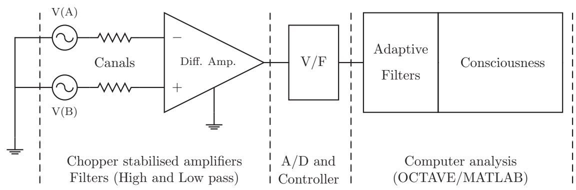

Figure 5: Electrical model of the underwater measurement system

Table 1: **Specifications of the underwater measurement system**

Number of channels	:	3 (x,y and z)
Frequency Response (-3dB)	:	0.1 - 10 Hz
Alias noise	:	-50 dB at 32 Hz
Sample Rate	:	64 samples/sec
Sample size	:	24 bits
Recording time	:	60 minutes
Input range	:	$\pm 18\,\mathrm{mV/m}$
Internal noise	:	$< \pm 30\mu\mathrm{V/m}$
Interface to computer	:	SD card interface

6.1 Results

Measurements were taken off the coast of Port Alfred, Eastern Cape, South Africa. These included five drifts over sand, over sandstone reefs, "deep sea" drifts at 30 m with the sea bottom at 70 m, to measure electric potentials without divers, and 27 dives with a varying number of divers. Two typical recordings are discussed.

Figure 6 shows the electric field measurements and frequency response taken during a drift 5.6 Nautical Miles (NM) off the coast with the recording system hanging from a buoy at 30 m with the sea floor at 70 m. The first 2.5 minutes show electrical activity after the recording system was dropped into the water, probably due to its movement through the water to 30 m and its close proximity to the boat. The spectral power density analysis is calculated relative to the maximum signal recorded and was plotted to -120 db(max) to indicate the noise floor of the recording system.

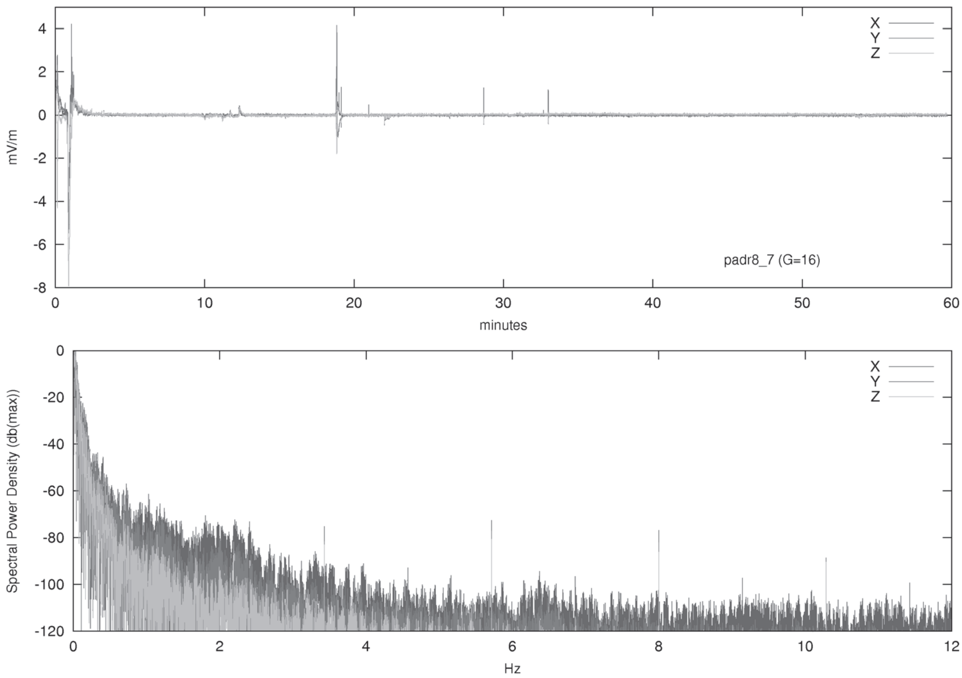

Figure 6: Recordings from an open water drift: depth 30 m, sea bottom at 70 m

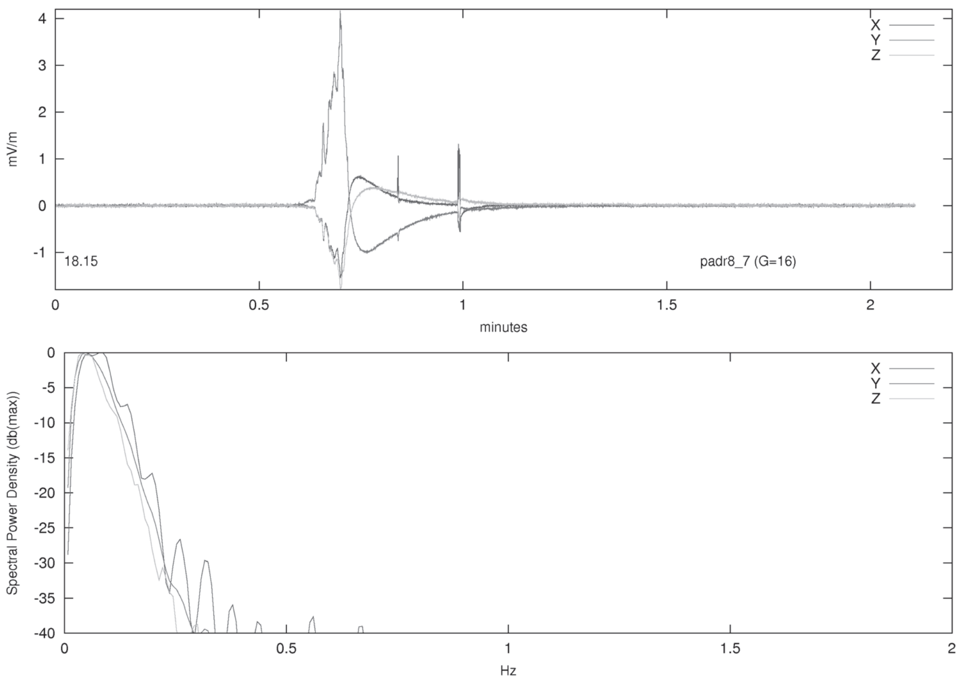

Figure 7: A large pulse measured during the open water drift

Figure 7 shows an expanded section of the large pulse at about 19 minutes. No definite theory is offered for this signal but observations of the buoy changing direction at approximately that time, during the drift, suggest that the measurement system passed through opposing currents with change in water temperature.

Figure 8 shows an expanded section of another pulse, at about 28 minutes, which is typical of measurements taken during most of the drifts and dives recorded off Port Alfred. Interestingly this pulse is almost the same as a pulse recorded by Sanford *et al.* [9] which Sanford suggested could have been caused by a "marine mammal disturbance" although this was not actually observed. These pulses have been recorded during dives where no interaction with marine life was observed and the author

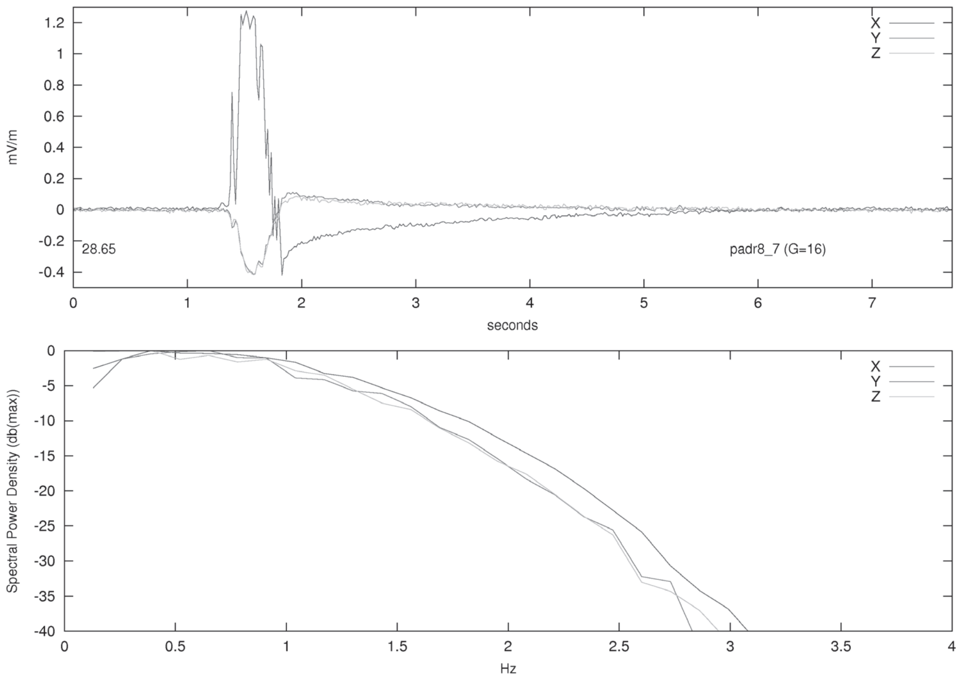

Figure 8: A typical signal measured during an open water drift

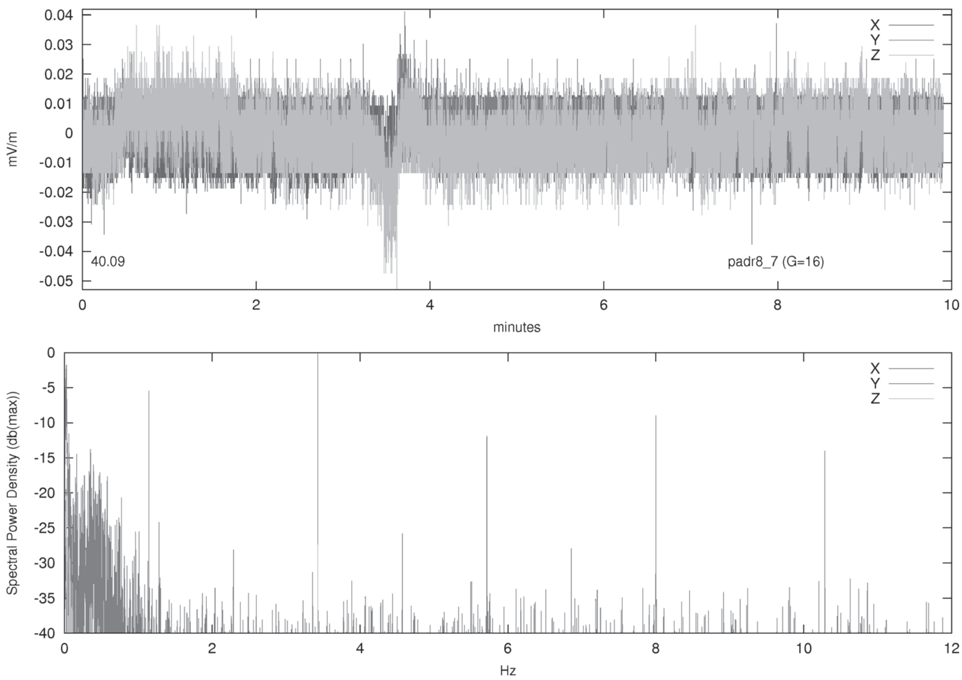

Figure 9: A typical quiet section recorded during open water drift

believes that this maybe related to the system passing through thermoclines or water bodies with dissimilar properties.

Figure 9 shows a "quiet" section during the drift with signals below $50\,\mu\mathrm{V/m}$ being measured with no distinctive signals. The spikes seen at regular intervals from about 0.8 Hz are due the sampling rates of the analogue-to-digital converter and the switching frequency of the chopper-stabilised amplifiers. This noise can be removed, if necessary, during analysis as the peaks are at known frequencies. The low frequency content, below 0.5 Hz, can be explained by the swell and wave action that was present, and is always present, while the measurements were being taken.

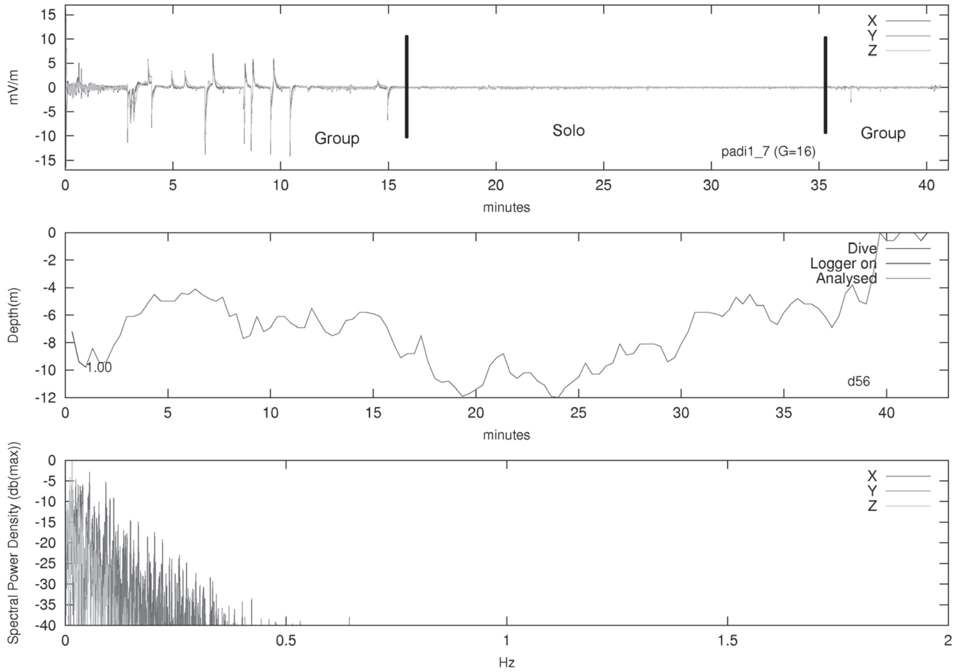

Figure 10: Measurements taken during a dive with up to twelve divers

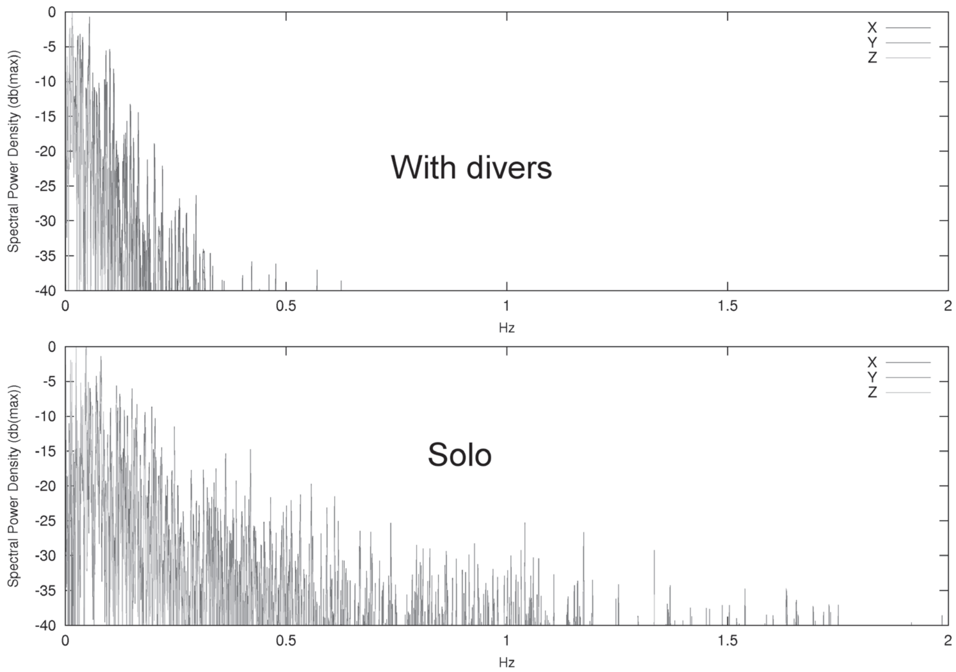

Figure 11: The frequency spectra measured, with and without other drivers near the recording system, during a dive

Figure 10 shows measurements during a dive with a group of 12 divers showing the recorded voltages, the dive profile and the frequency spectrum. Initially the recording system was amongst the divers and at about 15 minutes was moved away from the group and towed at a minimum distance of 5 m from the group. The group was rejoined at 35 minutes for the ascent. From the measurements it appears that groups of divers radiate electric signals into the water at frequencies and amplitudes well within the sharks' sensory range.

In Figure 11 the frequency spectrum of the measurements with and without other divers in the vicinity of the recording system are compared. It should be noted that the scales of the two plots are not comparable as the frequency power density (db(max)) is calculated with the maximum signal in the section being analysed, as with this method it is easier to visualise the frequency spectrum where there are large variations in the voltages being measured. The plots do show, however, that there are more lower frequencies signals produced by a group of divers, in the range DC to 0.5 Hz, as opposed to those produced by a single diver. None of the divers were using any electronic equipment, other than dive computers, and the signals were produced by passive sources such as air cylinders, buoyancy compensators, breathing systems and their bodies.

7. DISCUSSION

One of the problems of analysing the measurements is the separation of far-field events, such as those caused by wave action and ionospheric events, and near-field events, such as diving equipment. The elasmobranchii have adapted to live with the considerable natural electric noise in the sea but do react to near-field disturbances such as camera strobe flashes [1]. One of the solutions is a remote reference system as used by Crona *et al.* [8] where common signals can be removed and only the remaining signals studied. In Crona's case the reference system was placed 1.8 km from the measurement system. This is not a feasible option for a system designed to accompany a diver on many dives at many dive sites. The elasmobranchii also do not have the option of a remote reference and seem to be able to distinguish between near-field and far-field events. It is possible that their "sensor arrays" enable them to ignore far-field events and work by Sisneros [25] and Tricas [26] may provide more information that may be used in the analysis of the measurements.

8. CONCLUSION

The design of, and the results obtained from, an underwater recording system to measure the electric potentials in sea water has been presented. The system has three channels with an input range is ± 18 mV/m, a frequency range of 0.1 - 10 Hz at 64 samples/sec, a resolution of 24 bits and a noise floor of less than ± 30 μV/m. The system was designed to be "towed" by a diver and record all the electric potentials produced by divers and their equipment during dives one hour. Laboratory results show distinct changes in both the amplitude and the frequency content of the measured potentials from both a strobe flash and a video camera. Measurements in the sea, both drifts and dives, show a surprisingly electrically noisy environment with some unexplained phenomena. The results also show large changes in both the amplitude and the frequency content in the electric potentials when a group of divers is compared to a single diver towing the recording system.

9. ACKNOWLEDGEMENTS

The author would like to thank both the University of the Witwatersrand, Johannesburg and the National Research Foundation (NRF) for past financial support, André Slade of Inner Space Developments for the design and manufacture of the housing for the measurement system and Keryn van der Walt and her team from Outdoor Focus, Port Alfred for all their support.

REFERENCES

[1] G. J. Gibbon, "Initial investigation into the influence that electrical SCUBA diving equipment has on the *Elasmobranch* family," in *2nd International Conference on Marine Electromagnetics, Brest, July 1999*. Brest: MARELEC, July 1999, pp. 407–415.

[2] E. K. Ritter, "Personal communication," July 1998, *eritter@greenmarine.com*.

[3] L. J. Marra, "Sharkbite on the SL submarine lightwave cable system: History, causes, and resolution," *IEEE Journal of Oceanic Engineering*, vol. 14, no. 3, pp. 230–237, July 1989.

[4] M. C. Öhman, P. Sigray, and H. Westerberg, "Offshore windmills and the effects of electromagnetic fields on fish," *AMBIO*, vol. 36, no. 8, pp. 630–633, 2007.

[5] A. B. Gill, Y. Huang, I. Gloyne-Philips, J. Metcalfe, Quayle, J. Spencer, and V. Wearmouth, "Cowrie 2.0 electromagnetic fields (emf) phase 2: Emf-sensitive fish response to em emissions from sub-sea electricity cables of the type used by the offshore renewable energy industry," Commissioned by COWRIE Ltd (project reference COWRIE-EMF-1-06). Copies available from: www.offshorewind.co.uk., Tech. Rep., 2009.

[6] J. Ridgway, M. L. Larson, C. H. Waldman, M. Gabbay, and R. R. Bunsten, "Analysis of littoral underwater electromagnetic data," in *Proceedings of the Marine and Electromagnetics Conference, London, March 2004*. London: MARELEC, March 2004.

[7] C. Cox, X. Zhang, S. Webb, and D. Jacobs, "Electro-magnetic fluctuations induced by geomagnetic induction in turbulent flow of seawater in a tidal channel," in *3rd International Conference on Marine Electromagnetics, Stockholm, July 2001*. Stockholm: MARELEC, July 2001.

[8] L. Crona, T. Fristedt, and B. Lundqvist, "Electric background fields in a shallow water environment off the coast of San Diego," in *Proceedings of the Marine and Electromagnetics Conference, London, March 2004*. London: MARELEC, March 2004.

[9] T. B. Sanford, "Ambient oceanic electric fields observed from a Langranian float," in *Proceedings of the Marine and Electromagnetics Conference, London, March 2004*. London: MARELEC, March 2004.

[10] H. Jones, S. J. Davidson, and P. Rawlins, "Development of a low noise electric field sensor

for measurement and ranging applications," in *Proceedings of the Marine and Electromagnetics Conference, London, March 2004*. London: MARELEC, March 2004.

[11] J. J. Holmes, "The future of marine electromagnetics," in *Proceedings of the Marine and Electromagnetics Conference, London, March 2004*. London: MARELEC, March 2004.

[12] J. B. Peddell, "The spectrum of marine electromagnetics: Advances through diversity," in *Proceedings of the Marine and Electromagnetics Conference, London, March 2004*. London: MARELEC, March 2004.

[13] H. H. Zakon, "Electroreceptors: Diversity in structure and function," in *Sensory Biology of Aquatic Animals*, J. Atema, R. R. Fay, A. N. Popper, and W. N. Tavolga, Eds. New York: Springer-Verlag, 1988, ch. 32, pp. 813–850.

[14] A. J. Kalmijn, "Electric and magnetic sensory world of sharks, skates and rays," in *Sensory Biology of Sharks, Skates and Rays*, E. S. Hodgson and R. F. Mathewson, Eds. Arlington: Office of Naval Research, USA, 1978, pp. 507–528.

[15] M. V. L. Bennett and W. T. Clusin, "Physiology of the ampulla of Lorenzini, the electroreceptor of the elasmobranchs," in *Sensory Biology of Sharks, Skates and Rays*, E. S. Hodgson and R. F. Mathewson, Eds. Arlington: Office of Naval Research, USA, 1978, pp. 483–505.

[16] A. J. Kalmijn, "Detection of weak electric fields," in *Sensory Biology of Aquatic Animals*, J. Atema, R. R. Fay, A. N. Popper, and W. N. Tavolga, Eds. New York: Springer-Verlag, 1988, ch. 6, pp. 151–186.

[17] J. Bastian, "Electrosensory organisms," *Physics Today*, vol. Feb, pp. 30–37, February 1994.

[18] T. C. Tricas and J. G. New, "Sensitivity and response dynamics of elasmobranch electrosensory primary afferent neurons to near threshold fields," *Journal of Comparative Physiology A*, vol. 182, pp. 89–101, 1998.

[19] D. Bodznick, J. Montgomery, and M. Carey, "Adaptive mechanism in the elasmobranch hindbrain," *The Journal of Experimental Biology*, vol. 202, pp. 1357–1364, 1999.

[20] M. V. L. Bennett, "Electroreception," in *Fish Physiology*, W. S. Hoar and D. J. Randall, Eds. New York: Academic Press, 1971, vol. V, Sensory Systems and Electric Organs, ch. 11, pp. 493–574.

[21] H. G. Zachar and G. J. Gibbon, "Measurement of electromagnetic fields produced by underwater equipment," in *2002 International Symposium on Underwater Technology*, Tokyo, Japan, 2002, pp. 149–153.

[22] L. Crona, T. Fristedt, P. Lundberg, and P. Sigray, "Field tests of a new type of graphite-fiber electrode for measuring motionally induced voltages," *Journal of Atmospheric and Oceanic Technology*, vol. 18, pp. 92–99, January 2001.

[23] N. D. Warren and G. J. Gibbon, "3-d modelling of electric fields of underwater electrical equipment in the marine environment," in *2002 International Symposium on Underwater Technology*, Tokyo, Japan, 2002, pp. 154–158.

[24] Microchip, "TC7650 Chopper Stabilized Operational Amplifier," Microchip Technology Inc., 2002.

[25] J. A. Sisneros and T. C. Tricas, "Neuroethology and the life history adaptations of the elasmobranch electric sense," *Journal of Physiology*, vol. 96, pp. 379–389, 2002.

[26] T. C. Tricas, "The neuroecology of the elasmobranch electrosensory world: why peripheral morphology shapes behaviour," *Environmental Biology of Fishes*, vol. 60, pp. 77–92, 2001.

INVESTIGATION INTO THE ROLE OF SINGLET OXYGEN IN POSITIVE CORONA IN AIR

A.G. Swanson* **and I.R. Jandrell***†

* *School of Electrical and Information Engineering, Faculty of Engineering and the Built Environment, Private Bag 3, Wits 2050, South Africa E-mail: andrewgswanson@gmail.com*

† *E-mail: ian.jandrell@wits.ac.za*

Abstract: Corona is the partial breakdown of air in a divergent electric field and is particularly evident around high voltage equipment. Air comprises of nitrogen and oxygen and the corona process involves many complex phenomena including ionisation, attachment and excitation and the interaction of the ions and excited molecules generated by these phenomena. A particular state of excited molecular oxygen, singlet oxygen, has the characteristic that it remains excited for a relatively long period of time. Singlet oxygen plays a role in the detachment of electrons from the negative oxygen ions and its role in corona discharges has been accounted for through theory and models, but due to the difficulties of measurement of the singlet oxygen, the influence it does have on corona discharges is not entirely clear. On this basis the gas processes associated with the corona discharge in air have been explored, where a Boltzmann equation solver, the electron energy distribution function, transport coefficient and Townsend coefficients are used to understand the phenomena and provide input to a gas discharge model, where the gases are representing as species in a drift-diffusion model. The model indicates the presence of negative ions and singlet oxygen, but clearly illustrates how the space charge plays the critical role in positive corona due to the collapse of the electric field. An experiment that involved altering the environment with air-flow produced an unexpected result in the positive onset streamers where the repetition rate changed considerably, initially it was thought that this was due to the removal of singlet oxygen. In an effort to determine if their was a relationship between repetition rate and singlet oxygen, experiments detecting the emission from singlet oxygen and exciting oxygen through a laser were undertaken. There was no evidence to suggest that the repetition rate of the positive onset streamers could be related to singlet oxygen. There were no emissions detected from various configurations, whilst visible corona was clearly seen. The experiment where laser induced excitation showed no change in repetition rate. It could be inferred that a relationship between repetition rate and that the detachment due to negative ions and singlet oxygen is not a dominant process in the corona discharge.

Key words: Corona, Positive onset streamers, Space charge, Singlet oxygen

1. INTRODUCTION

Corona in air is the partial breakdown of the gas in a sufficiently high electric field. For high voltage engineerings it is responsible for audio and radio interference and is a sign of poorly designed or degraded hardware or materials.

Air is predominantly made up of nitrogen and oxygen and corona occurring in air involves many complex phenomena including the production of space charge and excited molecular states of its constituents. Oxygen itself is an electronegative gas and has the ability to attach electrons. In the discharge process these phenomena combine to influence the electric field and the production of secondary electrons give corona its distinctive modes [1].

Positive corona involves electrons that are produced by natural means and move towards the high voltage electrode. This causes a number of reactions including ionisation, attachment and excitation and a subsequent collapse of the electric field. The process can only begin again when the space charge dissipates [1, 2]. The main difference with negative corona is that in negative corona the electrons are emitted upon positive ion bombardment with the electrode producing a supply of seed electrons are responsible for the repetitive nature of Trichel pulses, whereas positive corona has no such measurable mechanism to produce such seed electrons [1, 2].

Singlet oxygen, $O_2(a^1\Delta_g)$, is the lowest electronic excited state of oxygen and it has the characteristic that it remains in the excited state for a relatively long amount of time. Lowke proposed in his work that the singlet oxygen has a dominant role in the pre-breakdown corona and streamer process because of its ability to detach electrons from negative ions as given by the reaction [3, 4]:

$$O_2^- + O_2(a^1\Delta_g) = 2O_2 + e \tag{1}$$

An initial experiment was performed in [5] where the application of airflow to a point plane gap initially intended to alter the space charge produced an interested phenomena, where the low speed airflow significantly changed the repetition rate of positive onset streamers. This did not seem consistent with theory and considering the reaction in Equation (1), it was hypothesised that the removal of singlet oxygen was responsible [5].

The paper covers the investigation into the phenomena beginning with the physics of the mechanism, the modelling of the positive corona process and the experiments to ascertain if there is any influence of singlet oxygen on the repetitive nature of positive corona.

2. CORONA IN AIR

The fundamentals of the gas discharge are presented in this section where the basics of deriving the Townsend and transport coefficients is key to understanding the following sections.

2.1 *Collisional Cross-Sections*

Molecules in a gas are in constant random motion and are constantly colliding with other molecules leading to a distribution of velocity or energy given by the Maxwell-Boltzmann distribution [6]:

$$f(v) = \left(\frac{m}{2\pi k_B T}\right)^{\frac{1}{2}} \exp\left(-\frac{m v_i^2}{2 k_B T}\right) \qquad (2)$$

Where:

m = Mass of the particle [g]
k_B = Boltzmann's constant
T = Temperature [K]
v_i = Velocity of particle [m.s^{-1}]

Applying an external influence such as change in temperature or an electric field (Lorentz force) would alter this distribution.

All of the collisional reactions (elastic and inelastic) are based on a probability phenomenon related to the energy (or velocity) of an electron and a collisional cross-section, σ, for each type of reaction [6].

The collisional cross-sections for nitrogen and oxygen are illustrated in Figure 1 and Figure 2. The cross-sections are based on the data collated by Itikawa [7–10]. The figure illustrates only the momentum, electronic excitation and ionisation cross sections. The data from the LXcat database, which is used for Bolsig+, is similar [11, 12].

It is evident that for an electron with any given energy that there are a number of reactions that could take place where the most likely is the momentum collision for the whole range of energies. As the electron energy increases the ionisation cross-section tends towards the momentum cross-section. There are multiple excited states of nitrogen, which act as energy sinks and is the reason it is often considered a good insulator, as these excited states retard the growth of a streamer. There are fewer excited states for oxygen when compared with nitrogen, there is however the additional attachment cross-section. It is evident that attachment is in a lower energy region of the graph when compared to the ionisation. Importantly singlet oxygen, a$^1\Delta_g$, has a cross-section that is spread over a wide range of energies.

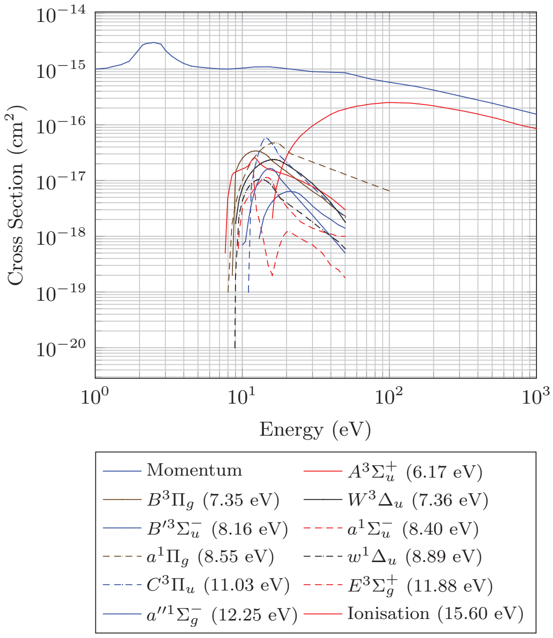

Figure 1: Collisional cross sections of nitrogen

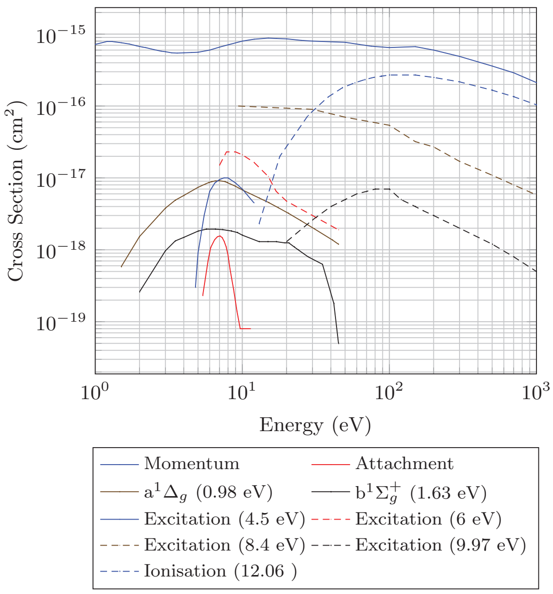

Figure 2: Collisional cross sections of oxygen

2.2 *Townsend and Transport Coefficients*

The Townsend and transport coefficients (mobility and diffusion) are derived from the cross-sections through the Boltzmann equation solver, Bolsig+ [13].

The Townsend coefficients and mean energy for an applied electric field are illustrated in Figure 3. The coefficients match well with published data [14]. It is seen that singlet oxygen has a relatively high Townsend coefficient indicating that singlet oxygen will be produced for wide range of applied electric fields. For a phenomena such as corona where there is a non-linear electric field this indicates the singlet oxygen will be produced over the entire region.

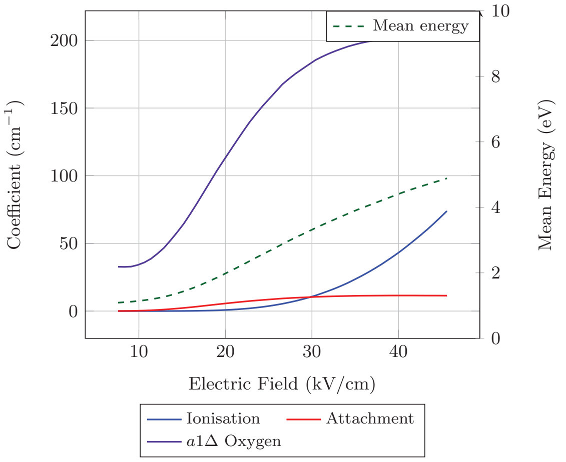

Figure 3: Townsend coefficients and mean electron energy for an applied electric field

2.3 *Positive Corona*

Positive corona is initiated by electrons that are freed due to natural processes in the air. The electron avalanche develops towards the electrode in an increasing electric field. The highest ionisation activity occurs near the conductor surface where the electric field is the highest [1, 2]. Clouds of space charge are formed which consist of mostly positive ions near the conductor and relatively small amounts negative ions away from the conductor as electrons are neutralised closer to the conductor. These space charge clouds modify the electric field and the discharge development leading to the modes of corona including Burst Corona, Onset Streamer, Positive Corona and Breakdown Streamer [1, 2].

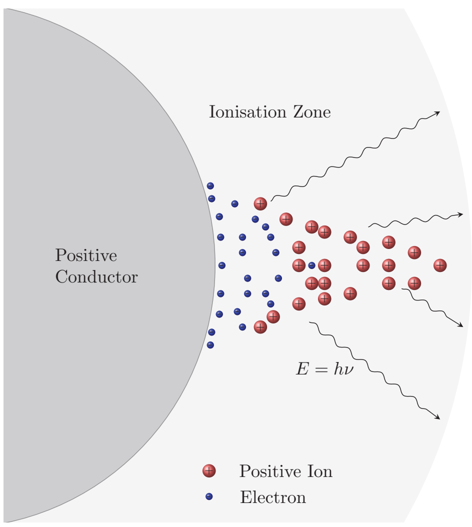

Figure 4: Positive corona

Burst corona occurs at the onset of positive corona where electrons lose their energy due to ionisation activities before they get absorbed by the conductor. The discharge directs radially outwards from the electrode. Positive ion space charge cloud is formed around the conductor which suppresses the discharge. The spread of electrons then moves to another part of the conductor. As the ionisation spreads around the conductor and is suppressed by the space charge cloud a positive corona current pulse is produced [1, 2].

Onset streamers result from radial development of the discharge. A large amount of positive ion space charge is left behind by electron avalanches and this space charge cloud enhances the electric field away from conductor, causing successive avalanches. The positive ion space charge cloud created from the avalanches reduces the electric field near the conductor surface and suppresses the streamer. When the space charge cloud is cleared, the original field is restored and the cycle repeats itself. The onset streamers have a pulse amplitude from a few milliamps to a few hundred milliamps, and the repetition rate increases with the voltage up to a critical point where it is then suppressed by the negative charge and the mode changes to glow. Positive onset streamers are the main source of radio interference and audio noise on transmission lines [1, 2]. The typical measured positive onset streamer pulse is illustrated in Figure 5.

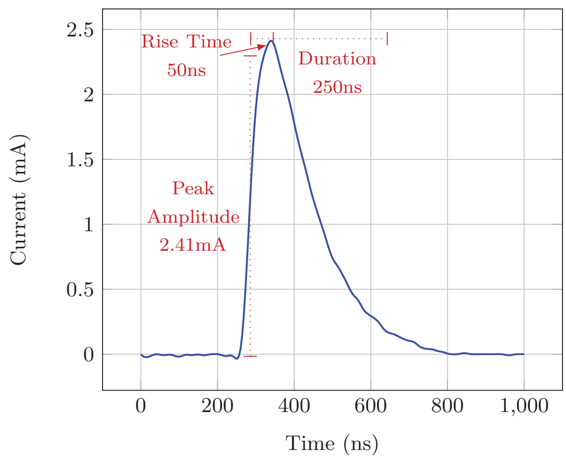

Figure 5: Positive onset streamer

Positive glow corona does not have a pulsating nature and occurs under a particular condition of production and removal of positive ions, where the field distribution allows for the rapid removal of positive ions while not allowing for the development of discharges and streamers. Glow corona manifests itself as a thin luminous layer over the conductor surface, where the discharge current is a direct current with a small superimposed pulsating current with a high repetition rate [1, 2].

Positive breakdown streamers are similar to onset streamers but extend further into the gap and lead to breakdown of the gap. The streamer current and repetition rate are higher than onset streamers [1,2].

3. MODELLING

The fluid model of a gas discharge is considered the most appropriate and successfully applied method to model the gas discharge.

Morrow et al proposed the use of the flux corrected transport algorithm (initially described by Boris and Book) as a numerical solution to the flow of charged particles in a gaseous system [15–19]. Morrow and Lowke applied the algorithm to the modelling of a streamer [15].

Shim et al further built on the FDM FCT methods for a two dimensional analysis of needle plane corona [20]. The finite difference schemes used in FCT however limit the shape of the grid, limit the type of complex geometries expected in discharges and can be computationally expensive. Georghiou et al proposed an improved finite element FCT method [21] and continued to implement it for various cases including the modelling of the gas discharge in two dimensions and investigating the role of photoionisation [22, 23]. Sattari et al have developed finite element methods to investigate Trichel pulses [24]. Deng et al have modelled the Trichel pulse under air flow conditions in two dimensions and successfully illustrated the influence the air flow on the space charge by showing that there was a decrease in repetition rate of Trichel pulses for 18 m.s^{-1} illustrate the effect of shifting the space charge [25]. The commercial package COMSOL Multiphysics® has become more popular in solving the drift diffusion equations and has been applied to gas discharges. Kim et al have investigated the breakdown voltage in air using COMSOL Multiphysics® [26]. Tran et al have investigated negative discharges in air with and without a dielectric barrier. The use of the fluid equations through COMSOL Multiphysics® in investigating surface charges on a dielectric barrier found good correlation with experiments [27]. Recently Zhuang and Zeng have developed a local discontinuous Galerkin method that combines the advantages of finite volume and finite element stating that it is a compact, local conservative and high order accurate method [28].

The FCT methods extend further into other research areas. Liu and Pasko, for example, have used similar algorithms to model positive and negative streamers that originate from quasi-static electric fields developed during lightning activity [29].

Whilst the authors have concentrated on negative corona and Trichel pulse, apart from the work done on positive glow by Morrow [15, 30], positive corona a modest presence in literature, possibly due to the unknown mechanisms that lead to initiation and possibly due to the space charge and electric field calculations for the discharge model.

The key to understanding the influence of singlet oxygen is to illustrate and understand the physical phenomena in positive corona using the information from the solution of the Boltzmann equation and as such the 1.5D FDM model is considered sufficient.

3.1 Drift-Diffusion Model

The gas discharge is modelled using the drift-diffusion equations, where there are four species electrons, positive ions, negative ions and singlet oxygen. It is possible to extend this to any of the excited species but not necessary for the work here. The continuity equations written for the species in one dimension are given by [15–17, 19]:

$$\frac{\partial N_e}{\partial t} = S + N_e\alpha|\vec{v}_e| - N_e\eta|\vec{v}_e| - N_eN_p\beta - \frac{\partial(N_e\vec{v}_e)}{\partial z} + \frac{\partial}{\partial z}\left(D_e\frac{\partial^2 N_e}{\partial z^2}\right) \tag{3}$$

$$\frac{\partial N_p}{\partial t} = S + N_e\alpha|\vec{v}_e| - N_eN_p\beta - N_nN_p\beta - \frac{\partial(N_p\vec{v}_p)}{\partial z} + \frac{\partial}{\partial z}\left(D_p\frac{\partial^2 N_p}{\partial z^2}\right) \tag{4}$$

$$\frac{\partial N_n}{\partial t} = N_e\eta|\vec{v}_e| - N_nN_p\beta - N_nN_ok_d - \frac{\partial(N_n\vec{v}_n)}{\partial z} + \frac{\partial}{\partial z}\left(D_n\frac{\partial^2 N_n}{\partial z^2}\right) \tag{5}$$

$$\frac{\partial N_o}{\partial t} = N_e\psi|\vec{v}_e| - N_nN_ok_d - N_oN_{O_2}k_q \tag{6}$$

Where:

- N_x = Number densities of electrons, positive ions, negative ions and singlet oxygen [cm^{-3}]
- N_{O_2} = Number density of oxygen [cm^{-3}]
- $\vec{v}_x$ = Velocities of electrons, negative ions and positive ions [cm.s^{-1}]
- α = Ionisation coefficient [cm^{-1}]
- η = Attachment coefficient [cm^{-1}]
- ψ = Singlet oxygen coefficient [cm^{-1}]
- S = Photoionisation term [cm^{-3}.s^{-1}]
- β = Recombination coefficient [cm^3.s^{-1}]
- D_x = Diffusion coefficient [cm^2.s^{-1}]
- k_d = Detachment rate coefficient [cm^3.s^{-1}]
- k_q = Quenching rate coefficient [cm^3.s^{-1}]

3.2 Photoionisation

A model of photoionisation was developed by Penny and Hummert, where they related the number of photo-electrons produced to the number of ionisation events [31]. They showed that the photoionisation events are dependent on the pressure and distance from the discharge with a function given by [31].

$$\phi = \frac{N_P}{N_D}\theta PD \tag{7}$$

Where:

N_D = Number of ion pairs produced per second
N_P = Number of photon pairs produced per second
PD = Pressure distance relationship [cm torr]
θ = Angle subtended by volume

The physical model for photoionisation was developed by Zheleznyak et al [32] partially based on the data, where the model was based on the assumption that excited nitrogen atoms will emit in the region of 98 - 102.5 nm which is absorbed by oxygen with an ionisation threshold of 102.4 nm and this leads to photoionisation. The rate of photoionisation is dependent on the absorption of the emission and as such the partial pressure of oxygen [23, 32, 33]. Kulikovsky implemented a photoionisation model based on the the Zheleznyak model, where the number of electron-ion pairs produced per second in incremental volume dV_1 due to ionisation events in volume dV_2 is given by [33]:

$$S(dV_1, dV_2) \simeq \frac{I(dV_2)f(r)}{4\pi r^2}dV_2 \tag{8}$$

$$I(dV_2) = \xi\frac{P_q}{P+P_q}\alpha N_e\frac{dx}{dt} \tag{9}$$

$$f(r) = \frac{\exp\left(-\chi_{min}P_{O_2}r\right) - \exp\left(-\chi_{max}P_{O_2}r\right)}{r\log(\chi_{max}/\chi_{min})} \tag{10}$$

Where:

r = Distance between volumes dV_1 and dV_2
P = Pressure [760 torr]
P_q = Quenching pressure [30 torr]
P_{O_2} = Partial pressure of oxygen [22%P]
$\chi_{max,min}$ = Absorption coefficients of O_2 [cm^{-1}.torr^{-1}]

Pancheshnyi et al investigated the role of background ionisation and indicated that this background ionisation can be neglected when the photoionisation is included [34].

3.3 Electric Field

The electric field is solved through Poisson's equation, which describes the potential at a point [35]:

$$\nabla^2\phi = -\frac{q_e}{\varepsilon_0}(N_p + N_n + N_e) \tag{11}$$

Poisson's equation is solved with number densities set to 0 to obtain the Laplacian electric field E_L.

Davies stated that the using a uniform or cylindrical form of Poisson's equation overestimates the influence of the space charge on the electric field, as the discharge is only limited to a channel. A solution using disc's of space charge is that takes account of the radius of the channel ,r, is proposed where the Poissonian axial field at point along the axis is given by [19, 36, 37]:

$$\begin{aligned} E(x) =& \frac{1}{2\varepsilon_0}\int_{-x}^{0}\rho(x+x')\left[-1-\frac{x'}{\sqrt{x'^2+r^2}}\right]dx' \\ &+\int_{0}^{d-x}\rho(x+x')\left[1-\frac{x'}{\sqrt{x'^2+r^2}}\right]dx' \end{aligned} \tag{12}$$

The total field is then the sum of the Laplacian and Poissonian electric fields:

$$E = E_L + E_P \tag{13}$$

3.4 Circuit Current

Sato applied this concept to the movement of space charge in gas discharges and Morrow subsequently completed it to the form given by [38, 39]:

$$\begin{aligned} I(t) =& \pi r^2\frac{q_e}{V_A}\int_0^d (N_p v_p - N_n v_n - N_e v_e \\ &+ \frac{\partial^2 DN_e}{\partial^2 x})E_L dx \end{aligned} \tag{14}$$

This form is however incomplete when relating it to the circuit as this current will affect the voltage applied to the test device [40]. The voltage applied to the test device is given by:

$$V_A = I(t)R - \frac{1}{C}\int I(t)dt \tag{15}$$

3.5 Results

The parameters used in the model are listed in Table 1.

An initial plasma number density is applied to the system, which gives a peak electron and positive ion density of 0.9995 cm^{-3} at 0.02 cm.

$$N_i = \exp(-(x+dx)^2) \tag{16}$$

The circuit current is illustrated in Figure 6 and it is followed by the pre-current pulse development of the electric field in Figure 7 and space charge in Figure 8 as well as the post current pulse development of the electric field in Figure 9 and space charge in Figure 10. The *Laplacian Field* refers to the electric field with no space charge and the *Space Charge Field* refers to the electric field determined only by the space charge. The *Total Field* is the sum of the two.

Table 1: Input parameters for positive corona model

Parameter/coefficient	Symbol	Value
Pressure	P	760 torr
Temperature	T	20 °C
Anode radius	r	0.02 cm
Electrode spacing	d	2.5 cm
Grid size	N_g	800
Grid spacing	dx	0.03 cm
Time step	dt	1×10^{-12}
Secondary ionisation	γ	0.01
Recombination	β	2×10^{-7}
Detachment	k_d	2×10^{-10}
Quenching	k_q	2×10^{-18}
Mobility of positive ion	μ_p	2.34 cm^2/V/s
Mobility of negative ion	μ_n	2.7 cm^2/V/s
Diffusion of positive ion	D_p	5×10^{-2} cm^2/s
Diffusion of negative ion	D_n	5×10^{-2} cm^2/s
Applied voltage	V_a	9 kV

It is clear that the in the process the role played by the positive ions far greater than the negative ions. The positive ions are generated rapidly at the electrode reaching a peak density of 2.4×10^{13} cm^{-3} after 30 ns, with the fast moving electrons at less than half this density after 50 ns. It is clear from Figure 7 that this distorts the field considerably causing a complete collapse near the electrode and a peak away from the electrode. This peak causes the streamer to propagate into the gap and the collapse prevents activity in the region close to the electrode. There will be no more ionisation activity until this space charge clears.

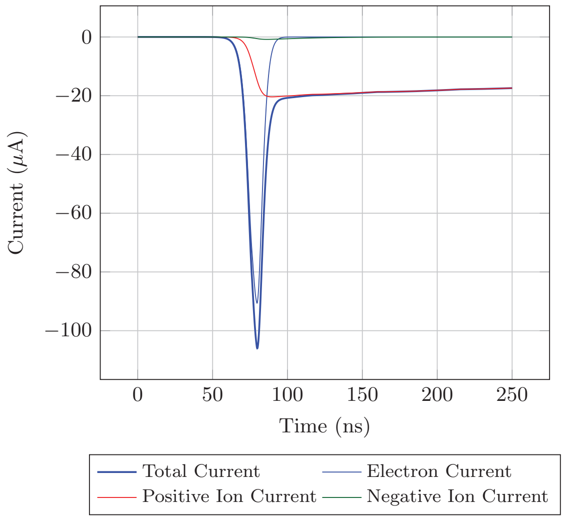

Figure 6: Circuit current for 250 μs

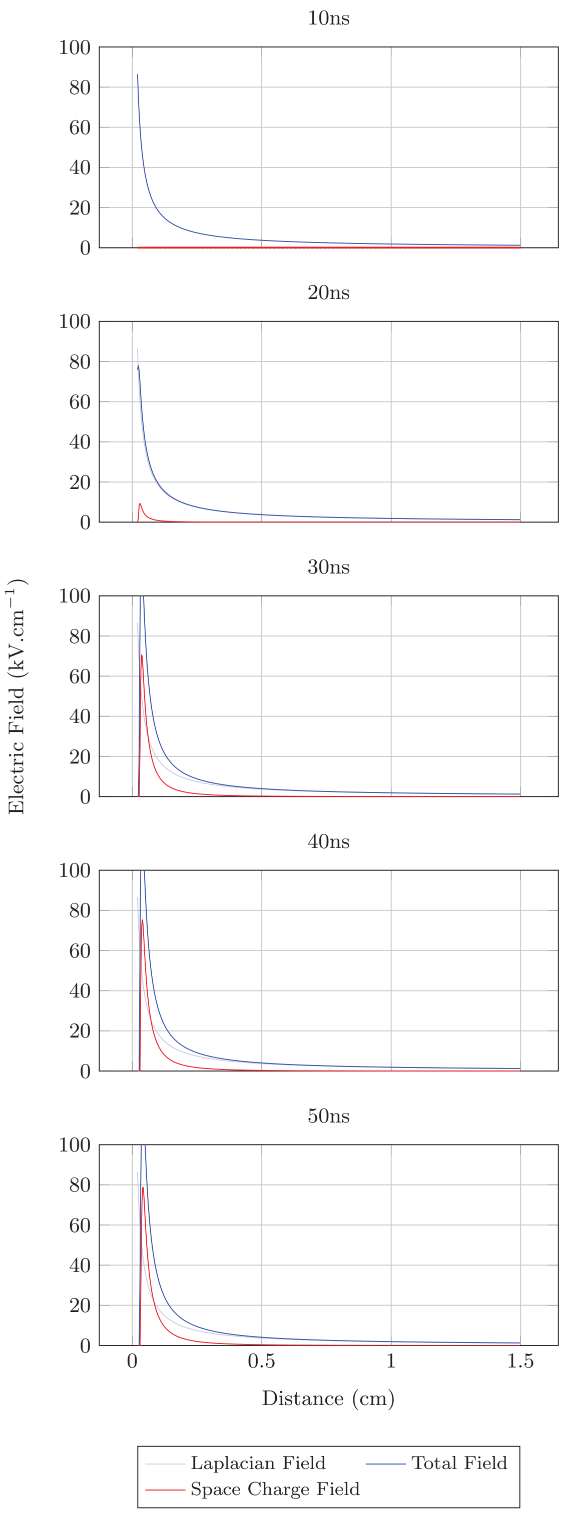

Figure 7: Electric field over 50 μs

Following the distortion of the field in the initial pulse, the field recovers slowly. The densities of the species decrease due to the activities that occur where the field has collapsed including recombination of positive ions and electrons, recombination of negative ions, and detachment of electrons from the reaction of negative ions and singlet oxygen. There is no drift velocity as there is no electric field and as such the normal Townsend generation of species due to electron collision does not exist. While there is some value in the process, it is thought that the 1.5D

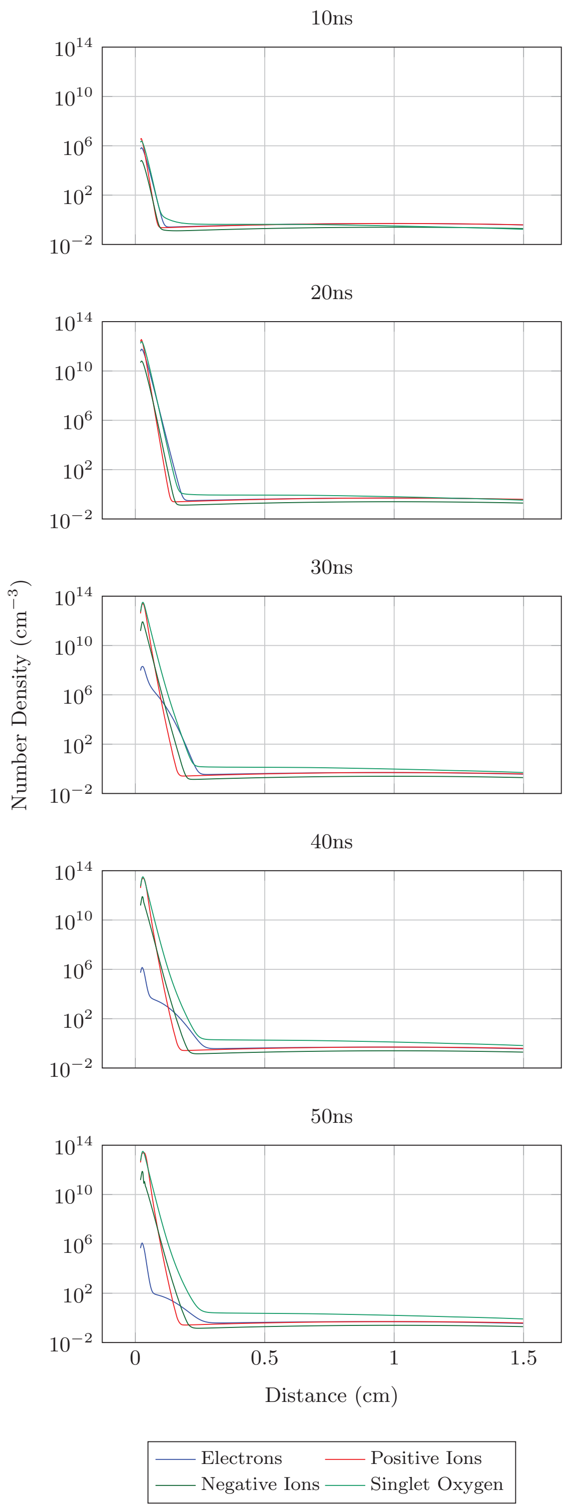

Figure 8: Number densities of species over 50 μs

model is limited in this respect.

The oscillations seen at B occur only for the negative ions for the positive corona. These are thought to be numerical errors due to the recombination of positive and negative ions and to the reaction of negative ions and singlet oxygen.

Singlet oxygen is generated within the region close to the cathode. After 4000 ns there is a peak singlet oxygen density of 8.5×10^{12} cm^{3}s^{-1} and a peak negative ion density of 3.92×10^{10} cm^{3}s^{-1}. With a neutral density of 2.5×10^{25} cm^{-3} and a quenching rate of 2×10^{-18} cm^3.s^{-1}, the expected emission is 4.25×10^{11} photons per cm^3 per nanosecond. The emission is slightly higher than that of negative corona it is however localised around the anode.

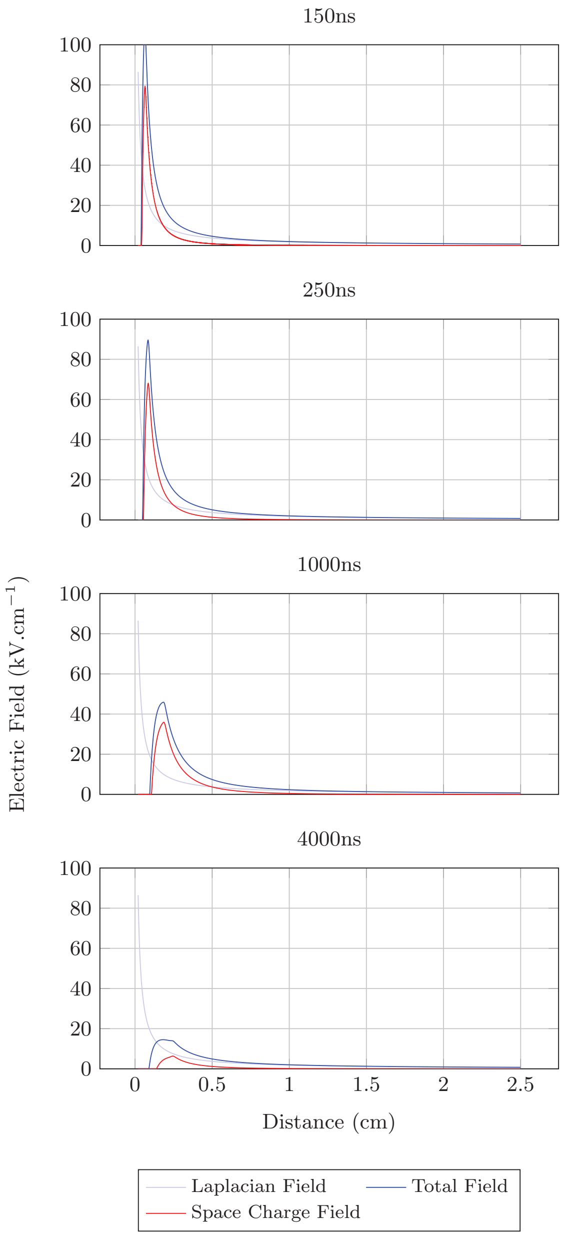

Figure 9: Electric field over the 4000 μs

To illustrate the argument Figure 11 overlays the negative ion and singlet oxygen densities at 4000 ns by the detached electrons considering a detachment rate of 2×10^{-7} cm^3.s^{-1} for the reaction between negative ions and

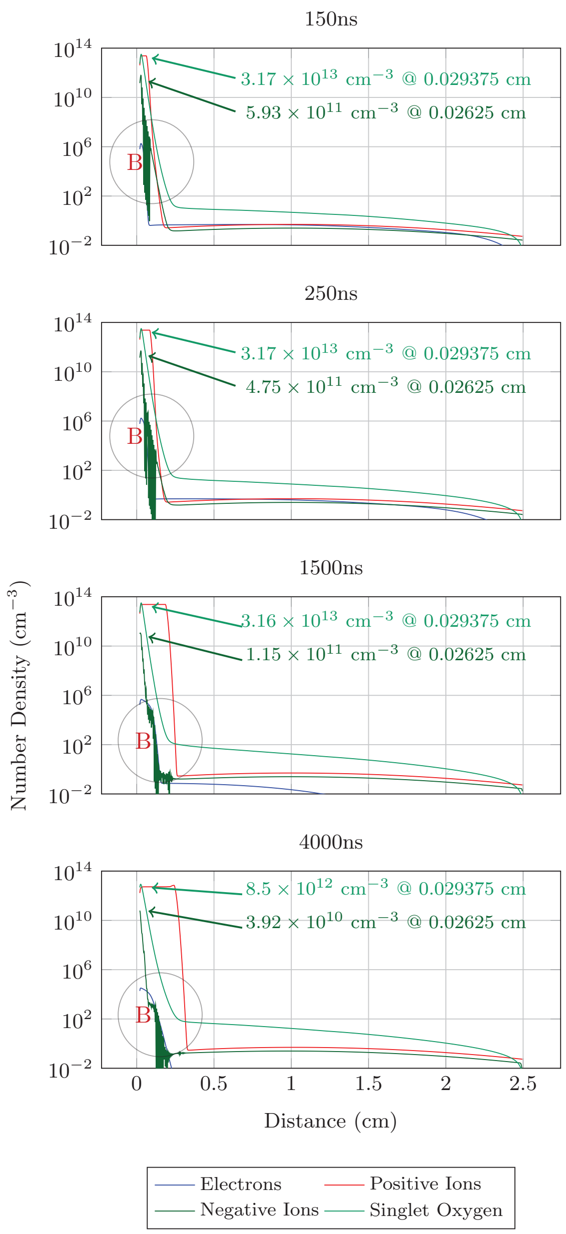

Figure 10: Number densities of species over 4000 μs

singlet oxygen. This is slightly misleading as the negative ion and singlet oxygen densities are not constant over time and still decreasing, however, there is value in identifying that electrons are released. There is a peak rate of 2.55×10^7 $cm^3.ns^{-1}$ at the anode and while this is a significant number, these electrons may be absorbed before impacting on the streamer. The rapid decline of detached electrons rate is clear in the plot and critical in extracting the influence of singlet oxygen. A higher density would be expected to initiate the streamer process, however the rate of 2.23 $cm^{-3}.ns^{-1}$ where $\alpha = \eta$ for the initial electric field illustrates that there may be a small correlation between the positive streamer and the singlet oxygen density should the field recover to its initial state. It is clear that the space charge is dominant and it takes a significant amount of time to recover, in that time electrons may be formed by other means leaving those generated by singlet oxygen relatively insignificant. A number of experiments are undertaken in the next section to understand the significance.

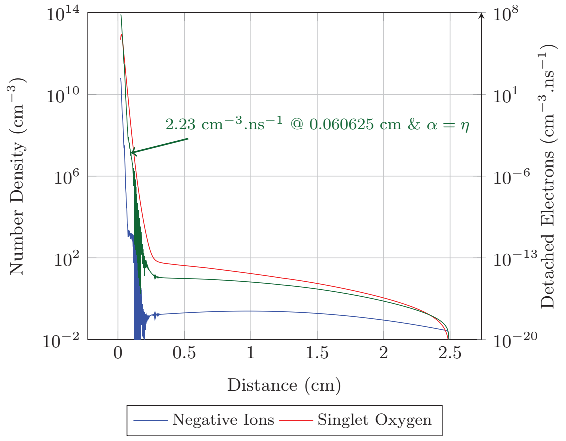

Figure 11: Negative ions and singlet oxygen densities overlaid by detached electrons

4. EXPERIMENTS

The experiment consisted of a point-plane configuration excited by a 50 kV DC source as shown in Figure 12. The point provided the necessary sharp electric field to produce positive onset streamers. The measurement system consisted of a voltage measured across a resistor below the second electrode. Gauss' law states that the measurement that the surface charge of the electrode will change according to the space charge inside of it [41].

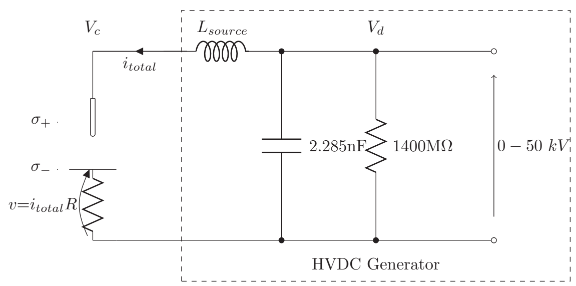

Figure 12: Experimental arrangement

4.1 Air Flow

The experiment was performed at the the high voltage laboratory at the University of the Witwatersrand which is located at an altitude of 1700 m. The experimental setup is illustrated in Figure 13 where a slow non-turbulent airflow of 5 $m.s^{-1}$ was applied to the configuration. This is a continuation of the initial work in reference [5], where the hypothesis was formed.

The results in Figure 14 illustrate the approximate regions of burst, onset streamer and glow corona for the point plane

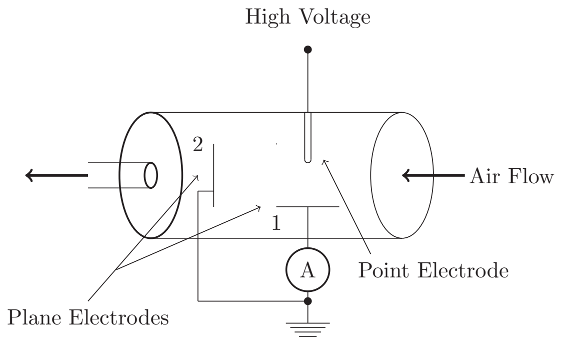

Figure 13: Experimental arrangement

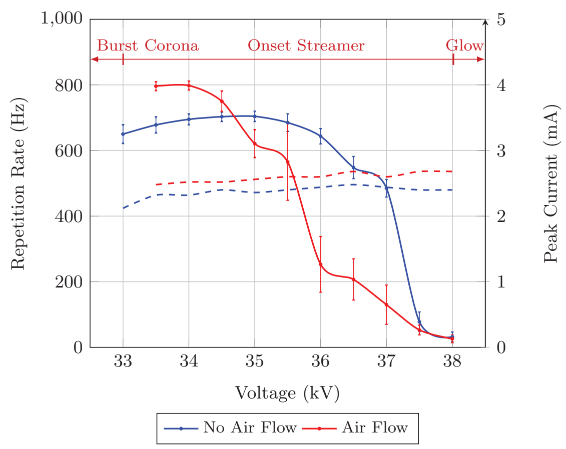

Figure 14: Measurement positive corona for airflow

experiment. It is evident that the air flow had an influence on the nature (and mode) of the corona, where initially the onset streamers increased in repetition rate and then sharply decreased in repetition rate. The average peak current was consistently higher for the air flow condition for all the applied voltages. The average peak current is dependent on the movement of the space charge and any small shift would cause the peak current to change slightly, which is evident in Figure 14.

The repetition rate of onset streamers are related to the collapse of the electric field at the conductor due to the positive space charge and the recovery due to the removal of the positive space charge [1], any influence on this space charge should theoretically result in an increase in the repetition rate as the field is restored faster. The results under air flow conditions were partially inconsistent with this theory.

The fact that the average peak current has a relatively small deviation and the repetition rate has a large deviation lends credibility to the hypothesis that singlet oxygen may be a source of seed electrons and be related to the repetition rate of the onset streamers. The detachment of electrons from negative ions would be dependent on both the density of negative ions and singlet oxygen and the slow moving air removes the singlet oxygen from the system and does not allow it to build up. Referring to the modelling of positive corona the densities of singlet oxygen and negative ions may not be large enough to react and produce sufficient seed electrons away from the anode to be the dominant process.

4.2 Infrared Detection

The purpose of the experiment was to measure a singlet oxygen emission and relate that to the repetition rate of positive onset streamers. Any relationship would indicate that it is a measurable and significant process.

The emissions of singlet oxygen due to the transition from singlet state to ground state or due to the dimol emission are given respectively by [42]:

$$O_2 + O_2(a^1\Delta_g) = 2O_2 + h\nu_{(1270nm)}$$

$$O_2(a^1\Delta_g) + O_2(a^1\Delta_g) = 2O_2 + h\nu_{(634nm)}$$

Considering the Grum and Costa investigation into the spectral emission of corona [43]:

- 200-500 nm is the dominant region of emission with peaks at 337 nm and 358 nm due to transitions of nitrogen. This region of emissions have since been used as a basis for investigating corona on high voltage equipment [44].
- 400-600 nm where the peaks in the region of 400 nm are around 12.5% of the peaks in the UV region.
- 600-900 nm where the emissions are the lowest. There is activity around the 630-650 nm region, however there is no distinct peak in the region.

This as well as being the only emission in the region informed the decision to measure 1270 nm. The 1270 nm emission was investigated with an InGaAs pin photodiode as a detector [45]. Importantly the photosensitivity of the photodiode lies in the range of 900 nm to 1700 nm making it the optimal diode to detect the photo luminescence of singlet oxygen. As the only expected emission from corona in this region is from singlet oxygen, the use of a filter is deemed unnecessary. The use of the photodiode over a photomultiplier tube was due to the saturation of the latter in the presence of an electric field.

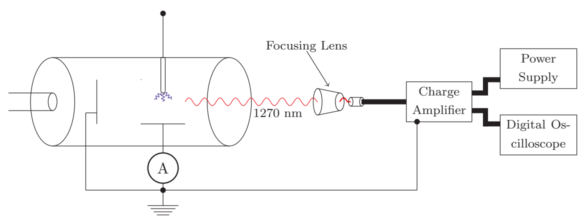

Figure 15: Experimental arrangement

The experiment was setup as illustrated in Figure 15 Figure 16 illustrates the optical emissions of the point plane gap in the visible region, where the extension of the onset streamers was approximately 1 cm from the anode surface. The infrared measurement system produced no detectable emissions from singlet oxygen, which could have been due to the weak emissions or due to detector sensitivity. The long lifetime of singlet oxygen does not assist with detection even if the densities are high. It has been noted that detection of singlet oxygen has been a difficult measurement to make in numerous fields including chemical and medical fields where more sensitive photomultiplier tubes have been used to detect it [46,47].

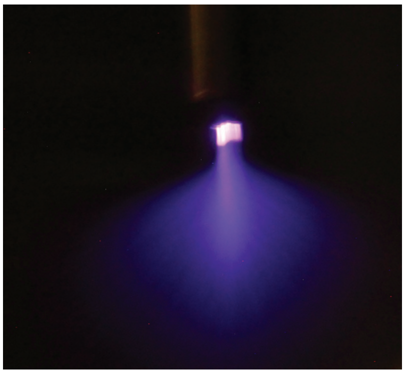

Figure 16: Onset streamer

4.3 *Laser Excitation*

The aim of the experiment was to determine the contribution of the singlet oxygen in the positive onset streamer by using a laser to excite the oxygen and observing the changes in waveform and repetition rate of the positive onset streamers. The advantage of this excitation due to the laser is that it isolates singlet oxygen and should have no effect on the space charge.

The Beer Lambert law relates the absorption capabilities of the material to the light and is given by [48]:

$$I = I_0 \exp(-\sigma N x) \tag{17}$$

Where:

I = Intensity
I_0 = Initial intensity
σ = Absorption cross-section
N = Number density of the neutral
x = Thickness of material

At 1.27 μm and 1.06 μm with peak cross sections of 2.52 $\times 10^{-26}$ and 0.717 $\times 10^{-26}$ cm^2.molecule^{-1} for a mixture of 21% O_2 and 79% N_2 at 20 °C and at an altitude of 1400 m; the intensity after 1 cm is $0.59 I_0$ and $0.86 I_0$ for 1.27 μm and 1.06 μm respectively [49].

Jockusch et al have shown that oxygen is directly excitable through the use of an Nd:YAG laser with a wavelength of 1064 nm where the expected processes related to singlet oxygen include [46]:

The excitation process is [46]:

$$\left[{}^3\Sigma_g^-(\nu=0)\right] + h\nu_{1064nm} \quad \rightarrow \quad \left[{}^1\Delta_g(\nu=1)\right]$$

The emission processes are [46]:

$$\begin{aligned} \left[{}^1\Delta_g(\nu=1)\right] &\rightarrow \left[{}^1\Delta_g(\nu=0)\right] + \text{heat} \\ \left[{}^1\Delta_g(\nu=0)\right] &\rightarrow \left[{}^3\Sigma_g^-(\nu=0)\right] + h\nu_{1270nm} \end{aligned}$$

The experiments were performed at the National Laser Centre at the CSIR at an altitude of 1400 m with a setup as illustrated in Figure 17. The laser was aimed approximately 1 cm below the electrode and each laser pulse had a 10 Hz frequency, a width of 10-20 ns, a beam diameter of 1cm (unfocused) and an energy of 118 mJ or 800 mJ.

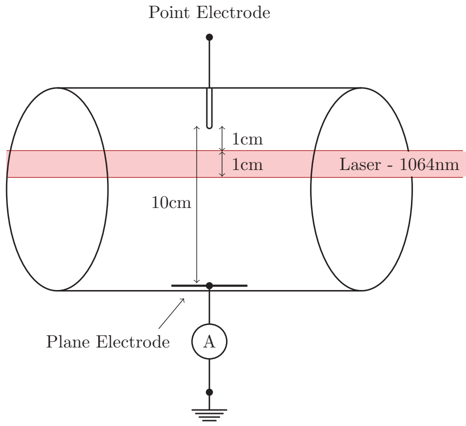

Figure 17: Experimental arrangement

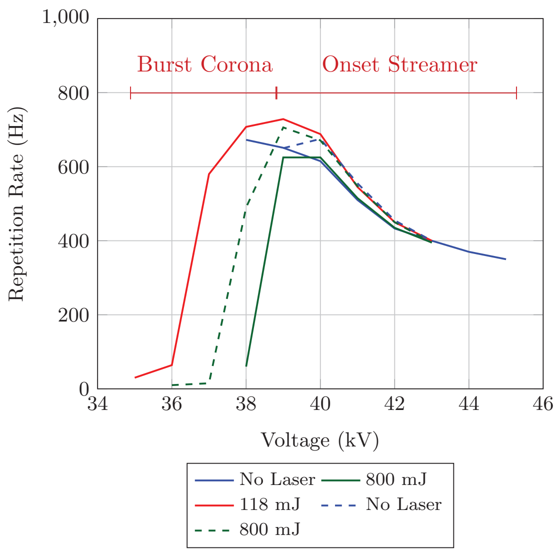

Figure 18: Measurement of positive corona for laser excitation

The repetition rate for positive onset streamers under normal conditions and for when the laser was fired in at

118 mJ and 800 mJ are illustrated in Figure **??**. There are some differences at lower applied voltages, but tend to converge from 40 kV. Below 40 kV it was difficult to define the corona as onset streamers as it was inconsistent and it has been defined as burst corona. It is not evident that any singlet oxygen produced had an influence on the repetition rate of corona. The modelling illustrated that the singlet oxygen and negative ions produce high densities close to the anode, but are not produced further away where the reaction between negative ions and singlet oxygen does occur but is significantly less (Figure 11). It is felt by the author that the lack of negative ions in the region as shown by the modelling is critical, it is also evident that in the region where there are high densities of both negative ions and singlet oxygen, the ionisation, attachment and photoionisation mechanisms would be dominant.

5. CONCLUSION

The theory behind corona in air indicates that there are multiple excited states of its constituents. These excited states do play a role in the process, particularly where the energy of photons emitted from the excited molecules is high. The role of singlet oxygen was less well understood due to its low energy level and its secondary role of contributing to the production of seed electrons.

The modelling indicated that the influence of space charge on the collapse of the field for positive corona is the critical component of the pulse formation and duration. The model indicated that there is a presence of singlet oxygen, however the role it plays may be insignificant to that of the space charge.

The experiments investigated the role of singlet oxygen and illustrated that it is not a contributing factor to the positive onset streamers. This is inferred from the fact that

- The airflow influenced the removal of space charge and altered the repetition rate of positive onset streamers. The mode is pushed towards that of positive glow.
- The emission from singlet oxygen at 1270 nm was not detectable, both due to the low emission from singlet oxygen and sensitivity of the photodiode.
- The repetition rate does not change when oxygen is directly excited in the system through the use of a laser.

It is concluded that singlet oxygen plays no distinguishable role in the repetition rate of positive onset streamers as the production of seed electrons is minimal.

6. ACKNOWLEDGEMENTS

The authors would like to thank Eskom for the support of the High Voltage Engineering Research Group through the TESP programme. They would also like to thank CBI-electric for support, the department of Trade and Industry (DTI) for THRIP funding as well as to the National Research Foundation (NRF) for direct funding.

The authors would like to thank Roel Stolper from the CSIR for the loan of lenses to aid in the detection experiments and Bathusile Masina and Thomas du Plooy from the CSIR National Laser Centre for allowing the use of the Nd:YAG laser for the experiments.

REFERENCES

[1] P. Sarma Maruvada, *Corona Performance of High Voltage Transmission Lines*. Taylor and Francis Group, 2000.

[2] T. Giao and J. Jordan, "Modes of corona discharges in air," *IEEE Transactions on Power Apparatus and Systems*, vol. 87, no. 5, 1968.

[3] J. Lowke, "Theory of electrical breakdown in air - the role of metastable oxygen molecules," *Journal of Physics D: Applied Physics*, vol. 25, 1992.

[4] J. Lowke and R. Morrow, "Theory of electric corona including the role of plasma chemistry," *Pure and Applied Chemistry*, vol. 66, no. 6, 1994.

[5] A. Swanson, M. Grant, I. Hofsajer, and I. Jandrell, "HVDC corona - experimental setup and measurements," *International Symposium on High Voltage Engineering, Seoul, South Korea*, 2013.

[6] E. Kuffel, W. Zaengl, and J. Kuffel, *High Voltage Engineering: Fundamentals*, 2nd ed. Newnes, 2000.

[7] Y. Itikawa, M. Hayashi, A. Ichimura, K. Onda, K. Sakimoto, and K. Takayanagi, "Cross sections for collisions of electrons and photons with nitrogen molecules," *Journal of Physical Chemistry*, vol. 15, no. 3, 1986.

[8] Y. Itikawa, "Cross sections for electron collisions with nitrogen molecules," *Journal of Physical Chemistry*, vol. 35, no. 1, 2006.

[9] Y. Itikawa, A. Ichimura, K. Onda, K. Sakimoto, and K. Takayanagi, "Cross sections for collisions of electrons and photons with oxygen molecules," *Journal of Physical Chemistry*, vol. 18, no. 1, 1989.

[10] Y. Itikawa, "Cross sections for electron collisions with oxygen molecules," *Journal of Physical Chemistry*, vol. 38, no. 1, 2009.

[11] A. Phelps and L. Pitchford, "Anisotropic scattering of electrons by N_2 and its effect on electron transport," *Phys. Rev. A*, vol. 31, no. 5, 1985.

[12] Plasma Data Exchange Project, "Lxcat," *http://fr.lxcat.net/home/, last accessed March 12, 2015*.

[13] G. Hagelaar and L. Pitchford, "Solving the boltzmann equation to obtain electron transport coefficients and rate coefficients for fluid models," *Plasma Sources Science and Technology*, vol. 14, 2005.

[14] A. Swanson, M. Grant, and I. Jandrell, "HVDC corona - analysis of corona through modelling techniques," *International Symposium on High Voltage Engineering, Seoul, South Korea*, 2013.

[15] R. Morrow and J. Lowke, "Streamer propagation in air," *Journal of Physics D: Applied Physics*, vol. 30, 1997.

[16] R. Morrow, "Numerical solution of hyperbolic equations for electron drift in strongly non-uniform electric fields," *Journal of Computational Physics*, 1981.

[17] R. Morrow and L. Crem, "Flux-corrected transport and diffusion on a non-uniform mesh," *Journal of Computational Physics*, 1985.

[18] J. Boris and D. Book, "Flux-corrected transport. I. SHASTA, a fluid transport algorithm that works," *Journal of Computational Physics*, 1973.

[19] R. Morrow, "Theory of negative corona in oxygen," *Phys. Rev. A*, 1985.

[20] J. Shim, S. Choi, H. Hwang, H. Ha, K. Ko, and H. Kang, "2-d simulation on the corona discharge of negative needle-to-plane electrodes," *IEEE Transactions on Magnetics*, vol. 38, no. 2, 2002.

[21] G. Georghiou, R. Morrow, and A. Metaxas, "An improved finite-element flux-corrected transport algorithm," *Journal of Computational Physics*, vol. 148, 1999.

[22] ——, "A two-dimensional, finite-element, flux-corrected transport algorithm for the solution of gas discharge problems," *Journal of Physics D: Applied Physics*, vol. 33, 2000.

[23] A. Hallac, G. Georghiou, and A. Metaxas, "Secondary emission effects on streamer branching in transient non-uniform short-gap discharges," *Journal of Physics D: Applied Physics*, vol. 36, 2003.

[24] P. Sattari, C. Gallo, S. Castle, and K. Adamaniak, "Trichel pulse characteristics—negative corona discharge in air," *Journal of Physics D: Applied Physics*, vol. 44, 2011.

[25] F. Deng, L. Ye, and K. Song, "Numerical studies of trichel pulses in airflows," *Journal of Physics D: Applied Physics*, 2013.

[26] N. Kim, S. Lee, G. Georghiou, D. Kim, and D. Kim, "Accurate prediction method of breakdown voltage in air at atmospheric pressure," *Journal of Electrical Engineering and Technology*, vol. 7, 2012.

[27] T. Tran, I. Golosnoy, P. Lewin, and G. Georghiou, "Numerical modelling of negative discharges in air with experimental validation," *Journal of Physics D: Applied Physics*, vol. 44, 2011.

[28] Zhuang and Zeng, "A local discontinuous galerkin method for 1.5-dimensional streamer discharge simulations," *Applied Mathematics and Computation*, vol. 219, 2013.

[29] N. Liu and V. Pasko, "Effects of photoionization on propagation and branching of positive and negative streamers in sprites," *Journal of Geophysical Research*, vol. 109, 2004.

[30] R. Morrow, "The theory of positive glow corona," *Journal of Physics D: Applied Physics*, vol. 30, 1997.

[31] G. Penney and G. Hummert, "Photoionization measurements in air, oxygen and nitrogen," *Journal of Applied Physics*, vol. 41, no. 2, 1970.

[32] M. Zheleznyak, B. Mnatskanian, and S. Sizykh, "Photoionization of nitrogen and oxygen mixtures by radiation from gas discharge," *High Temperature*, 1982.

[33] A. Kulikovsky, "The role of photoionization in positive streamer dynamics," *Journal of Physics D: Applied Physics*, vol. 33, 2000.

[34] S. Pancheshnyi, S. Starikovskaia, and A. Y. Starikovskii", "Role of photoionization process in propagation of cathode-directed streamer," *Journal of Physics D: Applied Physics*, vol. 34s, 2001.

[35] J. Kraus, *Electromagnetics*, 4th ed. McGraw-Hill, Inc, 1991.

[36] A. Davies, C. Evans, and F Llewellyn Jones, "Electrical breakdown of gases: The spatio-temporal growth of ionization in fields distorted by space charge," *Proceedings of the Royal Society of London - Series A: Mathematical and Physical Sciences*, vol. 281, no. 1385, 1964.

[37] A. Davies, "Discharge simulation," *IEE Proceedings A*, vol. 133, no. 4, 1986.

[38] N. Sato, "Discharge current induced by the motion of charged particles," *Journal of Physics D: Applied Physics*, vol. 13, 1980.

[39] R. Morrow and N. Sato, "The discharge current induced by the motion of charged particles in time-dependent electric fields; Sato's equation extended," *Journal of Physics D: Applied Physics*, vol. 32, 1999.

[40] J. Verboncoeur, M. Alves, V. Vahedi, and C. Birdsall, "Simultaneous potential and circuit solution for 1d bounded plasma particle simulation codes," *Journal of Computational Physics*, vol. 104, 1993.

[41] C. Birdsall, “Particle-in-cell charged particle simulations, plus Monte Carlo collisions with neutral atoms, pic-mcc,” *IEEE Transactions on Plasma Science*, vol. 19, no. 2, 1991.

[42] D. Kearns, “Physical and chemical properties of singlet oxygen,” *Chemical Reviews*, vol. 71, no. 4, 1971.

[43] F. Grum and L. F. Costa, “Spectral emission of corona discharges,” *Appl. Opt.*, vol. 15, no. 1, pp. 76–79, Jan 1976. [Online]. Available: http://ao.osa.org/abstract.cfm?URI=ao-15-1-76

[44] W. Vosloo, R. Stolper, and P. Baker, “Daylight corona discharge observation and recording system,” *International Symposium on High Voltage Engineering, Quebec, Canada*, 1997.

[45] Hamamatsu, “InGaAs PIN Photodiodes - G8376 Series,” *http://www.hamamatsu.com*, last accessed 2013.

[46] S. Jockusch, N. Turro, E. Thompson, M. Gouterman, J. Callis, and G. Khalil, “Singlet molecular oxygen by direct excitation,” *The Royal Society of Chemistry: Photochemical and Photobiological Sciences*, 2008.

[47] M. Niedre, M. Patterson, and B. Wilson, “Direct near-infrared luminescence detection of singlet oxygen generated by photodynamic therapy in cells in vitro and tissue in vitro,” *Photochemistry and Photobiology*, vol. 75, 2002.

[48] R. Serway and R. Beichner, *Physics for Scientists and Engineers with Modern Physics*, 5th ed. Saunders College Publishing, 2000.

[49] K. Smith and D. Newham, “Near-infrared absorption cross-sections and integrated absorption intensities of molecular oxygen (O_2, $O_2 - O_2$ and $O_2 - N_2$),” *Journal of Geophysical Research*, vol. 105, no. D6, 2000.

SPACE-TIME PRECODED CDMA-OFDMA EMPLOYING SUPER-ORTHOGONAL COMPLETE COMPLEMENTARY CODES

N. de Figueiredo[†] **and L.P. Linde**[‡] **and J.H. van Wyk**[*]

[*] *Department of Electrical, Electronic & Computer Engineering, University of Pretoria, Lynnwood Road, Pretoria, South Africa E-mail:* { [†]*NikolaideFigueiredo@gmail.com*, [‡]*louis.linde@up.ac.za, jhvanwyk@up.ac.za*}

Abstract: This paper addresses and illustrates, both analytically as well as by means of simulation, the equivalence of a cyclically rotated complete complementary coded (CRCCC) code division multiple access orthogonal frequency division multiplexed (CDMA-OFDM) BPSK/QPSK system and a narrowband uncoded BPSK/QPSK reference system. The equivalence can be attributed to the MUI-free characteristic performance of CRCCCs. It is demonstrated that when employed in a multiple-input multiple-output (MIMO) antenna configuration along with orthogonal space-time block codes (OSTBCs), the maximum theoretical diversity order of $N_{Tx}N_{Rx}$ is achieved. Most significantly, simulations show that CDMA-OFDM using CRCCCs is capable of rendering additional multipath diversity gain at no additional processing cost. This signifies improved performance when compared with conventional ST-OFDM systems.

Key words: CRCCC, OSTFBC, STF-CDMA-OFDM, diversity, multi-user-interference (MUI) free, multiple-access (MA)

1. INTRODUCTION

In the process of striving to achieve higher data rates and improved performance within limited bandwidth, engineers are often forced to employ new combinations of well established techniques to meet the said objectives. One example of the latter is the use of multiple-input multiple-output (MIMO) techniques that have emerged to become pivotal in meeting the capacity demands of modern wireless cellular networks. By employing multiple antennas using MIMO principles, additional spatial degrees of freedom have been added to existing already saturated temporal, frequency and coded (spread) diversity domains. Although this may seem to have provided much needed relief to the improved capacity demand, it introduced a number of new challenges. In its infancy MIMO promised remarkable increases in capacity [1]. Unfortunately this was obtained at the cost of exceedingly complex detection algorithms under idealistic operating conditions. However, the Bell Labs layered space-time (BLAST) architecture did indeed demonstrate that it was possible to achieve the predicted capacity [2]. On the other hand, it was shown that it is possible to achieve transmit diversity while maintaining a remarkably simple linear receiver structure [3]. Further investigation into this field spawned the use of space-time coding, and more specifically, orthogonal space-time block codes (OSTBC) [4]. One major conclusion from these studies is that capacity and diversity are irreconcilable gains offered by MIMO.

The introduction of multiple antennas has done nothing to address the pressing concerns of multiple users in modern wireless cellular networks. With the roll-out of fourth generation (4G) networks, orthogonal frequency division multiple access (OFDMA) emerged as a technology of the future. OFDM is primarily favoured as the preferred modulation scheme, because of the reduced complexity offered by the use of the Fast Fourier Transform (FFT) algorithm. The FFT has been combined with space-time block codes (STBC) resulting in ST-OFDM [4], and application of OFDMA to this scenario is one solution.

Another approach is to use code division multiple access (CDMA) along with OFDM [5]. This combination will henceforth be referred to as space-time-frequency-(spread) CDMA-OFDM (STF-CDMA-OFDM). Historically CDMA alone is not favoured due to its inability to scale and its suboptimal performance in third generation networks. The latter can be primarily attributed to oversimplified choices of non-perfect suboptimal (Gold and Walsh-Hadamard) spreading (channelisation) sequences in present CDMA systems. The latter set of sequences hardly possess acceptable autocorrelation (AC) properties, while their cross-correlation (CC) only produce zero values at zero relative time shifts, with large sub-peaks at a distance of as little as $\pm$ one sampling interval from the origin. This narrow zero cross-correlation margin calls for extremely accurate and stable clock recovery in order to prevent excessive inter-code and/or multi-user interference (MUI). This form of distortion is the primary cause of CDMA performance loss and diminishing processing gain as a result of non-perfect spreading sequence design. The maturing of the field led to the reviving of families of spreading sequences with perfect priodic and aperiodic cross-correlation and auto-correlation properties (requirements of super-orthogonality), originally proposed by Golay [6].

The best results are attained when new innovation is applied to render remarkable improvements compared to previous results. A further refinement of the orthogonal complete complementary (OCC) codes proposed in [7] provided a solution to the rate loss and scaling issue of CDMA orthogonal variable spreading factor (OVSF) codes. The modified OCC codes are termed super-orthogonal cyclically rotated complete complementary codes (CRCCC) [8]. CCC is regarded as ideal orthogonal codes, in contrast to Walsh-Hadamard or OVSF codes, whose orthogonality is lost if used in asynchronous transmission systems, such as uplink channels in a mobile cellular scenario [8, p236].

This work presents a novel layered [9] modulation scheme that combines ST-OFDM and super-orthogonal CRCCCs to achieve transmit diversity. The elegant combination of these techniques leads to another interesting outcome: while providing multiple access (MA), the spreading codes also distribute energy from all symbols over all OFDM sub-carriers without destroying sub-carrier orthogonality. The result of this is a triply orthogonal modulator that achieves transmit diversity, extracts additional multipath (frequency) diversity and requires only a linear receiver to achieve maximum likelihood (ML) detection performance in the presence of fading. It should be emphasized that the choice of a combination of CDMA and OFDM was made to yield a multi-layered multi-user interference (MUI) free multiple-access modulation scheme that would be particularly robust under fading multipath channel conditions, as apposed to conventional OFDMA approaches primarily aimed at achieving maximum capacity. One typical application of the said modulation method is the primary control channel of a long distance surveillance remote piloted vehicle (RPV).

2. SYSTEM MODEL

The proposed system operates by mapping several independent multi-carrier (MC) CDMA sequences to an array of antennas according to an OSTBC with maximal rate. The MC-CDMA sequences are generated by spreading independent symbol blocks with the same family of CRCCCs and then multiplexing the resulting sequence onto orthogonal sub-carriers via the IFFT. Each of these modulation operations serves a particular purpose in a wireless communication system. The OFDM allows the multipath channel to be affectively divided into many flat faded channels with a significantly reduced complexity. OSTBCs add a transmit diversity advantage with multiple antennas with linear detectability. Furthermore, the CRCCCs provide a means for multiple users to share the same physical propagation medium without excessive MA interference (MAI).

2.1 Cyclically rotated complete complementary codes

In order to illustrate the potential of CRCCCs, certain assumptions must be made. Firstly, the code sequences must be synchronised in much the same way as the downlink of a cellular network. Secondly, it was assumed that the system has perfect timing and frequency synchronisation, and thirdly, perfect channel state information (CSI) is available. With this in mind, consider an OCC code family composed of K flocks (groups) of sequences, each made of M length N sequences. Thus, each flock is of length MN. OCC code families exhibit ideal correlation properties, i.e., the CC between two flocks for any cyclic chip shift is given by:

$$R_{c_a,c_b}[n] = \sum_{i=1}^{N-n}\sum_{j=1}^{M} c_{i,j,a}c_{j,j+n,b} = 0 \quad \forall\, n, \tag{1}$$

and the AC of each flock is given by:

$$R_{c_a,c_a}[n] = \sum_{i=1}^{N-n}\sum_{j=1}^{M} c_{i,j,a}c_{j,j+n,b} = \begin{cases} MN & n=0 \\ 0 & \text{otherwise} \end{cases}. \tag{2}$$

$R_{c_a,c_b}[n]$ represents the aperiodic CC between two complementary sequences, c_a and c_b. Interestingly, it has been shown that if a family of complementary sequences exhibits these ideal properties for aperiodic correlation, they also exhibit these properties for periodic correlation [7]. With a classical OCC code family a maximum of K symbols may be transmitted simultaneously. By imposing the synchronised code constraint, the symbol rate may be increased to NK. This is achieved by extending the OCC code family as follows - Taking the first of K flocks and cyclically rotating each of the element codes by one chip period, a new flock is created that maintains orthogonality with the original parent flock. Repeating the procedure for each of $N-1$ remaining chips, a total of N OCC flocks can be generated from flock one. Extending the procedure to each of the remaining $K-1$ flocks, an OCC family may be extended to a total of KN flocks of CRCCCs. Finally, if a super orthogonal complementary code (SOCC) family is used (i.e., an OCC code family with K=M), the CRCCC family size equals MN. This implies that MN symbols may be transmitted simultaneously, i.e., a rate of

$$\begin{aligned} R &= \tfrac{KN}{MN} \\ &= 1 \quad symbol/chip \end{aligned} \tag{3}$$

may be achieved, when compared with conventional MC-CDMA systems, which only provides $1/N$ symbols/chip. It should be noted that the summation of CRCCC codes leads to a multilevel signal that affects the Peak-to-Average Power Ratio (PAPR) of the system. However, by applying a Generalized Boolean Function (GBF) approach as described in [10], a considerable improvement in PAPR can be obtained for our system, when compared to traditional OFDM systems. When quadrature phase shift keying (QPSK) is employed as the underlying digital modulation scheme, a spectral efficiency of 2 bits/s/Hz may be attained, while maintaining the bit error probability (BEP) performance of binary phase shift keying (BPSK) in AWGN [8]. Although the need for synchronisation of the codes may be a disadvantage, only the code sequences generated by cyclically rotating a single flock need to maintain relative synchronism. This is because the correlation properties of the OCC code sequences hold for both the periodic and non-periodic (aperiodic) correlation functions ensuring that the perfect complete complementary properties of the new family of CRCCC sequences are maintained. Therefore, by assigning an extended flock of CRCCCs to a single user, it is possible to provide significant increase in rate and spectral efficiency. The grouping of sequences belonging to an extended flock is further motivated by the ability to decode groups of sequences in a single FFT operation. This is achieved by performing fast correlation according to:

$$R_{\mathbf{r},\mathbf{c}_k^0} = \sum_{m=1}^{M} \mathcal{F}^{-1}\left\{\mathcal{F}\{\mathbf{r}^{(m)}\}\cdot\left[\mathcal{F}\left\{\mathbf{c}_{m,k}^0\right\}\right]^*\right\}, \qquad (4)$$

where $\mathcal{F}[.]$ and $\mathcal{F}^{-1}[.]$ represents the FFT and IFFT operations, respectively, $(.)^*$ denotes the complex conjugate and $\mathbf{r}^{(m)}$ is the mth sequence of received symbols corresponding to the mth element code. Each symbol in the resulting sequence is a sufficient statistic for the detection of the data transmitted using one of the cyclically rotated extension sequences corresponding to the decoding sequence $c_k^0 = [c_{1,k}^0\ c_{2,k}^0\ \ldots\ c_{M,k}^0]$ (i.e., the original parent code of the CRCCC extended flock). The index of the decision variable corresponds to the number of cyclic chip rotations that was performed on the parent flock.

2.2 *Space-time orthogonal frequency division multiplexing*

The CRCCCs have been shown to perform identical to BPSK in a single antenna environment [8]. This is extended to the multi-antenna environment in this paper, by employing the combination of OSTB and space-time-frequency OFDM (STF-OFDM). This approach achieves a diversity order of $N_{Tx}N_{Rx}$, i.e., the product of the number of transmit and receive antennas, as opposed to a diversity order of N_{Rx} in the case of spatial multiplexing. However, there is a compromise to be made: spatial multiplexing yields large capacity gains predicted for multiple antennas when $N_{Rx} \geq N_{Tx}$, but at the cost of an increase in non-linear detection complexity. This is normally not applicable to the forward channel where the mobile mostly uses a single antenna and also has limited computational resources. OSTBs may have reduced capacity, but it is due to this reduction that improved performance is achievable with a single receive antenna. The maximum rate achievable with OSTBCs is [9]:

$$R_{max} = \frac{m+1}{2m}, \qquad (5)$$

where $N_{Tx} = 2m-1$ or $N_{Tx} = 2m$. Let $\mathbb{N}$ denote the set of all natural numbers, so that $\{m \in \mathbb{N} | m \leq 8\}$. Taking n_s blocks of data symbols and performing the modulation operations common to single antenna systems, produces a set of vectors

$$\mathbf{s}_i = \Phi\mathbf{W}^H\mathbf{C}\mathbf{d}_i \quad i = 1,2,\ \ldots\ n_s, \qquad (6)$$

where $\mathbf{d}_i$ is the ith vector of digitally modulated symbols, $\mathbf{C}$ is a matrix with columns formed by the flocks of the extended CRCCC, $\mathbf{W}$ is the discrete Fourier transform matrix and Φ is a cyclic extension matrix. Taking the rows of the resulting matrix in (6) and mapping them to a sequence of matrices,

$$\{\mathbf{s}_1[n]\ \mathbf{s}_2[n]\ \ldots\mathbf{s}_{n_s}[n]\} \rightarrow \{\Phi[n]\}n = -CP, -CP+1,\ \ldots,\ N_{FFT}-1, \qquad (7)$$

according to an OSTBC, the triply orthogonal modulation is completed. This mapping is mathematically equivalent to mapping the entire OFDM symbols according to the OSTBC before transmission. The index n represents the discrete time index of the MC-CDMA sequences, N_{FFT} is the FFT length (also equal to MN for the system concerned) and CP is the cyclic prefix length. The transmitter is depicted in Figure 1 and the receiver in Figure 2.

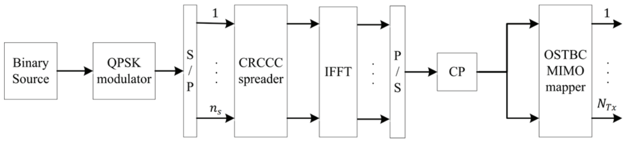

Figure 1: The modulation process performed at the transmitter

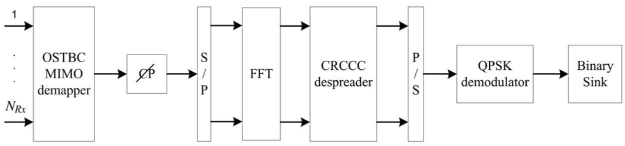

Figure 2: The demodulation process performed at the receiver

The received symbols are described by

$$\mathbf{Y}[n] = \sum_{l=0}^{L} \mathbf{H}_l\Phi[n-l] + \mathbf{N}_\sigma[n] \quad n = 0,1,\ \ldots,\ N_{FFT}-1. \qquad (8)$$

The ith column of $\mathbf{Y}[n]$ corresponds to the samples received at time n during the ith OFDM symbol period (n is relative to the beginning of the symbol period), $\mathbf{H}_l$ is the lth matrix channel tap value of a length $L+1$ channel impulse response, and $\mathbf{N}_\sigma[n]$ is a matrix containing *i.i.d.* AWGN samples with zero mean and standard deviation σ_n. With this formulation of the received symbols the detection criterion for the MIMO demapping stage of the receiver is expressed as:

$$\sum_{n=0}^{N_{FFT}-1} ||\mathbf{z}[n] - \mathbf{F}[n]\hat{\mathbf{s}}[n]||^2, \qquad (9)$$

where,

$$\hat{\mathbf{s}}[n] \quad = \left[\Re\left[\hat{\mathbf{s}}^T[n]\right]\ \Im\left[\hat{\mathbf{s}}^T[n]\right]\right]^T, \qquad (10)$$

$$\mathbf{z}[n] = vec\left(\mathbf{Z}[n]\right), \qquad (11)$$

$$\mathbf{Z}[n] = \frac{1}{\sqrt{N_{FFT}}}\sum_{k=0}^{N_{FFT}-1}\mathbf{Y}[k]e^{-j2\pi\frac{kn}{N_{FFT}}}, \qquad (12)$$

and

$$\begin{aligned}
\mathbf{F}[n] &= [\mathbf{F}_a[n]\ \mathbf{F}_b[n]],\\
\mathbf{F}_a[n] &= \left[vec\left(\check{\mathbf{H}}\left[2\pi\tfrac{n}{N_{FFT}}\right]\mathbf{A}_1\right)\ \ldots\ vec\left(\check{\mathbf{H}}\left[2\pi\tfrac{n}{N_{FFT}}\right]\mathbf{A}_{N_s}\right)\right],\\
\mathbf{F}_b[n] &= \left[j.vec\left(\check{\mathbf{H}}\left[2\pi\tfrac{n}{N_{FFT}}\right]\mathbf{B}_1\right)\ \ldots\ j.vec\left(\check{\mathbf{H}}\left[2\pi\tfrac{n}{N_{FFT}}\right]\mathbf{B}_{N_s}\right)\right],\\
\check{\mathbf{H}}[\omega] &= \textstyle\sum_{l=0}^{L}\mathbf{H}_l e^{-j\omega l}.
\end{aligned} \tag{13}$$

The symbols $\Re(\cdot)$ and $\Im(\cdot)$ represent the real and imaginary parts and $vec(\cdot)$ is the matrix vectorisation operator. The sets $\{\mathbf{A}_i\}$ and $\{\mathbf{B}_i\}$ where $i = 1,2,\ \ldots,\ n_s$ define the OSTBC in such a way that the metric (9) reduces to:

$$\sum_{n=0}^{N_{FFT}-1} \left|\left|\hat{\mathbf{s}}'[n]-\hat{\mathbf{s}}[n]\right|\right|^2, \tag{14}$$

where

$$\hat{\mathbf{s}}'[n] = \frac{\Re\{\mathbf{F}^H[n]\mathbf{z}[n]\}}{\left|\left|\check{\mathbf{H}}\left[2\pi\frac{n}{N_{FFT}}\right]\right|\right|^2}. \tag{15}$$

This is because of the property of OSTBCs that may be expressed as,

$$\Re\left\{\mathbf{F}^H[n]\mathbf{F}[n]\right\} = \left|\left|\check{\mathbf{H}}\left[2\pi\frac{n}{N_{FFT}}\right]\right|\right|^2\mathbf{I}. \tag{16}$$

The effect of the OSTBC is to orthogonalise several MC-CDMA signals spatially. Typically, this technique would be employed to orthogonalise multiple symbols in space and in that case multipath diversity will be lost [4]. However, as can be seen from the simulation results, this is not the case for the proposed system.

3. ANALYTICAL ANALYSIS

3.1 Additive white Gaussian noise

The linear detectability of OSTBC allows the correlation of the CRCCCs to be decoupled from the spatial channel. The MIMO detection criterion is applied to the received signal resulting in the equivalent of n_s direct sequence CDMA received signals of the form

$$\mathbf{r}_i = \tilde{\mathbf{s}}_i + \tilde{\mathbf{n}}_i \quad i = 1,2,\ \ldots,\ n_s, \tag{17}$$

where $\tilde{\mathbf{s}}_i = \mathbf{Cd}_i$ and $\tilde{\mathbf{n}}_i$ is the transformed noise vector. Each of these n_s vectors are then in turn correlated with the CRCCCs using the fast correlation algorithm. This operation is equivalent to the matched filter (MF) receiver, traditionally employed for detection in spread-spectrum systems. It is known that the MF receiver is sub-optimal due to the non-zero correlation coefficients amongst all pairs of codes in the family. Fortunately the CRCCCs do not suffer from this drawback. To illustrate this the correlation of one of the n_s received sequences with one of the flocks from the parent OCC code is investigated in the presence of AWGN:

$$R_{\mathbf{r}_i,\mathbf{c}_k}[n] = R_{\tilde{\mathbf{s}}_i,\mathbf{c}_k}[n] + R_{\tilde{\mathbf{n}}_i,\mathbf{c}_k}[n] \tag{18}$$

$$= d_{k,i}R_{\mathbf{c}_k,\mathbf{c}_k}[n] + \sum_{a=1,\ a\neq k}^{MN} d_{a,i}R_{\mathbf{c}_a,\mathbf{c}_k}[n] + R_{\tilde{\mathbf{n}}_i,\mathbf{c}_k}[n] \tag{19}$$

where $\mathbf{c}_k$ is the kth flock of the CRCCC and $d_{k,i}$ is the kth symbol of the ith data block. The first term in the expression represents the desired symbol (note that the fast correlation algorithm decodes multiple symbols simultaneously, but the result is equivalent to correlation with each flock of the CRCCC individually), the second term represents the multi-user interference (MUI) due to CC between pairs of flocks and the third term represents the noise. Typical CDMA systems incur a performance penalty because the second term in (19) is non-zero. However, in our case the expression reduces to,

$$R_{\mathbf{r}_i,\mathbf{c}_k}[0] = MNd_{k,i} + R_{\tilde{\mathbf{n}}_i,\mathbf{c}_k}[0]. \tag{20}$$

Finally, by dividing by the spreading gain MN in order to normalise the bit energy, the decision variable is expressed as.

$$D_{k,i} = d_{k,i} + R_{\tilde{\mathbf{n}}_i,\mathbf{c}_k}[0]/MN. \tag{21}$$

The bit error probability (BEP) for the kth user may be expressed as,

$$\begin{aligned}
P_e &= \tfrac{1}{2}\left[P\left(\mathcal{N}\left(\sqrt{\varepsilon_b},\tfrac{N_0}{2}\right)>0\right)+P\left(\mathcal{N}\left(\sqrt{\varepsilon_b},\tfrac{N_0}{2}\right)<0\right)\right]\\
&= P\left(\mathcal{N}\left(\sqrt{\varepsilon_b},\tfrac{N_0}{2}\right)>0\right)
\end{aligned}, \tag{22}$$

where ε_b is the bit energy and BPSK modulation is assumed. The noise term in the decision variable maintains the original one-sided power spectral density N_0 of the AWGN. The well known BPSK BEP is given by,

$$P_e = Q\left(\sqrt{\frac{2\varepsilon_b}{N_0}}\right) \tag{23}$$

where $Q(\cdot)$ is the Gaussian Q-function. This expression is equivalent to that of QPSK in the presence of AWGN.

3.2 Frequency non-selective Rayleigh fading

Equations (21) - (23) illustrate the equivalence of the CRCCCs and BPSK modulation in the presence of noise. It stands to reason that the BEP in frequency non-selective fading would also be equivalent to that of BPSK. Consider to this end the received signal with fading,

$$\mathbf{r}_i = \alpha_i\tilde{\mathbf{s}}_i + \tilde{\mathbf{n}}_i \quad i = 1,2,\ \ldots,\ n_s, \tag{24}$$

where α_i is a Rayleigh distributed random variable. Since the fading coefficient is assumed to be constant over the transmission duration for $\mathbf{s}_i$ the decision variable becomes,

$$D_{k,i} = \alpha_i d_{k,i} + R_{\tilde{\mathbf{n}}_i,\mathbf{c}_k}[0]/MN, \tag{25}$$

and the conditional BEP may be expressed as,

$$P_{e|\alpha_i} = Q\left(\sqrt{\frac{2|\alpha_i|^2\varepsilon_b}{N_0}}\right). \tag{26}$$

In order to derive an expression for the BEP that is not conditioned on α_i the following integral must be performed:

$$P_e = \int_0^\infty P_{e|\alpha_i} p(\gamma_i) d\gamma_i \tag{27}$$

where $\gamma_i = \frac{|\alpha_i|^2 \varepsilon_b}{N_0}$ represents the instantaneous received signal-to-noise ratio (SNR). This is of course for the case where a single transmit antenna and single receive antenna is employed. Combining the MC-CDMA signals with the OSTBCs introduces spatial diversity to the system by orthogonalising $N_{Tx}N_{Rx}$ spatial channels. Since the CRCCCs offer equivalent performance to BPSK (or QPSK) in both AWGN and flat fading channel conditions, we may compare the simulation results to the diversity expression for BPSK,

$$P_e = \left[\frac{1}{2}(1-\mu)\right]^L \sum_{k=0}^{L-1} \binom{L-1+k}{k} \left[\frac{1}{2}(1+\mu)\right]^k \tag{28}$$

where,

$$\mu = \sqrt{\frac{\bar{\gamma}_i}{1+\bar{\gamma}_i}} \tag{29}$$

and $\bar{\gamma}_i$ is the average received SNR.

4. SIMULATION RESULTS

Monte Carlo simulations were performed for three channel types. For all three types, the sampling frequency F_s=1 MHz, K=8, M=8, N=4, FFT size N_{FFT}=MN, code rate R=R_{max} and the bit rate F_{bit}=$2R_{max}F_s$. Firstly, the CRCCCs were employed along with the OSTBCs for various numbers of transmit and receive antennas. The experiment was then repeated with a frequency non-selective Rayleigh (flat) fading channel. Lastly, the system was simulated with two transmit and two receive antennas in the presence of a multipath channel.

4.1 Additive white Gaussian noise

Figure 3 shows the BEP vs SNR per bit performance of the proposed system when transmission took place through an AWGN channel.

It can be observed from the figure that the system achieves equivalent performance to a narrowband uncoded BPSK/QPSK system and is independent of the number of receive antennas. When the rate of the OSTBC is $R_{max} < 1$, or alternatively, $N_{Tx} > 2$, there is a performance loss of approximately 1.25 dB. This is because of the need to normalise the SNR to bit energy-to-noise density ratio (ε_b/N_0). The simulations confirm that the OSTBC orthogonalises the various MC-CDMA signals and illustrates the equivalence of the CRCCC-based system to a narrowband uncoded BPSK/QPSK system. Note that the BEP performance is the same for both single and multi-user operation, due to the total absence of MAI as a result of the perfect orthogonality of the

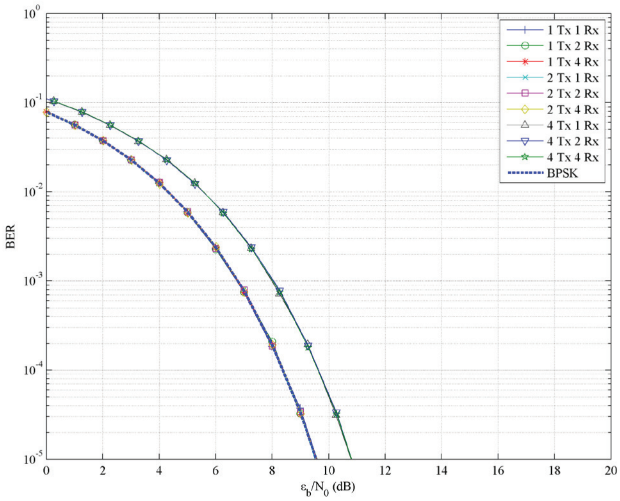

Figure 3: BEP vs SNR of the MIMO MC-CDMA system in an AWGN channel

CRCCC codes. The results are illustrated and discussed in subsequent sections.

4.2 Frequency non-selective Rayleigh fading

The BEP vs. SNR per bit performance results of the proposed system when transmission is through a frequency non-selective Rayleigh fading channel are shown in Figures 4 and 5.

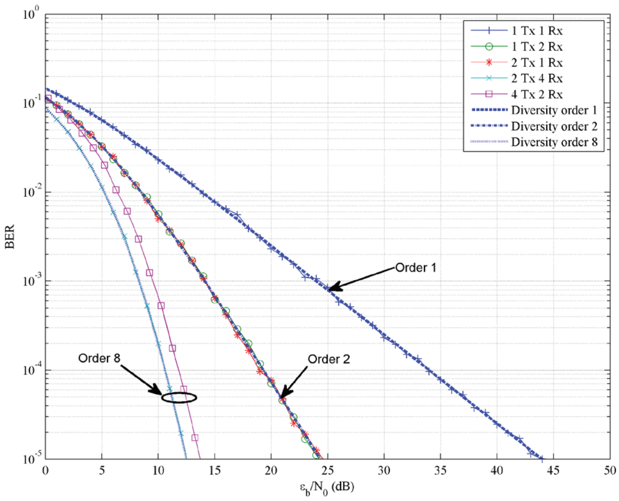

Figure 4: BEP vs. SNR of the MIMO MC-CDMA system in a frequency non-selective Rayleigh fading channel (part 1).

The results have been split into two figures so that they may be easily compared to the analytical curves. The single antenna has for reference purposes been duplicated along with the analytical curve for a diversity order of one. Fig. 4 shows the results for simulations where $N_{Tx}N_{Rx} \in \{1,2,8\}$. It is observed that the system performs identically to that of theoretical narrowband uncoded BPSK/QPSK, again confirming the equivalence. Fig. 5 depicts the results

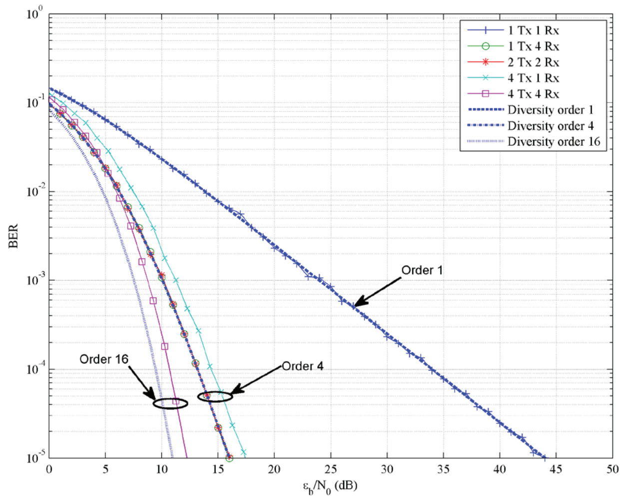

Figure 5: BEP vs. SNR of the MIMO MC-CDMA system in a frequency non-selective Rayleigh fading channel (part 2).

of simulations where $N_{Tx}N_{Rx} \in \{1,4,16\}$. Here similar conclusions as in Fig. 4 may be drawn. Both of the forgoing graphs also display the performance loss of approximately 1.25 dB due to the reduced rate of the OSTBC when $N_{Tx} > 2$.

4.3 *Multipath Rayleigh fading*

Fig. 6 illustrates the performance gain achieved by the proposed CRCCC-based OSTBC CDMA-OFDM system in a multipath channel environment, compared to a conventional narrowband uncoded BPSK/QPSK system. Employing CRCCCs provides a means to achieve multiple access (MA) in a communication system. The figure shows multipath gains in the order of 2.25 dB (L=2) to 3.75 dB (L=6) at a BEP=10^{-5}, where L denotes the number of multipaths in each case.

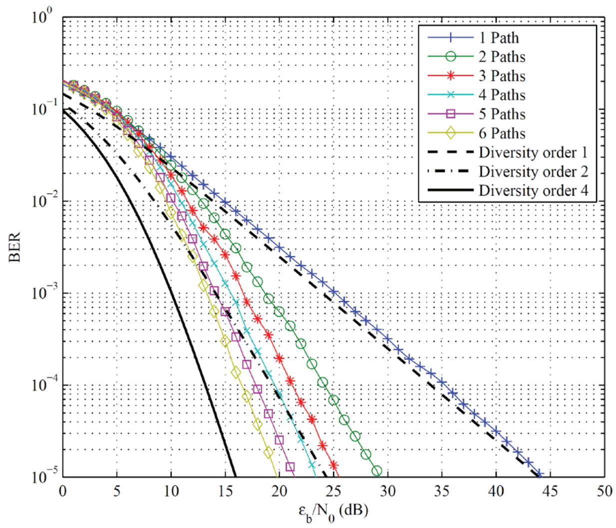

Figure 6: BEP vs. SNR of the MIMO MC-CDMA system in a multipath channel.

5. CONCLUSION

This study illustrated the equivalence of a CRCCC CDMA-OFDM BPSK/QPSK MUI/MAI-free system and a narrowband uncoded BPSK/QPSK system in terms of BEP in the presence of AWGN and frequency non-selective (flat) Rayleigh fading. This has clearly been confirmed by the results obtained from the simulations performed. It is furthermore demonstrated that the use of OCC codes, and more specifically CRCCCs, provides a means to extract otherwise non-exploitable multipath diversity (as in ST-OFDM) in a multiple antenna environment. This is achieved without incurring the expected rate and performance loss of traditional CDMA systems. This paper also highlights the prevention of uncontrolled multi-user interference (MUI) through the use of CRCCCs and illustrates the performance gains achievable with the proposed multi-layered perfectly orthogonal technologies, viz CDMA using CRCCCs, OFDM and OSTBC, while not incurring additional processing cost.

ACKNOWLEDGEMENT

This work is based on the research supported in part by the National Research Foundation of South Africa (Grant reference TP1207183332) and our industry partners Telkom and Bytes Universal Systems. The grantholder acknowledges that opinions, findings and conclusions or recommendations expressed in any publication generated by the NRF supported research are that of the author(s), and that the NRF and our industry partners accept no liability whatsoever in this regard.

REFERENCES

[1] A. Goldsmith, S. A. Jafar, N. Jindal, and S. Vishwanath, "Capacity limits of MIMO Channels," *IEEE JSAC*, vol. 21, no. 5, pp. 684–702, 2003.

[2] G. J. Foschini, "Layered space-time architecture for wireless communication in a fading environment when using multi-element antennas," *Bell Labs Technical Journal*, vol. 1, no. 2, pp. 41–59, 1996.

[3] S. Alamouti, "A simple transmit diversity technique for wireless communications," *IEEE JSAC*, vol. 16, no. 8, pp. 1451–1458, 1998.

[4] E. G. Larsson and P. Stoica, *Space-Time Block Coding for Wireless Communications*. Cambridge University Press, 2003.

[5] L.-L. Yang and L. Hanzo, "Multicarrier DS-CDMA: a multiple access scheme for ubiquitous broadband wireless communications," *IEEE Comm. Mag.*, vol. 41, no. 10, pp. 116–124, 2003.

[6] M. J. E. Golay, "Complementary Series," *IEEE Trans. on Inf. Theory*, vol. 7, no. (2), pp. 82–87, 1961.

[7] H.-H. Chen, *The Next Generation CDMA Technologies*, 1st ed. John Wiley & Sons Ltd., 2007.

[8] A. M. Merensky, L. P. Linde, and J. H. van Wyk, "A multi-dimensional code-division-multiplexed OFDMA modem using cyclic rotated orthogonal complete complementary codes," *SAIEE Africa Research Journal*, vol. 103, no. 2, pp. 94–102, June 2012.

[9] X.-B. Liang, "Orthogonal designs with maximal rates," *IEEE Trans. on Inf. Theory*, vol. 49, no. 10, pp. 2468–2503, 2003.

[10] Z. Lui, L. Guan, and U. Parampali, "New Complete Complementary Codes for the Peak-to-Mean Power Control in MC-CDMA," *IEEE Trans. on Comm*, vol. 62, no.3, pp. 1105–1113, Mar 2014.

SYMBOL ERROR RATE OF GENERALIZED SELECTION COMBINING WITH SIGNAL SPACE DIVERSITY IN RAYLEIGH FADING CHANNELS

A. Essop* and H. Xu**

** School of Engineering, University of Kwa-Zulu Natal, King George V Avenue, Durban, South Africa. E-mail: eaadil3@yahoo.com, aadil3e@gmail.com*
*** School of Engineering, University of Kwa-Zulu Natal, King George V Avenue, Durban, South Africa. E-mail: xuh@ukzn.ac.za*

Abstract: This paper concerns M-ary quadrature amplitude modulation (M-QAM) with signal space diversity (SSD) and generalised selection combining (GSC) in independent and identically distributed (i.i.d) Rayleigh fading channels. The theoretical symbol error rate (SER) performance in i.i.d Rayleigh fading channels for M-QAM with SSD and GSC is derived. The theoretical SER performance of M-QAM with SSD and GSC reception is confirmed via simulations. Thereafter, the diversity gain of M-QAM with SSD and GSC is also analysed. Finally the signal-to-noise ratio (SNR) gap of M-QAM with SSD between selection combining (SC) and maximal ratio combining (MRC) is investigated and validated via simulations.

Keywords: Generalized Selection Combining (GSC), Signal Space Diversity (SSD), M-ary quadrature amplitude modulation (M-QAM).

1. INTRODUCTION

Over the last decade there has been a substantial increase in the number of wireless devices that utilise wireless connectivity with a large bandwidth. This drives a demand to improve wireless communications. In wireless communications, multipath fading is one of the main factors contributing to a decrease in bit error rate (BER) and/or symbol error rate (SER) performance. The application of diversity into a wireless communication system can play a role in improving BER and/or SER performance [1].

The use of rotated signal constellations results in the addition of diversity into a system. This diversity is more commonly known as signal space diversity (SSD) and by adding SSD into a wireless communication system the BER or SER performance can improve [2, 3]. SSD can be thought of as a conventional M-ary quadrature amplitude modulation (M-QAM) constellation, rotated by a certain angle. Rotating the constellation would allow any two constellation points to achieve a maximum number of distinct components (constellation coordinates) [2, 3]. With the addition of component interleaving each of the components is affected by independent fading [3, 4]. As a result, SSD offers superior immunity to noise as there is a low probability that any two points will collapse at the same time [2, 3].

Receiver diversity can also be used to improve BER or SER performance. Receive diversity effectively provides multiple signal paths. This particular diversity technique takes advantage of the low probability that deep fading is unlikely to occur simultaneously on all signal paths [1]. Maximal ratio combining (MRC) and selection combining (SC) are two commonly used techniques which take advantage of multiple paths [5]. MRC offers superior performance at the cost of high implementation complexity since the receiver needs to estimate and combine all paths. SC has a lower implementation complexity since the receiver only needs to estimate all paths and select one path, but the low complexity of SC results in poorer performance. To trade-off between performance and complexity a hybrid selection combining scheme can be used [1]. This hybrid selection combining scheme is more commonly known as generalized selection combining (GSC). In GSC, a subset of receive antennas are selected based on each receiver path's signal-to-noise ratio (SNR). This subset is then combined using MRC. GSC is typically expressed as GSC (L_C, L), where L is the total number of receive antennas and L_C is the number of receive antennas which are being combined ($L_c \leq L$). GSC will result in MRC when $L_c = L$ and similarly SC when $L_C = 1$. GSC ($L_c < L$) offers lower complexity at the cost of performance reductions when compared to MRC. It is typically applied to offer a decrease in complexity whilst still providing BER/SER performance enhancements.

Implementing SSD together with receiver diversity introduces additional diversity and improves BER or SER performance. Receiver diversity with SSD was previously considered in [6], where SSD with MRC in Rayleigh fading channels was investigated. MRC has higher resource requirements when compared to SC, such as power consumption and processing speeds. GSC allows for MRC to be used when required or a suboptimal choice between MRC and SC. This makes GSC more feasible, as it allows the user to select an option to favourably use available resources. For example in portable applications, battery capacity can be a weak point. A system which applies variable GSC, depending on bandwidth load or signal strength can save significant battery power and other system resources.

To the authors' best knowledge M-QAM with SSD and GSC has not been discussed in literature. This motivates us to investigate the SER performance of M-QAM with SSD and GSC reception in this paper. For the purpose of this paper only square M-QAM constellations will be considered.

In a SSD system, the BER or SER depends on the rotation angle of the constellation points. This paper highlights two previously applied methods to derive an optimal rotation angle, namely the minimum product distance (MPD) and the design criterion [6-8]. In this paper the design criterion refers to the criterion of minimum Euclidean distance (MED) on the compound constellation. The main focus of this paper is to extend the approach in [6] to derive a closed form expression for the SER of M-QAM with SSD and GSC reception, which has not been presented in current literature.

A comparison between different methods can help one to decide which method best suits an application. It is vital to know the BER or SER performance difference between the two extreme cases of GSC, as this will allow one to correctly apply a blend between SC and MRC. Diversity analysis between the two extreme cases would theoretically provide insight on the performance difference. There has not been any recent work on the diversity analysis of SSD with MRC and SC. Should the diversity analysis result in no change, it then becomes important to analyse the signal-to-noise (SNR) gap between the two extreme cases.

Previous work showing the SNR gap between SC and MRC for conventional M-QAM has been presented in [9]. However, [9] did not provide any claims as to how SSD would influence this relationship. This also motivates us to present a diversity and SNR gap investigation for M-QAM with SSD and GSC.

The paper is organised as follows: a system model will be presented in section 2. The theoretical SER performance is derived in section 3. In section 4 the diversity gain and SNR gap are analysed. Simulation results and discussions are presented in section 5. Finally section 6 draws the conclusion of the paper.

2. SYSTEM MODEL

Consider a two dimensional M-QAM SSD system as shown in Fig. 1 [6]. The information bits are firstly mapped to two conventional M-QAM symbols. These two M-QAM symbols are then rotated. Finally the rotated M-QAM symbols are interleaved prior to transmission.
This can be expressed mathematically as follows:

Let the original and rotated constellation set be denoted by S and X, respectively. The rotated M-QAM symbols are given by.

$$x_i = s_i R^{\theta}\ ,\ i \in [1\colon 2] \tag{1}$$

where $s_i \in S, s_i = \begin{bmatrix} s_i^I & s_i^Q \end{bmatrix}$ and $x_i \in X, x_i = \begin{bmatrix} x_i^I & x_i^Q \end{bmatrix}$. $(\cdot)^I$ and $(\cdot)^Q$ are the in-phase and quadrature component of a signal, respectively, and the rotating matrix R^{θ} is given by [6]:

$$R^{\theta} = \begin{bmatrix} cos\theta & sin\theta \\ -sin\theta & cos\theta \end{bmatrix} \tag{2}$$

A pair of M-QAM rotated symbols is interleaved prior to transmission. A typical pair of interleaved symbols is given by:

$$u_1 = x_1^I + jx_2^Q \tag{3.1}$$

$$u_2 = x_2^I + jx_1^Q \tag{3.2}$$

The interleaved symbols $u_i, i \in [1\colon 2]$, are transmitted in two subsequent time slots by a single transmit antenna over L receive antennas. Each symbol is transmitted at different time slots; however a pair of symbols needs to be received prior to retrieving the sent data, due to the interleaving, as de-interleaving is required.

Let the received symbols at antenna l and at time slot i be denoted by r_{il}, where $i \in [1\colon 2], l \in [1\colon L]$. r_{il} can be given by:

$$r_{il} = h_{il} u_i + n_{il} \tag{4}$$

where n_{il} is the additive white Gaussian noise (AWGN) with distribution $CN \sim (0, N_0)$. h_{il} is the fading amplitude of the channel which can be modelled according to the Rayleigh distributed random variable with distribution given by equation (5):

$$f(h_{il}) = 2h_{il} \exp(-h_{il}^2) \tag{5}$$

where $E[\, h_{il}^2] = 2\sigma^2 = 1$

Assume that full channel state information is available at the receiver. The symbols pass an in/de-interleaving process followed by GSC at the receiver. Maximum likelihood (ML) detection will be used to estimate the received symbols. A summary of the system can be viewed in Fig. 1.

of CRCCC sequences are maintained. Therefore, by assigning an extended flock of CRCCCs to a single user, it is possible to provide significant increase in rate and spectral efficiency. The grouping of sequences belonging to an extended flock is further motivated by the ability to decode groups of sequences in a single FFT operation. This is achieved by performing fast correlation according to:

$$R_{\mathbf{r},\mathbf{c}_k^0} = \sum_{m=1}^{M} \mathcal{F}^{-1}\left\{\mathcal{F}\{\mathbf{r}^{(m)}\}\cdot\left[\mathcal{F}\left\{\mathbf{c}_{m,k}^0\right\}\right]^*\right\}, \quad (4)$$

where $\mathcal{F}[.]$ and $\mathcal{F}^{-1}[.]$ represents the FFT and IFFT operations, respectively, (.)* denotes the complex conjugate and $\mathbf{r}^{(m)}$ is the mth sequence of received symbols corresponding to the mth element code. Each symbol in the resulting sequence is a sufficient statistic for the detection of the data transmitted using one of the cyclically rotated extension sequences corresponding to the decoding sequence $c_k^0 = [c_{1,k}^0\ c_{2,k}^0\ \ldots\ c_{M,k}^0]$ (i.e., the original parent code of the CRCCC extended flock). The index of the decision variable corresponds to the number of cyclic chip rotations that was performed on the parent flock.

2.2 *Space-time orthogonal frequency division multiplexing*

The CRCCCs have been shown to perform identical to BPSK in a single antenna environment [8]. This is extended to the multi-antenna environment in this paper, by employing the combination of OSTB and space-time-frequency OFDM (STF-OFDM). This approach achieves a diversity order of $N_{Tx}N_{Rx}$, i.e., the product of the number of transmit and receive antennas, as opposed to a diversity order of N_{Rx} in the case of spatial multiplexing. However, there is a compromise to be made: spatial multiplexing yields large capacity gains predicted for multiple antennas when $N_{Rx} \geq N_{Tx}$, but at the cost of an increase in non-linear detection complexity. This is normally not applicable to the forward channel where the mobile mostly uses a single antenna and also has limited computational resources. OSTBs may have reduced capacity, but it is due to this reduction that improved performance is achievable with a single receive antenna. The maximum rate achievable with OSTBCs is [9]:

$$R_{max} = \frac{m+1}{2m}, \quad (5)$$

where $N_{Tx} = 2m-1$ or $N_{Tx} = 2m$. Let $\mathbb{N}$ denote the set of all natural numbers, so that $\{m \in \mathbb{N} | m \leq 8\}$. Taking n_s blocks of data symbols and performing the modulation operations common to single antenna systems, produces a set of vectors

$$\mathbf{s}_i = \Phi\mathbf{W}^H\mathbf{C}\mathbf{d}_i \quad i = 1,2,\ \ldots\ n_s, \quad (6)$$

where $\mathbf{d}_i$ is the ith vector of digitally modulated symbols, $\mathbf{C}$ is a matrix with columns formed by the flocks of the extended CRCCC, $\mathbf{W}$ is the discrete Fourier transform matrix and Φ is a cyclic extension matrix. Taking the rows of the resulting matrix in (6) and mapping them to a sequence of matrices,

$$\{\mathbf{s}_1[n]\ \mathbf{s}_2[n]\ \ldots \mathbf{s}_{n_s}[n]\} \to \{\Phi[n]\} n = -CP, -CP+1,\ \ldots,\ N_{FFT}-1, \quad (7)$$

according to an OSTBC, the triply orthogonal modulation is completed. This mapping is mathematically equivalent to mapping the entire OFDM symbols according to the OSTBC before transmission. The index n represents the discrete time index of the MC-CDMA sequences, N_{FFT} is the FFT length (also equal to MN for the system concerned) and CP is the cyclic prefix length. The transmitter is depicted in Figure 1 and the receiver in Figure 2.

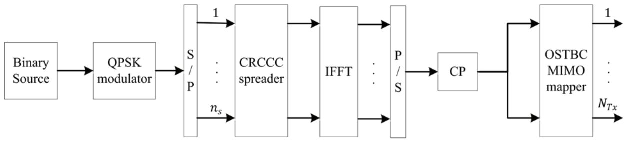

Figure 1: The modulation process performed at the transmitter

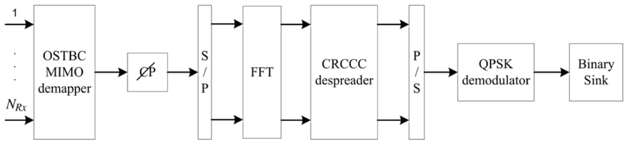

Figure 2: The demodulation process performed at the receiver

The received symbols are described by

$$\mathbf{Y}[n] = \sum_{l=0}^{L}\mathbf{H}_l\Phi[n-l] + \mathbf{N}_\sigma[n] \quad n = 0,1,\ \ldots,\ N_{FFT}-1. \quad (8)$$

The ith column of $\mathbf{Y}[n]$ corresponds to the samples received at time n during the ith OFDM symbol period (n is relative to the beginning of the symbol period), $\mathbf{H}_l$ is the lth matrix channel tap value of a length $L+1$ channel impulse response, and $\mathbf{N}_\sigma[n]$ is a matrix containing *i.i.d.* AWGN samples with zero mean and standard deviation σ_n. With this formulation of the received symbols the detection criterion for the MIMO demapping stage of the receiver is expressed as:

$$\sum_{n=0}^{N_{FFT}-1} ||\mathbf{z}[n] - \mathbf{F}[n]\hat{\mathbf{s}}[n]||^2, \quad (9)$$

where,

$$\hat{\mathbf{s}}[n] = \left[\Re\left[\hat{\mathbf{s}}^T[n]\right]\ \Im\left[\hat{\mathbf{s}}^T[n]\right]\right]^T, \quad (10)$$

$$\mathbf{z}[n] = vec\left(\mathbf{Z}[n]\right), \quad (11)$$

$$\mathbf{Z}[n] = \frac{1}{\sqrt{N_{FFT}}}\sum_{k=0}^{N_{FFT}-1}\mathbf{Y}[k]e^{-j2\pi\frac{kn}{N_{FFT}}}, \quad (12)$$

Table 1: Nearest neighbours

Points	Diagonal Neighbours	Perpendicular Neighbours
Side	2	3
Centre	4	4
Corner	1	2

Based on $P[X_A \rightarrow X_B] = P[X_A \rightarrow X_D]$ and the NN approach, the SER for rotated 16-QAM can be given as [6, 8-11] :

$$P_{SER}^{16-QAM} = 3\,P[X_A \rightarrow X_B] + 2.25\;P[X_A \rightarrow X_C] \quad (7)$$

where $P[X_A \rightarrow X_B]$ and $P[X_A \rightarrow X_C]$ are the probabilities of an error occurring due to incorrect detection of a nearby perpendicular and diagonal point, respectively.

The coordinates of X_A and X_B in Fig. 2 and Fig. 3 can be given by:

$$X_A = [3a\ 3a]\begin{bmatrix} cos\theta & sin\theta \\ -sin\theta & cos\theta \end{bmatrix} \quad (8)$$

$$X_B = [a\ 3a]\begin{bmatrix} cos\theta & sin\theta \\ -sin\theta & cos\theta \end{bmatrix} \quad (9)$$

Then the Euclidean distance between X_A and X_B, and X_A and X_C can be evaluated as follows:

$$d_{A\rightarrow B}^2 = 4a^2h_I^2\cos^2\theta + 4a^2h_Q^2\sin^2\theta \quad (10)$$

$$d_{A\rightarrow C}^2 = 4a^2h_I^2\,(1 - sin2\theta) + 4a^2h_Q^2(1 + sin2\theta) \quad (11)$$

where h_I and h_Q are the in-phase and quadrature components fading gain.

Given h_I and h_Q the conditional PEP of choosing X_B given that X_A was transmitted is given by [17]:

$$P\left[X_A \rightarrow X_B\,|h_I,\,h_Q\right] = \mathrm{Q}\left(\sqrt{\frac{d_{A\rightarrow B}^2}{2N_0}}\right) \quad (12)$$

where $Q(\cdot)$ is the Gaussian Q function.

Substituting equation (10) into (12) results in the following:

$$P\left[X_A \rightarrow X_B\,|\gamma_I\,,\gamma_Q\right] = Q\left(\sqrt{\frac{1}{5}\left(\gamma_I\,\cos^2\theta + \gamma_Q\,\cos^2\theta\right)}\right) \quad (13)$$

Similarly we have

$$P\left[X_A \rightarrow X_C\,|\gamma_I\,,\gamma_Q\right] = Q\left(\sqrt{\frac{1}{5}\left(\gamma_\mathrm{I}\,(1-\sin2\theta)\,+\gamma_\mathrm{Q}\,(1+\sin2\theta)\right)}\right) \quad (14)$$

where $\gamma_I = \bar{\gamma}\sum_{k=1}^{L_c}\tilde{h}_{1k}^2$ and $\gamma_Q = \bar{\gamma}\sum_{k=1}^{L_c}\tilde{h}_{2k}^2$. $k \in [1{:}L_c]$. $\tilde{h}_{ik}, i \in [1{:}2]$, are the L_c largest channel gain of $h_{il},\ l \in [1{:}L]$. L denotes the total number of receive antennas and $\bar{\gamma} = E[\gamma_I] = E[\gamma_Q]$ denotes the average SNR and $E[\cdot]$ denotes expectation.

The error probability $P[X_A \rightarrow X_B]$ can be obtained by averaging the conditional PEP in equation (13) over independent fading channels for GSC reception as shown in equation (15):

$$P[X_A \rightarrow X_B] = \int_0^\infty\int_0^\infty P\left[X_A \rightarrow X_B\,|\gamma_I\,,\gamma_Q\right] f_{\gamma_I}(\gamma_I) f_{\gamma_Q}(\gamma_Q)\mathrm{d}\gamma_I\mathrm{d}\gamma_Q \quad (15)$$

where f_{γ_I} and f_{γ_Q} are the PDFs for GSC in Rayleigh fading channels given by the following expression [5, Eq. 9.325].

$$f(\gamma) = \binom{L}{L_C}\left[w_1 + \frac{1}{\bar{\gamma}}w_2\,w_3\right] \quad (16)$$

where

$$w_1 = \frac{\gamma^{L_c-1}e^{-\gamma/\bar{\gamma}}}{\bar{\gamma}^{L_c}(L_c-1)!}$$

$$w_2 = \sum_{l=1}^{L-L_c}(-1)^{L_c+l-1}\binom{L-L_c}{l}\left(\frac{L_c}{l}\right)^{L_c-1}$$

and $w_3 = e^{-\frac{\gamma}{\bar{\gamma}}}\left(e^{-\frac{l\gamma}{L_c\bar{\gamma}}} - \sum_{m=0}^{L_c-2}\frac{1}{m!}\left(-\frac{l\gamma}{L_c\bar{\gamma}}\right)^m\right)$.

The PDF of GSC can be used to generate the PDF of SC, GSC $(1, L)$ and MRC, GSC (L, L) which are given by [5] respectively as:

$$f_{SC}(\gamma) = \frac{L}{\bar{\gamma}}\sum_{l=0}^{L-1}(-1)^l\begin{bmatrix} L-1 \\ l \end{bmatrix}e^{-\gamma\frac{1+l}{\bar{\gamma}}} \quad (17.1)$$

$$f_{MRC}(\gamma) = \frac{\gamma^{L-1}\,e^{-\frac{\gamma}{\bar{\gamma}}}}{\bar{\gamma}^L\,(L-1)!} \quad (17.2)$$

In order to evaluate and simplify the expression in equation (15), the Q function in equation (12), needs to be simplified. This is accomplished with the trapezoidal approximation of the Q function presented in [11]. The trapezoidal approximation of the Q function is given as follows [11]:

$$Q(x) = \frac{1}{2n}\left(\frac{1}{2}e^{-\frac{x^2}{2}} + \sum_{k=1}^{n-1}e^{-\frac{x^2}{2\sin^2\theta_k}}\right) \quad (18)$$

where $\theta_k = \frac{k\pi}{2n}$, n is the upper limit for the summation.

To simplify the integral found in equation (15), a moment generating function (MGF) will be used. The MGF of the output SNR is given by [5]:

$$M_y(s) = \int_0^\infty f_\gamma(\gamma)\, e^{s\gamma}\, \mathrm{d}\gamma \qquad (19)$$

The MGF for GSC can be derived using equation (18) and (19). For Rayleigh channels this is evaluated as [18, 5- Page 383 Eq. 9.321]:

$$M_{\gamma GSC}(s) = (1 - s\bar{\gamma})^{-L_C+1} \prod_{l=Lc}^{L} \left(1 - \frac{s\bar{\gamma}L_C}{l}\right)^{-1} \qquad (20)$$

Using equation (13) and simplifying (15) with the Q approximation - equation (18), results in the following:

$$P[X_A \to X_B] = \int_0^\infty \int_0^\infty \{\Delta_1 + \Delta_2\} f_{\gamma_I}(\gamma_I) f_{\gamma_Q}(\gamma_Q) \mathrm{d}\gamma_I \mathrm{d}\gamma_Q \qquad (21)$$

where $\Delta_1 = \frac{1}{2n}\left(0.5\, e^{-\frac{0.2(\gamma_I \cos^2\theta + \gamma_Q \sin^2\theta)}{2}}\right)$,

and $\Delta_2 = \frac{1}{2n}\sum_{k=1}^{n-1} e^{-\frac{0.2(\gamma_I \cos^2\theta + \gamma_Q \sin^2\theta)}{2\sin^2\theta_k}}$.

From equation (20), the error probability equation (21), $P[X_A \to X_B]$ can be further simplified as:

$$P[X_A \to X_B] = \frac{1}{4n} M_{\gamma GSC}\left(-\frac{cos^2(\theta)}{\varepsilon_m}\right) M_{\gamma GSC}\left(-\frac{sin^2(\theta)}{\varepsilon_m}\right) + \frac{1}{2n}\sum_{k=1}^{n-1} M_{\gamma GSC}\left(-\frac{cos^2(\theta)}{\varepsilon_m \sin^2(\theta_k)}\right) M_{\gamma GSC}\left(-\frac{\sin^2(\theta)}{\varepsilon_m \sin^2(\theta_k)}\right) \qquad (22)$$

where $\varepsilon_m = 10$ and ε_m is the average expected energy per symbol and this is calculated based on the M-QAM constellation size.

Similarly, $P[X_A \to X_c]$ is derived as:

$$P[X_A \to X_c] = \frac{1}{4n} M_{\gamma GSC}\left(-\frac{1+sin2\theta}{\varepsilon_m}\right) M_{\gamma GSC}\left(-\frac{1-sin2\theta}{\varepsilon_m}\right) + \frac{1}{2n}\sum_{k=1}^{n-1} M_{\gamma GSC}\left(-\frac{1+sin2\theta}{\varepsilon_m sin^2(\theta_k)}\right) M_{\gamma GSC}\left(-\frac{1-sin2\theta}{\varepsilon_m\, sin^2(\theta_k)}\right) \qquad (23)$$

Substituting equation (22) and (23) directly into equation (7) results in the SER for 16-QAM with SSD and GSC. A similar approach is used to evaluate the SER for other M-QAM constellation sizes. The perpendicular and diagonal neighbours for each constellation size are used to evaluate the coefficients of $P[X_A \to X_B]$ and $P[X_A \to X_c]$ which are denoted by A_M and B_M respectively and can be found in Table 2.

Table 2: Values for A_M, B_M and ε_m

Constellations	A_M	B_M	ε_m
4 - QAM	2	1	2
16 - QAM	3	2.25	10
64 - QAM	3.5	3.0625	42
256 - QAM	3.75	3.5156	170

The values for A_M and B_M in Table 2 are verified using the expression found in [16, Table 2] for squared M-QAM constellations.
A more general expression for GSC M-QAM SSD can be written as

$$P_{SER}^{M-QAM} = A_M P[X_A \to X_B] + B_M P[X_A \to X_c] \qquad (24)$$

where A_M, B_M and ε_m vary with each M-QAM constellation and are tabulated in Table 2.

4. DIVERSITY ORDER AND SNR GAP

Diversity analysis gives an indication of the diversity of a system. The amount of diversity effects the overall SER/BER performance of a communication system. The diversity order has not been analysed for M-QAM with SSD in current literature. This section will investigate the analysis of diversity and SNR gap between the extreme cases of GSC which are SC and MRC.
This paper will show that GSC *($L_c \neq L$)* achieves the same diversity order as MRC for conventional M-QAM due to the total available receive antennas remaining constant. However, the SER performance of GSC is worse than MRC [9]. There is in fact an SNR gap between GSC and MRC even in conventional M-QAM. The SNR gap between SC and MRC in Nakagami-m fading channels has been investigated in [9]. However, it has not commented on the SNR gap between SC and MRC for M-QAM with SSD. In this section the same approach proposed in [9] will be used to investigate the SNR gap for M-QAM with SSD.

4.1 Diversity order

Consider that the fading is independently and identically distributed with the same fading parameters and the same average SNR, $\bar{\gamma}$ for all L_c channels. For the purpose of this paper the diversity gain for the extreme cases will be derived. The extreme cases are $L_c = 1$ and $L_c = L$, which are the SC and MRC cases, respectively.
The diversity order denoted by G, of a communication system can be defined as the slope of its error probability $P_e(SNR)$ in log-scale, at values where the SNR tends to infinity [19]. This can be evaluated as follows [19]:

$$G = \lim_{\bar{\gamma}\to\infty} \frac{log[P_e(\bar{\gamma})]}{log(\bar{\gamma})} \qquad (25)$$

An approximation will be used to simplify the expression for diversity order for both MRC and SC whilst maintaining a high level of accuracy. The SER is largely dependent on the MED. At high SNR values the perpendicular closest neighbours have a greater influence on the overall SER performance when compared to diagonal neighbours. The SER derived in section 3, equation (24) can be approximated to:

$$P_{SER}^{M-QAM} \cong A_M P[X_A \to X_B] \qquad (26)$$

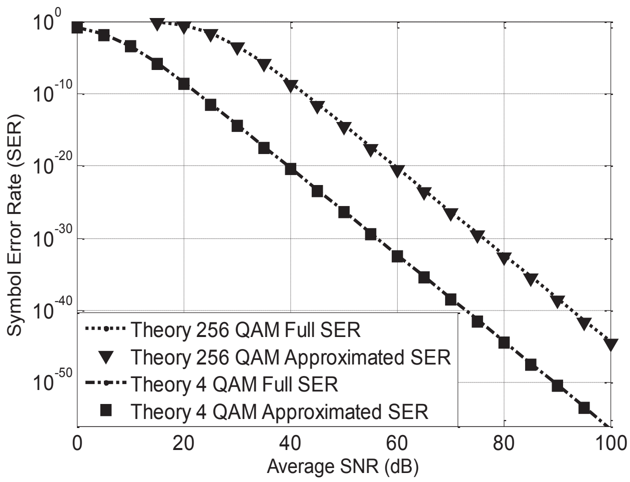

Fig. 4: SNR difference between using full SER expression and $P[X_A \rightarrow X_B]$ only for 4 and 256-QAM

The accuracy of equation (26) is questionable at first glance therefore warranting the validation of its accuracy. As per the definition of diversity order, it is evaluated as the SNR approaches infinity and it is for that reason that the above approximation maintains a high level of accuracy when calculating the diversity order. In order to quantify the error introduced using the approximation, the accuracy of equation (26) is validated by comparing it directly with its accurate counterpart, equation (24). Fig. 4 shows a direct comparison of the theoretical results between equation (24) and (26) for 4-QAM and 256-QAM SSD with GSC(3,3).

Fig. 4 illustrates that the SER approximation is constellation size independent at high SNR. Both 4-QAM and 256-QAM exhibit a similar SNR gap between equation (24) and (26), at the same respective SER. Due to the approximation being constellation size independent the accuracy errors can be evaluated for 4-QAM and hence all values of M-QAM. More details are illustrated in Fig 5.1 and Fig. 5.2, which show the performance differences for 4-QAM at low and high SNR values, respectively. The difference in SNR between equation (24) and (26) change very little across SNR values, but the percentage error would increase as the SNR values tend to zero and decrease rapidly as the SNR values tend to infinity. Fig. 5.1 and Fig. 5.2 reveal an error of 0.3 dB and 0.4 dB when operating at 18 dB and 98 dB respectively.

$$\frac{0.3\ dB}{18dB} = 1.67\ \% \tag{27.1}$$

$$\frac{0.4\ dB}{98\ dB} = 0.48\ \% \tag{27.2}$$

Equation (27.1) – (27.2) prove that the approximation, equation (26) is valid and holds a high level of accuracy as depicted by the miniscule error at low SNR values and even smaller error at higher SNR values. Therefore for diversity order calculations the effects of $P[X_A \rightarrow X_C]$ can be neglected.

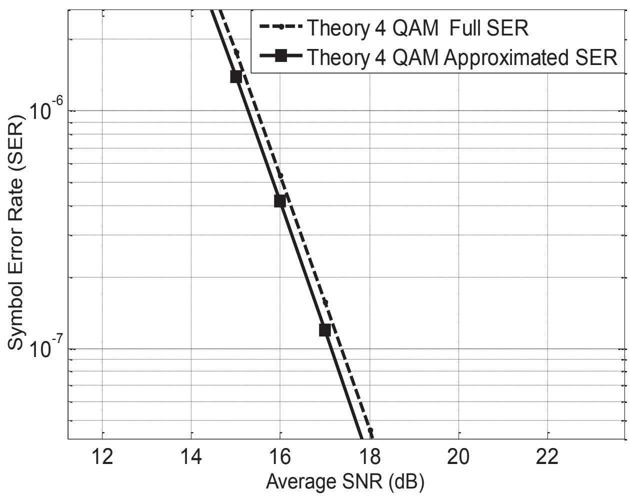

Fig. 5.1: SNR difference between using full SER expression and $P[X_A \rightarrow X_B]$ for 4-QAM at low SNR values

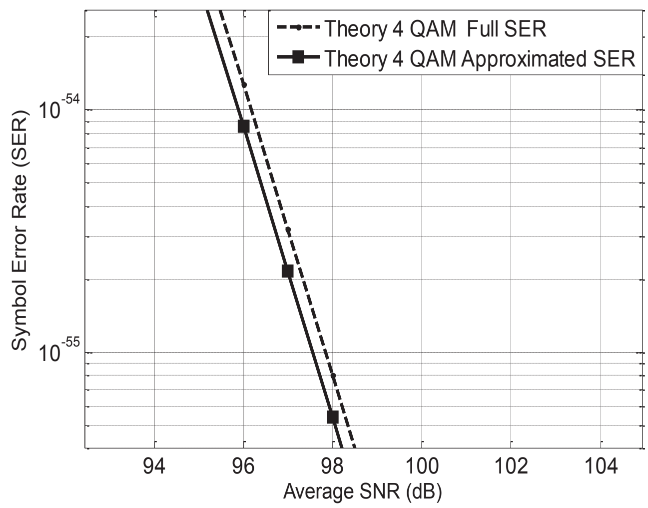

Fig. 5.2: SNR difference between using full SER expression and $P[X_A \rightarrow X_B]$ only for 4-QAM at high SNR values.

Using the approximation presented in equation (26) the diversity order for GSC $(1, L)$ and GSC (L, L) will be evaluated for L receive antennas.
The Q function in equation (15) will be simplified using the Chernoff bound found in [20] in order to simplify the diversity order calculations:

$$Q(x) \leq e^{-\frac{x^2}{2}} \tag{28}$$

Equation (15) can be approximated using this upper bound as:

$$P[X_A \rightarrow X_B] \leq$$
$$\frac{1}{2}\int_0^{\infty}\int_0^{\infty} e^{-\frac{\frac{1}{5}\left(\gamma_I \cos^2\theta + \gamma_Q \sin^2\theta\right)}{2}} f_{\gamma_I}(\gamma_I) f_{\gamma_Q}(\gamma_Q) \mathrm{d}\gamma_I \mathrm{d}\gamma_Q \tag{29}$$

The effect introduced by the Chernoff upper bound approximation becomes negligible as the SNR approaches infinity when evaluating the diversity order.

Substituting the PDF for SC, equation (17.1) into equation (29) results in the following:

$$P[X_A \rightarrow X_B] \leq \frac{1}{2}\int_0^{\infty} e^{-\frac{1}{5}\gamma_I \cos^2\theta} \times \frac{L}{\bar{\gamma}}\sum_{l=0}^{L-1}(-1)^l \begin{bmatrix} L-1 \\ l \end{bmatrix} e^{-\gamma_I \frac{1+l}{\bar{\gamma}}} \mathrm{d}\gamma_I \times \int_0^{\infty} e^{-\frac{1}{5}\gamma_Q \sin^2\theta} \times \frac{L}{\bar{\gamma}}\sum_{l=0}^{L-1}(-1)^l \begin{bmatrix} L-1 \\ l \end{bmatrix} e^{-\gamma_Q \frac{1+l}{\bar{\gamma}}} \mathrm{d}\gamma_Q \tag{30}$$

This can be simplified as follows:

$$P[X_A \rightarrow X_B] \leq \frac{L!}{2}\left(\frac{1}{\prod_{l=1}^{L}\left(l+\frac{\bar{\gamma}}{5}\cos^2\theta\right)}\right) \times \left(\frac{L!}{\prod_{l=1}^{L}\left(l+\frac{\bar{\gamma}}{5}sin^2\theta\right)}\right) \tag{31}$$

Using the SER approximation, equation (26) and simplifying the expression above using the upper bound of $P[X_A \rightarrow X_B]$ found in equation (30) results in equation (32):

$$P_{SER} \approx A_M\, P[X_A \rightarrow X_B] = 0.5A_M(L!)^2\left(\frac{1}{\prod_{l=1}^{L}\left(l+\frac{\bar{\gamma}}{5}\cos^2\theta\right)}\right) \times \left(\frac{1}{\prod_{l=1}^{L}\left(l+\frac{\bar{\gamma}}{5}sin^2\theta\right)}\right) \tag{32}$$

Based on the definition of diversity order given in equation (25) and using equation (32) to evaluate the diversity order for GSC $(1, L)$ results in:

$$G_{SC} = \lim_{\bar{\gamma}\rightarrow\infty} \frac{log\left[A_M\, P(X_A \rightarrow X_B)^{M-QAM}\right]}{log(\bar{\gamma})} = -2L \tag{33}$$

Similar to the diversity order derivation of GSC $(1, L)$ we find the diversity order of GSC (L, L) to be:

$$G_{MRC} = \lim_{\bar{\gamma}\rightarrow\infty} \frac{log\left[A_M\, P(X_A \rightarrow X_B)^{M-QAM}\right]}{log(\bar{\gamma})} = -2L \tag{34}$$

The diversity analysis for both extreme cases of GSC results in the same diversity order. This is due to the SER difference becoming negligible as the SNR approaches infinity. This means that the diversity which is gained from all GSC cases will always be the same, as proved by the extreme cases of SC and MRC.

It becomes important to perform a SNR gap analysis between the two extreme cases of SC and MRC to provide insight on the performance differences between SC and MRC and hence GSC. The extreme cases results in a diversity order of $-2L$ each. In the next subsection the SNR gap between SC and MRC will be derived.

4.2 SNR gap

An SNR gap is defined in [9] as the difference in SNR or power that is required for that of SC and GSC to achieve the same SER when the diversity order is the same. At high SNR this gap will be constant since the slope of the SER for both SC and MRC/GSC is invariant. This paper will derive and discuss the SNR gap for SC and MRC. Adopting the approach proposed in [21], the SNR gap can be determined by the following expressions:

$$SER^{MRC}(\bar{\gamma}) = SER^{SC}(\bar{\gamma}\, G_m) \tag{35}$$

where G_m is the SNR gain. The SNR gap in dB can be evaluated as follows:

$$SNR\ gap\ (dB) = 10\log G_m \ \ dB \tag{36}$$

The exact SER equation presented in this paper is of high complexity and hence a closed form approximation is used to solve for the SNR gap. An accurate approximation of the Q function shown in equation (37) [22], will be used to derive the SER of GSC $(1, L)$ and $GSC\ (L, L)$.

$$Q(x) = \frac{1}{12}exp\left(-\frac{x^2}{2}\right) + \frac{1}{4}exp\left(-\frac{2x^2}{3}\right) \tag{37}$$

Furthermore the approximation presented in equation (26) will also be used to simply the SER expressions when evaluating the SNR gap. The accuracy of the SER expressions will not influence the SNR gain - G_m as both the SER of SC and MRC will be evaluated using the same approximations hence having its overall effect on the SNR gain and hence SNR gap nullified.

Using the PDF of SC equation (17.1) and the Q approximation, equation (37) to simplify equation (15) results in the following:

$$P[X_A \rightarrow X_B] = \left(\int_0^{\infty}\left(\frac{1}{12}e^{-\frac{A}{2}} + \frac{1}{4}e^{-\frac{2A}{3}}\right)\frac{L}{\bar{\gamma}}\sum_{l=0}^{L-1}(-1)^l \begin{bmatrix} L-1 \\ l \end{bmatrix} e^{-\gamma_I \frac{1+l}{\bar{\gamma}}} \mathrm{d}\gamma_I\right) \times \left(\int_0^{\infty}\left(\frac{1}{12}e^{-\frac{B}{2}} + \frac{1}{4}e^{-\frac{2B}{3}}\right)\frac{L}{\bar{\gamma}}\sum_{l=0}^{L-1}(-1)^l \begin{bmatrix} L-1 \\ l \end{bmatrix} e^{-\gamma_I \frac{1+l}{\bar{\gamma}}} \mathrm{d}\gamma_I\right) \tag{38}$$

where $A = \frac{2}{\varepsilon_m}\cos^2\theta$ and $B = \frac{2}{\varepsilon_m}\sin^2\theta$

Using the approximation of the SER, equation (26), which neglects the effects of the diagonal points and evaluating the integral in equation (38), gives:

$$SER^{SC} = A_m \cdot P_{SC}^1 \cdot P_{SC}^2 \tag{39}$$

where

$$P_{SC}^1 = \frac{A_m}{12}\left(\frac{L}{\bar{\gamma}}\sum_{l=0}^{L-1}(-1)^l \begin{bmatrix} L-1 \\ l \end{bmatrix} \frac{\bar{\gamma}}{\left(1+l+\frac{A\bar{\gamma}}{2}\right)}\right) + \frac{1}{4}\left(\frac{L}{\bar{\gamma}}\sum_{l=0}^{L-1}(-1)^l \begin{bmatrix} L-1 \\ l \end{bmatrix} \frac{\bar{\gamma}}{\left(1+l+\frac{2A\bar{\gamma}}{3}\right)}\right) \quad \text{and}$$

$$P_{SC}^2 = \frac{A_m}{12}\left(\frac{L}{\bar{\gamma}}\sum_{l=0}^{L-1}(-1)^l \begin{bmatrix} L-1 \\ l \end{bmatrix} \frac{\bar{\gamma}}{\left(1+l+\frac{B\bar{\gamma}}{2}\right)}\right) + \frac{1}{4}\left(\frac{L}{\bar{\gamma}}\sum_{l=0}^{L-1}(-1)^l \begin{bmatrix} L-1 \\ l \end{bmatrix} \frac{\bar{\gamma}}{\left(1+l+\frac{2B\bar{\gamma}}{3}\right)}\right).$$

Similarly we have

$$SER^{MRC} = A_m \cdot P_{MRC}^1 \cdot P_{MRC}^2 \tag{40}$$

where

$$P_{MRC}^1 = \frac{A_m}{12}\left(\left(\frac{1}{\bar{\gamma}A*\frac{1}{2}+1}\right)^L + \frac{1}{4}\left(\frac{1}{\bar{\gamma}A*\frac{2}{3}+1}\right)^L\right) \text{ and}$$

$$P_{MRC}^2 = \frac{A_m}{12}\left(\left(\frac{1}{\bar{\gamma}B*\frac{1}{2}+1}\right)^L + \frac{1}{4}\left(\frac{1}{\bar{\gamma}B*\frac{2}{3}+1}\right)^L\right).$$

By comparing the terms found in equation (39) and equation (40) a simplification can be made. P_{MRC}^1 can be compared directly to P_{SC}^1 and the same applies to P_{MRC}^2 with P_{SC}^2. This simplification can be used to evaluate equation (35) which results in the following

$$\left(\frac{1}{\frac{1}{2}\bar{\gamma}B+1}\right)^L = \left(\frac{L}{\bar{\gamma}}\sum_{l=0}^{L-1}(-1)^l \begin{bmatrix} L-1 \\ l \end{bmatrix} \frac{\bar{\gamma}}{\left(1+l+\frac{BG_m\bar{\gamma}}{2}\right)}\right) \tag{41}$$

Using basic mathematics, from equation (41) the value of G_m can be determined as:

$$G_m = (L!)^{\frac{1}{L}} \tag{42}$$

$$SNR\ gap_{SC-MRC} = \frac{10}{L}\log(L!)\ \ dB \tag{43}$$

The same result was obtained in [21]. This proves that the SNR gap is not related to the rotation angle or constellation size. Thus the SNR gap between a rotated and non-rotated constellation will be equal. Since the SC–MRC SNR gap is angle independent, the SNR gap for other cases of SC–GSC SNR gap is also angle independent. Hence a more general expression for the SNR gap between SC and GSC can be simplified for Rayleigh fading channel directly from [21]:

$$SNR\ gap_{SC-GSC} = \frac{10}{L}\log(L_c!\ \ (L_c)^{L-L_c})\ \ dB \tag{44}$$

where $L_c \leq L$.

The above expression provides the SNR gap for SC to any GSC system for different values of L_c. In [21], the result was derived for non-rotated constellations. Equation (43), the MRC case proved the derivation to be angle independent, therefore equation (44) can be used directly for other GSC values for rotated constellations. Furthermore equation (44) does not contain any angle or constellation size dependent variables; this concisely proves the above statement.

Equation (43) is verified by comparing simulation results with the expressions evaluation. Similarly equation (44) is also verified by simulation results. Both figures can be viewed in the results section.

5. RESULTS

The aim of this section is to validate the theoretical derivations produced in this paper through simulations. The SER performance for rotated constellations of 4, 16, 64 and 256-QAM, at the optimal angle of 31.7°, for $L_c = 1,\ 2, 3$ and $L = 3$ is presented. Please note the extreme cases of MRC and SC at the extreme ends of GSC is also presented in the results, i.e. $L_c = 1$ and $L_c = 3$.

The full SER expression given by (24) is graphed for each case above and compared to simulation results. This will be a means to verify the mathematical expressions as well as compare the simulated system performance with theoretical performance.

The simulated SNR gap of SC and MRC is presented to verify (43). The SNR gap between SC and MRC for $L = 1{:}5$ is verified in the results section via simulations. Thereafter the SNR gap for SC and GSC ($L_c = 1{:}L$) will be graphed for values of $L = 3{,}5$ to verify (44). The SNR gap provides more insight as to the performance compromise when switching from MRC to a specific GSC case. It would allow one to visualise the gain/loss in performance as the L_c value is increased or decreased.

The SER simulations were performed over independent and identically distributed (i.i.d) Rayleigh flat fading channels with AWGN and perfect channel estimation at the receiver.

Fig. 6-9 shows the simulated and theoretical SER performance of SSD systems with $L = 3$ and different L_c values for 4, 16, 64, and 256-QAM, respectively. All exhibit a small difference in performance between the simulation results of the SER and the theoretical SER at low SNR values (SNR < 17dB). If more than a single bit error occurred this will still count as a single SER and hence a slight difference in the theory vs. simulations at low SNR values.

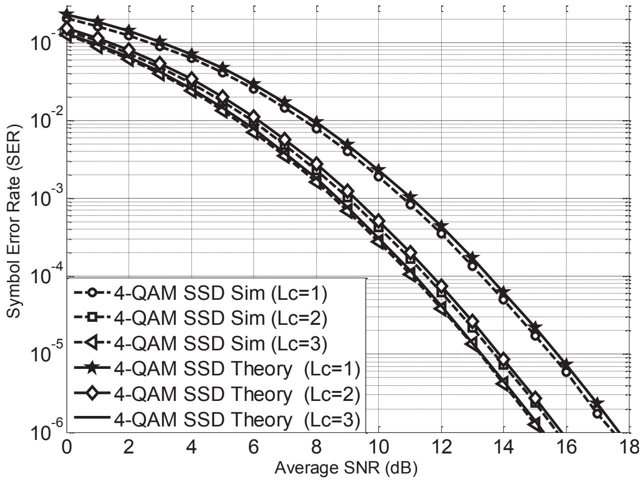

Fig. 6: SER - 4-QAM SSD with GSC in Rayleigh fading channel

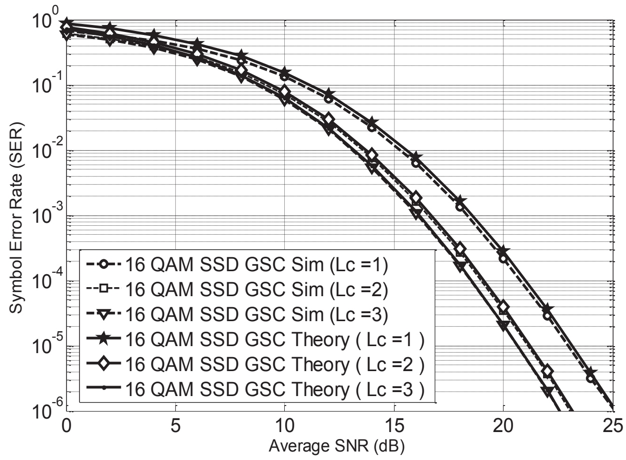

Fig. 7: SER - 16-QAM SSD with GSC in Rayleigh fading channel

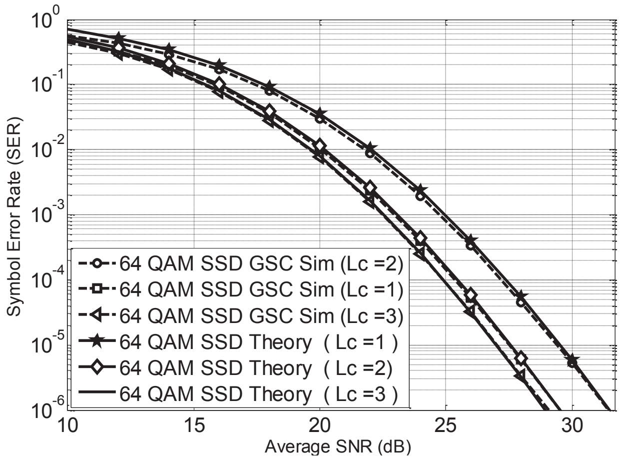

Fig. 8: SER - 64-QAM SSD with GSC in Rayleigh fading channel

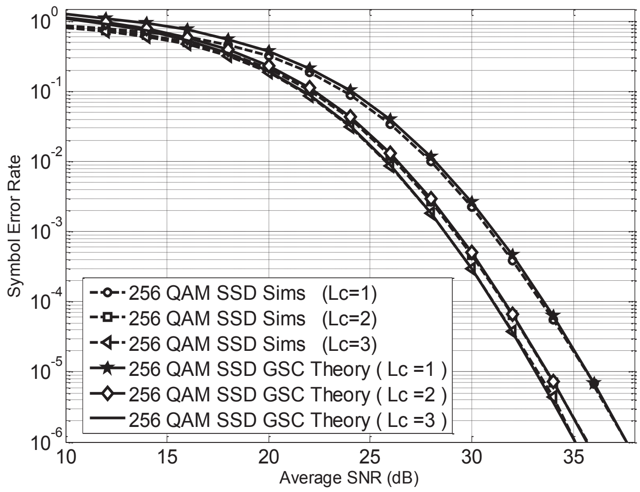

Fig. 9: SER - 254-QAM SSD with GSC in Rayleigh fading channel

At medium to high SNR the theoretical SER and simulation SER, for M-QAM in all GSC cases, closely overlap each other. This difference becomes more prominent as the constellation size increases because higher order constellations produce a greater number of errors at low SNR values and hence in practical applications the lower SNR values are seldom used, making the difference at lower SNR values unimportant.

A performance improvement as the L_c value increases from SC to MRC is also observed. By utilising a GSC scheme a designer can use this information to decide on a suitable L_c value for a device.

5.1 SNR gap relationship

The theoretical SNR gap using equation (43) and (44) are compared to actual simulation results. Due to the fact that the SNR gap is constellation size independent, the simulation results are only analysed for a 16-QAM constellation size at the optimal angle of 31.7 degrees.

Fig. 10 shows the results for the SNR gap which were derived in section 4.2. From Fig. 10 one can observe that the simulation results closely overlap the theoretical results, confirming that the relationship is true. As the number of receive antennas is increased the SNR gap between SC and MRC will increase at the same rate for M-QAM with and without SSD.

The simulations were performed at a constant SER of 10^{-7} for that of SC and MRC and the dB difference is calculated and graphed for a different number of receive antennas. At high SNR values the SER will be very small, thus making it hard to simulate. The relationship which was derived in section 4.2 holds when the SNR is substantially large (SER is low at high SNR). It is then that the SER of SC and MRC will be parallel to each other and hence a constant SNR gap between them. Due to computational requirements and accuracy when simulating at low SER, the SNR gap has been presented for up to five receive antennas.

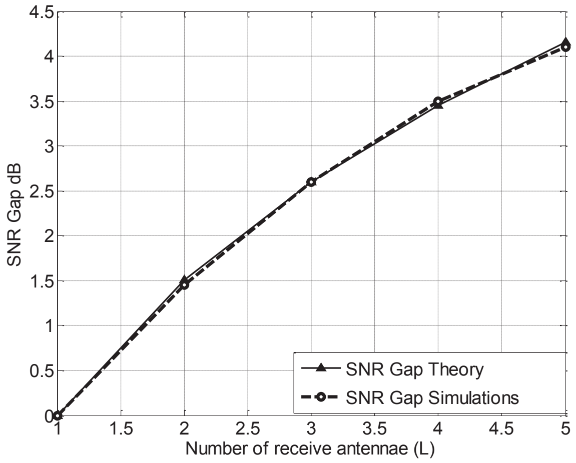

Fig. 10: SNR gap for different L values (MRC- GSC)

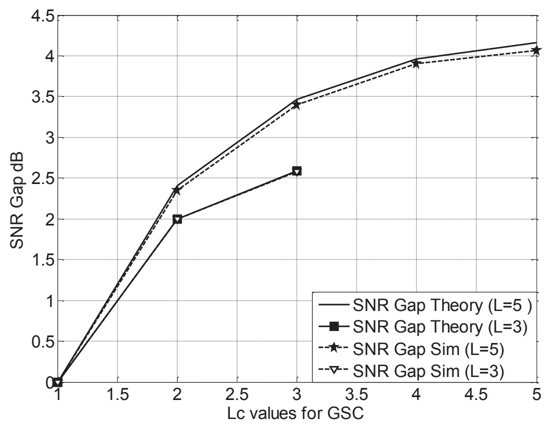

Fig. 11: SNR gap for different L_c values at $L = 3{,}5$

A non-linear curve representing the SNR gap between SC and MRC can be observed in Fig. 10. From the graph one can observe that when L =2 the SNR gap is 1.5 dB but when L =5 the difference is 4.1 dB.

Fig. 11 illustrates the SNR gap for different L_c values when L=5 and L=3. This is to verify equation (44) from [21] is correct. As can be seen that the SNR gap increases as L_c increases. The graph gives a visual representation of the SNR gap which is gained when switching from SC to GSC and then to MRC. As can be realized the relationship is a curve which has the least SNR gap gains when L_c approaches L. For example with L =5 and $L_c = 2$ there is an increase in the SNR gap of 2.4 dB from that of $L_c = 1$ (SC). But when $L_c = 5$ there is an increase of 0.2 dB from that of $L_c = 4$. This is useful information as one is able to realize that even though MRC is the best performing, it might not be worth the extra complexity.

6. CONCLUSION

The use of GSC on a SSD system is presented in this paper as a possible method to improve wireless communication SER performance. The SER performance of SSD using GSC with L receive antennas is derived in Rayleigh fading based on the nearest neighbour approach. A closed form solution based on the MGF function was presented in this paper.

The relationship between applying GSC $(L_c = 1)$ - SC or GSC $(L_c = L)$ - MRC is derived and proved to be positively related to the number of receive antennas. Similarly the power gain between SC and MRC and hence SC and GSC are presented in this paper and proved to be positively related to the number of receive antennas.

GSC proved useful as illustrated by the SNR gap curve and the small increase in performance as L_c approaches L. This was demonstrated by the small increase in the SNR gap as L_c approaches L.

The scheme presented in the paper proved to be successful as it demonstrated that the theoretical performance closely matches simulated performance and the use of GSC with SSD on an M-QAM constellation will increase SER performance.

REFERENCES

[1] H. Xu, "Symbol Error Probability for Generalized Selection Combining," *SAIEE Research Journal*, vol. 100, no. 3, pp. 68-71, Sept 2009.

[2] J. Boutros and E. Vitebro, "Signal Space Diversity: A Power-and Bandwidth- Efficient Diversity Technique," *IEEE Trans. on Info. Theory*, vol. 44, no. 4, pp. 1453 - 1467, July 1998.

[3] J. Kim and I. Lee, "Analysis of Symbol Error Rates for Signal Space Diversity in Rayleigh Fading Channels," in *IEEE International Conf. on Commun.*, Beijing, 2008, pp. 4621 - 4625.

[4] A. Chindapol, "Bit-interleaved coded modulation with signal space diversity in Rayleigh fading," in *Signals, Systems and Computers Conf.* , Pacific Grove, CA, 1999, pp. 1003-1007.

[5] M. S Alouini and M. K. Simon, *Digital Communications over Fading Channels: A Unified Approach to Performance Analysis.*: A Wiley-Interscience Publication, 2000.

[6] Z. Paruk and H. Xu, "Performance Analysis and Simplified Detection for Two - Dimensional Signal Space Diversity," *SAIEE Africa Research Journal*, vol. 104, no. 3, pp. 97-106, September 2013.

[7] S. A. Ahmadzadeh, "Signal space cooperative communication," *IEEE Trans. on wirless Commun.*, vol. 6, no. 4, pp. 1266-1271, April 2010.

[8] S. Jeon, I. Kyung, and M. K. Kim, "Component-Interleaved receive MRC with Rotated Constellation for Signal Space Diversity.," in *IEEE Conf. Veh. Technol.*, Alaska, 2009, pp. 1-6.

[9] N. Kong and L. B. Milstein, "Simple Closed Form Aymtotic Symbol Error Rate of Selection Combining and its Power Loss Compared to the Maximal Ratio Combining over Nakagami M Fading Channels," *IEEE Trans. on Commun.*, vol. 58, no. 4, pp. 1142-1150, April 2010.

[10] S. A. Ahmadzadeh, A. K. Khandani, and S.A. Motahari, "Signal Space Cooperative Communication for Single Relay Model," University of Waterloo, Ontario, Canada., Technical Report 2009.

[11] A. Saeed, T. Quazi, and H. Xu, "Hierarchical modulated quadrature amplitude modulation with signal space diversity and maximal ratio combining reception in Nakagami-m fading channels," *IET Commun.,* vol. 7, no. 12, pp. 1296-1303, Aug 2013

[12] G. Taricco and E. Viterbo, "Performance of component interleaved signal sets for fading channels," *Electronic letters*, vol. 32, no. 13, pp. 1170-1172, April 1996.

[13] I. Guillen, A. Fabregas, and E. Viterbo, "Sphere Lower Bound for Rotated Lattice Constellations in Fading Channels," *IEEE Wireless Commun.*, vol. 32, no. 13, pp. 1170-1172, April 1996.

[14] K. N. Pappi, N. D. Chatzidiamantis, and G. K. Karagiannidis, "Error Performance of Multidimensional Lattice Constellations—Part I: A Parallelotope Geometry Based Approach for the AWGN Channel," *IEEE Trans. on Commun.*, vol. 61, no. 3, pp. 1088-1098, April 2013.

[15] K. N. Pappi, "Error Performance of Multidimensional Lattice Constellations—Part II: Evaluation over Fading Channels," *IEEE Trans. on Commun.*, vol. 61, no. 3, pp. 1099-1110, April 2013.

[16] E. Salahat and I. Abualhaol "Generalized average BER expression for SC and MRC reciever over Nakagami-m fading channels," in *Personal Indoor and Mobile Radio Communications (PIMRC) 24th Int Symposium Conf.* , London, UK , 2013, pp. 3360 - 3365.

[17] M. Salehi and J. G. Proakis, *Digital Communications*, 5th ed. San Diago, USA: McGraw - Hill Higher Education, 2007.

[18] M. S. Alouini and M .K. Simon, "An MGF -Based Performance Analysis of Generalized Selection Combining over Rayleigh Fading Channels," *IEEE Trans. on Commun.*, vol. 48, no. 3, pp. 401-415, March 2000.

[19] H. Dai, H. Zhang, Q. Zhou, and B. L. Hughes, "On the Diversity Order of Transmit Antenna Selection for Spatial for Spatial Multiplexing Systems ," in *Global Telecommunications Conf.* , St. Louis, Missouri , 2005, pp. 1451-1455.

[20] U. Madhow, *Fundamentals of Digital Communication*. United Kingdom : University Press , 2008.

[21] N. Kong, S. Diego, J. C. Corp, and C. Wang, "Simple BER Approximations for Generalized Selection Combining (GSC) over Rayleigh Fading Channels," in *Military Commun. Conf.,* 2006, pp. 1-5.

[22] M. Chiani, D. Dardari, and M. K. Simon, "New exponential bounds and approximations for the computation of each error probability in fading channels," in *IEEE Wireless Commun.*, vol. 2, 2003, pp. 840-845.

PERFORMANCE OF THE LOCAL AVERAGING HANDOVER TECHNIQUE IN LONG TERM EVOLUTION NETWORKS

I.O. Elujide*, O.O. Olugbara, P.A. Owolawi*** and T. Nepal******

Dept. of Information Technology, Durban University of Technology, Durban 4001, South Africa
*Email: *daisel112@yahoo.com, **oludayoo@dut.ac.za, ****nepal@dut.ac.za*
**** Dept. of Electrical Engineering, Mangosuthu University of Technology, Durban, South Africa*
Email: owolawi@mut.ac.za, p.owolawi@gmail.com

Abstract: In this paper, we investigate the performance of an alternative received signal filtering technique based on local averaging to improve the quality of handover decisions in Long Term Evolution (LTE) networks. The focus of LTE-Advance (LTE-A) networks is to provide enhanced capacity and reliability of radio access as well as broadband demand for mobile users. The necessity to maintain quality of service, especially for the delay sensitive data services and applications, has made mobility and handover decisions between the base stations in the LTE networks critical. Unfortunately, several handover decision algorithms in the LTE networks are based on the Reference Signal Received Power (RSRP) obtained as a linear averaging over the reference signals. The critical challenge with the linear averaging technique is that the limited reference signal available in the downlink packet introduces an estimation error. This estimation error is a result of the effects of linear averaging on propagation loss components in eliminating fast-fading from the received signals. Moreover, prompt and precise handover decisions cannot be based on inaccurate measurement. The standardized LTE layer 3 filtering technique is applied to the local averaged layer 1 signal to render it suitable for LTE handover decisions. The local averaging technique produces better handover than the linear averaging technique in terms of the reduced number of handover failures, improved high spectral efficiency and increased throughput, especially for cell-edge users with high speeds. The findings of this study suggest that the local averaging technique enhances mobility performance of LTE-Advance networks.

Key words: averaging, evolution, filtering, handover, signal, network

1. INTRODUCTION

The Long Term Evolution (LTE) standard has evolved to the LTE-Advance in the Third Generation Partnership Project (3GPP) release 12 [1]. The specification of radio access networks was renewed to enhance the capability and reliability of the networks. The capability enhancement was achieved in the LTE networks because of the orthogonal frequency division multiplexing technology employed in the radio interface. The LTE radio interface technology supports a transmission protocol that uses both the Frequency Division Duplex (FDD) and the Time Division Duplex (TDD) mechanisms. The transmission mechanisms in downlink and uplink are based, respectively, on the Orthogonal Frequency Division Multiple Access (OFDMA) and Single Carrier Frequency Division Multiple Access (SC-FDMA) controls. The OFDMA allows for robustness of inter-symbol interference while enabling data and physical layer signals to be concurrently multiplexed. The smallest unit of resources transmitted in one OFDMA symbol that corresponds to one subcarrier is called a *resource element*. A group of resource elements that corresponds to 12 subcarriers in the frequency domain in one OFDMA symbol is called a *resource block*. Some resource elements within a resource block are reserved for special functions such as control signaling, system information broadcast, cell search and synchronization, while the remaining resource elements are used for data transmission.

The reference signals (RSs) which are multiplexed into resource elements are used by a user equipment (UE) to determine the RSRP and Reference Signal Receive Quality (RSRQ) [2]. The RSRP report from a UE is used to estimate the propagation channel condition. Some other methods that could be applied to estimate the channel condition include the exploitation of correlation properties of the channel, the use of deductive knowledge of a parametric model of channel, and blind estimation [3, 4]. The use of RSs for channel estimation is the most common solution because it is simple to implement [3]. However, this simplicity trades off spectral efficiency for tracking variations in the channel and reduces channel estimation accuracy because of the limited number of RSs available within each sub-frame. The limited RSs are the primary reason that the available RSs in adjacent sub-frames are exploited to yield more accurate results [3, 5]. The use of the linear averaging technique over the RSs in the derivation of RSRP limits the capability of the RSRP to make fast, accurate handover decisions for UE, especially when a sudden attenuation in the received signal is experienced by the UE [6, 7]. This is because linear averaging over RSs, necessary for removing the effects of fast-fading, interferes with other propagation loss components such as shadowing and path loss, and hampers the accuracy of the channel estimation.

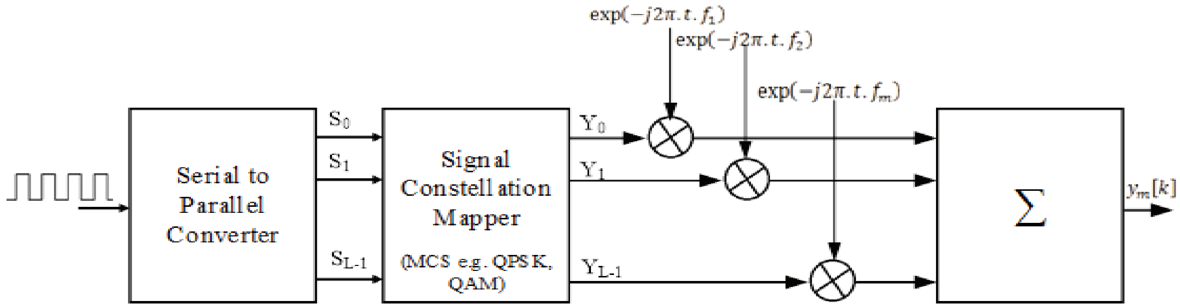

Figure 1: Model of an OFDM transmitter

Several variations of the linear averaging technique have been proposed in literature in an attempt to strike a balance between accuracy and complexity [8]. An alternative technique based on the local averaging can be used to solve the problem arising from the removal of fast-fading from the received signal [7, 9, 10] as well as assist in the protection of the integrity of other propagation loss components. It is particularly germane to note that the accuracy of the estimation made by a UE from the received signal depends largely on the averaging technique employed and has a significant impact on the ability of the handover algorithm to make fast, reliable decisions [11, 12]. Application of local averaging technique in cellular networks was demonstrated in [13]. It should be noted that LTE networks belong to the family of 3GPP technologies. Moreover, layer 1 (L1) filtering is not restrained by the 3GPP standards [14]. The local averaging technique is therefore investigated in LTE networks to achieve fast and reliable handover decisions for delay-sensitive data services, especially for a handover decision occurring at the cell-edge in the presence of multiple interfering signals from neighboring cells.

This paper reports the performance comparison of handover decisions made by using local averaging (L1 filtering) and linear averaging (L1 filtering) of RSRP. Performance is evaluated in terms of throughput, spectral efficiency and average number of handover failures between the UE speeds of 3km/h up to 120km/h [15]. The remainder of this paper is succinctly organized as follows: handover averaging techniques are first discussed; the simulation method and the parameters to compare the performances of the two averaging handover techniques are thereafter presented; and finally, results of the simulation experiments are presented. The paper concludes with a brief statement of achievement.

2. HANDOVER AVERAGING TECHNIQUES

A *handover* is a process of transferring a UE call or a data session from one cell site to another cell without disconnecting the session. The tasks of a handover can be classified appositely into handover measurement, handover processing and handover decision. Herewith we discuss these handover tasks.

2.1 Handover Measurement

The effects of interference on the signal received by a UE in a typical wireless propagation are classified into path loss, shadowing and fast-fading [12, 16]. The corresponding values of these losses, antenna gain and power transmitted from an eNodeB within the operating bandwidth are measured by the UE to facilitate dynamic allocation of network shared resources (E-UTRAN). The UE needs to provide a base station with measurement values of its downlink channel quality, from its cell as well as from neighboring cells, to facilitate the selection of an appropriate cell to connect to the UE. The measurement of UE is necessary for mobility of a user within the E-UTRAN. The UE measurement is performed using RSRP over cell-specific RSs which are multiplexed into the OFDM resource elements and transmitted by some subcarriers. The RS is available to all UEs in a cell for determining a phase reference demodulation of downlink control channels and for generating the Channel State Information (CSI) feedback [3]. Channel estimation is achieved through the transmitted OFDM signal using a filtering technique. Typical implementation of an OFDM transmitter is shown in Figure 1.

The transmitted serial data symbol is passed through a serial to parallel converter to generate L-dimensional parallel data block $S[k]=[S_0[k], S_1[k],\ldots,S_{L-1}[k]]^T$. Each component of the parallel data stream is independently modulated, resulting in a complex vector $Y[k]=[Y_0[k], Y_1[k],\ldots,Y_{L-1}[k]]^T$ used as an input to an Inverse Fast Fourier Transpose (IFFT) system to generate time domain M complex samples using Equation 1:

$$y_m[k]=\frac{1}{\sqrt{M}}\sum_{L=1}^{M} Y_L[k]\exp(2\pi jL\frac{m}{M}) \qquad (1)$$

A conjugate operation is performed at the receiver using an equivalent FFT operation to obtain the frequency domain vector of the transmitted signal. If *y(t)* is the transmitted symbol at time (*t*) where *h(t)* is a continuous time channel impulse and *n(t)* is additive noise, then the received signal, *x(t),* in a multipath environment is represented using the received discrete time OFDM symbol x[k] with cyclic prefix, CP given as:

$$\begin{bmatrix} x_0[k] \\ \vdots \\ x_{M-1}[k] \end{bmatrix} = \begin{bmatrix} y_0[k] & y_{M-1}[k] \cdots y_{M-CP+1}[k] \\ \vdots & \vdots \quad \ddots \quad \vdots \\ y_{M-1}[k] & y_{M-2}[k] \cdots \; y_{M-CP}[k] \end{bmatrix} \bullet \begin{bmatrix} h_0[k] \\ \vdots \\ h_{CP-1}[k] \end{bmatrix} + \begin{bmatrix} n_0[k] \\ \vdots \\ n_{M-1}[k] \end{bmatrix} \tag{2}$$

To simply matters, Equation 2 can be written further as follows:

$$\begin{bmatrix} x_0[k] \\ \vdots \\ x_{M-1}[k] \end{bmatrix} = \mathrm{A} \bullet \begin{bmatrix} h_0[k] \\ \vdots \\ h_{CP-1}[k] \end{bmatrix} + \begin{bmatrix} n_0[k] \\ \vdots \\ n_{M-1}[k] \end{bmatrix} \tag{3}$$

The FFT of matrix A containing the subcarriers with varying peak values produces a diagonal matrix [17, 18]. This implies that the matrix A is equivalent to $F^H YF$ where F is a FFT matrix and Y is a diagonal matrix whose elements are given, respectively, by $F[k] = \frac{1}{\sqrt{M}} \exp(-2\pi L \frac{m}{M})$

and

$Y_m[k] = \frac{1}{\sqrt{M}} \sum_{L=1}^{M} y_L[k] \exp(-2\pi j L \frac{m}{M})$.

The frequency domain representation of the received signal sample $X[k]$, after applying the FFT, is given by Equation 4:

$$\begin{bmatrix} X_0[k] \\ \vdots \\ X_{M-1}[k] \end{bmatrix} = \begin{bmatrix} Y_0[k] & 0 \cdots & 0 \\ \vdots & \vdots \ddots & \vdots \\ 0 & 0 \cdots & y_{M-1}[k] \end{bmatrix} \bullet \begin{bmatrix} H_0[k] \\ \vdots \\ H_{M-1}[k] \end{bmatrix} + \begin{bmatrix} N_0[k] \\ \vdots \\ N_{M-1}[k] \end{bmatrix} \tag{4}$$

The Channel Frequency Response (CFR) denoted by H can be expressed in terms of the Channel Impulse Response (CIR): h as $H = F.h$ [17].

2.2 Handover Processing

The handover processing, also called the L1 filtering as defined by 3GPP, is performed at the LTE physical layer [14]. The purpose of this filtering is to remove the effects of fast-fading in the signal received by a UE. Linear averaging and local averaging are two handover processing techniques studied for this purpose. Linear averaging is the common technique for estimating a channel over an RS. The channel estimation is performed either in the frequency domain or the time domain [3, 8]. The estimate of the channel is then performed using interpolation at several RS positions. For instance, the de-correlation of RS performed in the frequency domain is to determine the Channel Transfer Function (CTF) as given by Equation 5:

$$\hat{v}_i = F_i h + \tilde{v}_i \tag{5}$$

Where i is a value within the interval $(0,\ldots,M)$; M is the number of the available RSs; $F_i h$ is the same as the CFR; and $\tilde{v}$ is the white noise vector. If a generic linear filter D is used in the interpolation scheme for determining an estimate of a channel over a subcarrier at index n then the CTF at subcarrier n can be written as follows:

$$\hat{v}_n = D\hat{v}_i \tag{6}$$

The estimation error of the interpolated CTF of subcarrier n can be expressed as the difference between the actual value and the estimated value as follows:

$$\tilde{v}_n = (F - DF_i)h + D\tilde{v}_i \tag{7}$$

The common linear filters make use of techniques such as Least-Squares (LS) and Minimum Mean-Square Errors (MMSE) [8, 17, 19]. The LS is simple to implement, but it cannot be applied directly to LTE networks because of the ill-conditioning of the matrix inverse on the unmodulated subcarriers [3]. The MMSE produces a more accurate estimate than the LS; however, the MMSE is computationally expensive because it requires second order characteristics of the channel to perform the channel estimation [17].

Local averaging, an alternative technique to the linear averaging technique, is performed as a convolution of the exponential filter with the downlink received signal [7]. This averaging technique is based on the local scattering function that estimates the power spectrum of the measured data using an orthogonal window [9, 20]. The individual estimates of the spectra from the independent window data are aggregated by averaging to obtain a low variance estimate of the channel [21, 22]. If the CFR of the sampled spectra in time and frequency domains is represented by $H[x, y]$, and assuming that the index of each tapped spectral at a specific period corresponds to $w[t, f]$, the relative sampled spectral indices in time and frequency domains are given, respectively, by $x' \in (-\frac{x}{2},\ldots,\frac{x}{2}-1)$ and $y' \in (-\frac{y}{2},\ldots,\frac{y}{2}-1)$.

Where x *is* a time value from the interval of $(0,\ldots,X-1)$ and y *is* a frequency value from the interval $(0,\ldots,Y-1)$. The estimate of the local scattering function at each index corresponding to a discrete sample is given by Equation 8:

$$\xi[w_t, w_f] = \frac{1}{MN} \sum_{p=0}^{MN-1} \left| H^{(Q_p)}[w_t, w_f] \right|^2 \tag{8}$$

Where

$$H^{(Q_p)}[w_t, w_f] = \sum_{x'=\frac{X}{2}}^{\frac{X}{2}-1} \sum_{y'=\frac{Y}{2}}^{\frac{Y}{2}-1} H.Q_p \qquad (9)$$

Where M and N denote, respectively, the total number of tapped spectral used in both the time and frequency domains. The parameter Q_p is the window function equivalent to the exponential filter used for local averaging and N_{av} is the averaging window size. The parameter Q_p is determined as follows:

$$Q_p = \frac{e^{-n/N_{av}}}{1 - e^{-1/N_{av}}} \qquad n = 0,1,2,3,\ldots \qquad (10)$$

2.3 Handover Decision

The UE keeps track of the received signal measurement from its serving cell and neighboring cells in order to recognize the cell with the best signal at the current position. The report of this measurement is sent to the serving eNodeB. Signal attenuation is experienced by the UE as it moves towards the target eNodeB in the strongest interfering cell from the serving eNodeB. In other words, the signal received from the serving eNodeB gradually deteriorates, while that from the neighboring eNodeB (target eNodeB) gradually increases. At a particular distance from the serving eNodeB, the received signal from the serving eNodeB goes below the handover threshold, a predefined value in the eNodeB. The farther a UE moves away from the serving eNodeB, the more the signal attenuates, while there is a corresponding increase in the received signal from the target eNodeB. At a point between the two eNodeBs, the received signal from the serving eNodeB becomes lower than that from the target eNodeB. Figure 2 illustrates the concept of handover margin, the maximum difference between the values of the received signals from two eNodeBs that can be tolerated before triggering a handover decision. The region beyond the handover margin where a handover decision occurs is called the *handover region*. Handover margin is considered in a handover decision before moving a UE to the target eNodeB.

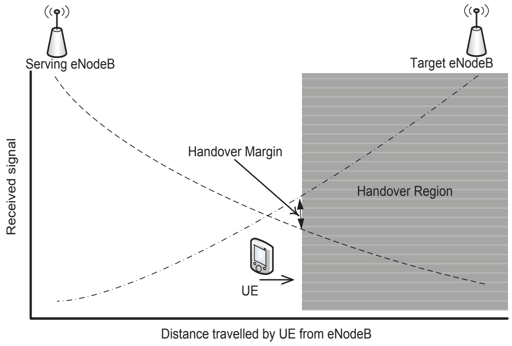

Figure 2: Received signal from two eNodeBs and handover margin

3. SIMULATION

The local filtering handover technique described in the previous section was implemented using the system level simulator [25] as a new module in the LTE networks. The original filtering technique implemented in the simulator is based on linear averaging, while the local averaging technique was implemented as a unique contribution of this study. The linear filtering algorithm implemented in the simulator was to determine the Mutual Information Effectiveness SINR (Signal to Interference plus Noise Ratio) Mapping (MIESM) to serve as a baseline for comparison with the implemented local averaging filtering technique. Two handover decision algorithms were implemented using the two filtering techniques to assess their performances on the overall network. Figure 3 shows a microcell network layout with the hexagonal grid using seven tri-sector sites (cell 0, cell 1 and cell 2) for the simulation experiments. The inter-site distance for each scenario was chosen according to the recommendation of ITU Radio communication (ITU-R) [26]. System bandwidth of 10MHz with 25 resource blocks and 2GHz carrier frequency was used for the simulation experiments.

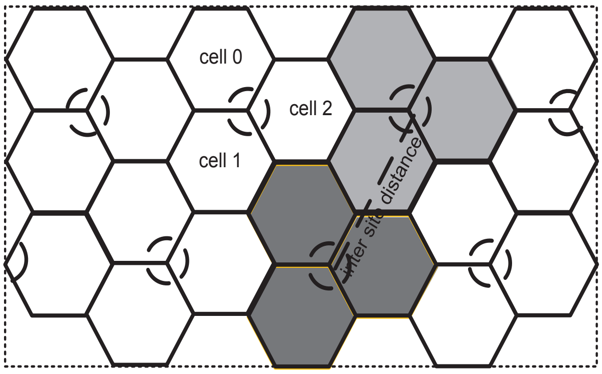

Figure 3: Network layout 7-sites hexagonal grid

The number of UEs at the commencement of the simulation experiments was kept constant. The UEs were uniformly distributed over the network coverage and their directions were randomly chosen from the range of 0^o to 360^o C. Each UE moved with a constant speed throughout the entire simulation. The speed of UE was chosen from 3 km/h, 30 km/h and 120 km/h depending on the scenario [15]. The channel estimation of the signal received at UE was dependent on the path loss, shadow fading and fast-fading [27-29]. The shadow fading with a standard deviation of 8dB and 0 mean was used for the simulation. The details of the simulation parameters are provided in Table 1.

Table 1: Simulation Parameters

PARAMETERS	ASSUMPTION
cell layout	Hexagonal grid (21 eNodeB, 3 sectors per eNodeB)
carrier frequency	2 GHz
resource block (PRB)	50
system bandwidth	10MHz , 180kHz per PRB
eNodeB Tx power	46 dBm
L3 sampling	200TTI
L3 filter coefficient	4
UE per eNodeB	20
UE noise figure	9 dB
packet scheduler	proportional fair
path loss	128.1 + 37.6log10 (R in km) dB
shadow fading	standard deviation = 8dB correlation mean = 0 correlation between eNodeB= 0.5
fast fading	winner channel model

4. RESULTS AND DISCUSSIONS

The results of the simulation experiments performed in this study are discussed in this section. Each simulation experiment was performed for the duration of 500 TTIs (Transmission Time Intervals) to ensure the reliability of results. The system performance is evaluated using the metrics of throughput, spectral efficiency and average number of handover failures for each of the L1 filtering techniques. Performance metrics have been selected to evaluate system and mobility-related performances [30, 31]. The throughput, the total number of the transmitted data packets per second, is measured in units of bits per second (bps) [3, 32]. The spectral efficiency which indicates the amount of spectrum used is the net UE data bit rate transmitted over the operating bandwidth and is measured in bits per second per hertz (bps/Hz) [9].

The values used for the averaging window N_{av} in the local averaging filtering techniques are, respectively, 5, 6 and 8.5 for the corresponding UE operating at standard speeds of 3, 30 and 120 km/h. In Figure 4, the empirical Cumulative Distribution Function (CDF) of the average UEs spectral efficiency at 3km/h is presented. The empirical CDF gives a fair estimate of the UEs CDF and a consistent estimate of the real CDF at any given point [24]. We have observed that a handover algorithm based on the local averaging technique is slightly more spectral efficient than the linear averaging technique in terms of the rate of information transmitted in number of bits per channel. There is no remarkable difference in the spectral efficiency for the 10th to 30th percentile, but the average user spectral efficiency gradually increases from the 40th percentile to about the 95th percentile. Results indicate that the capacity obtained within the cell is higher for average users and peak users when the local averaging filtering technique is used at this speed.

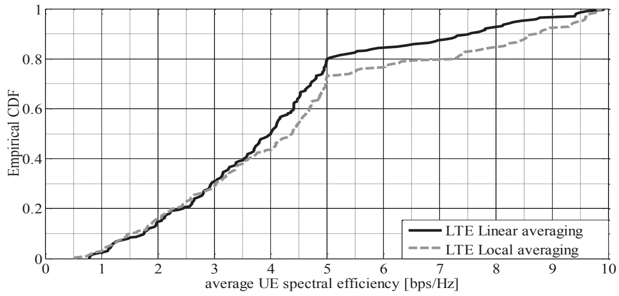

Figure 4: Empirical CDF of average UE spectral efficiency at 3 km/h

Figure 5 presents the results obtained when UEs are moving at 30 km/h in the simulated environment. The empirical cumulative distribution function (empirical CDF) shows that the probability of the average UE spectral efficiency is higher when the local averaging technique was used for a handover decision, suggesting that the number of bits transported within the bandwidth at this speed is higher for the local averaging technique than for the linear averaging technique. It is observed from this result that there is a significant difference between linear averaging and local averaging in terms of the amount of information transmitted by an average user at the 10th percentile to the 90th percentile. The local averaging technique produces higher average user spectral efficiency in bits per second per hertz than the linear averaging technique.

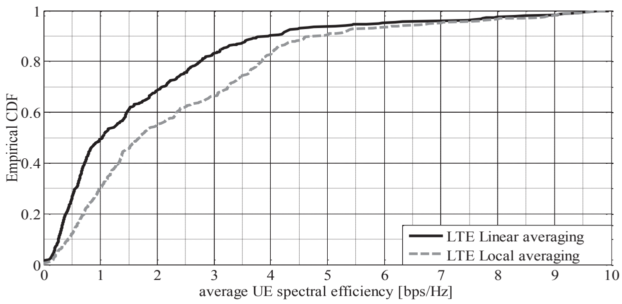

Figure 5: Empirical CDF of average UE spectral efficiency at 30 km/h

The empirical CDF in Figure 6 shows the average user spectral efficiency in bits per second per hertz (bps/Hz) when the UE speed is 120 km/h. The results suggest that the limited frequency spectrum is more utilized when the local averaging technique is employed than when the linear averaging technique is used, meaning that the average number of users accommodated to transmit call simultaneously over the limited spectrum is higher for the local averaging technique, although at about the 95th percentile there is only a slight difference between the performances of the two averaging techniques studied. However, there is a clear indication of the impact of differences in the averaging technique on the spectral efficiency within a cell from the 20th percentile to about the 90th percentile.

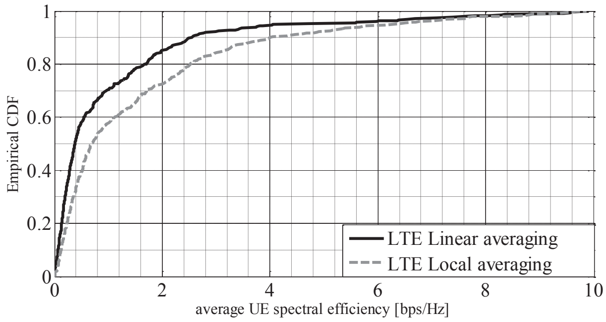

Figure 6: Empirical CDF of average UE spectral efficiency at 120 km/h

Figure 7 shows the results of the peak throughputs based on linear averaging and local averaging techniques. It can be observed from Figure 7 that the effects of these filtering techniques are not noticeably distinguishable at a relatively low speed of about 3 km/h. However, the local averaging technique achieves a better performance in terms of the peak throughput within the cells as the speed increases. It can be determined from Figure 7 that while the effect of the average multiple independent spectra used by the local averaging technique is not clearly visible at low speeds, it gives a better estimate of the channel quality that is achievable by a UE as the speed increases. The improved throughput experienced at higher speeds when the local averaging technique is employed is due to the accuracy of the channel estimate which influences the choice of MCS and increases the data rate achieved by the UE.

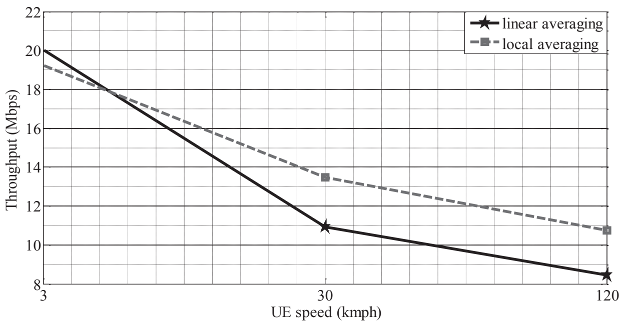

Figure 7: Peak user throughput at different UE speeds

The results of the simulation experiment for the average throughput experienced by a user are shown in Figure 8. The performances of the two filtering techniques are almost the same for the throughput experienced by the UEs. However, the average user throughput experienced when the local averaging technique was employed is slightly higher than that of the linear averaging technique at higher speeds. This is because at low speeds, the rate of change of the radio channel condition experienced by a user is very low, rendering the estimation error of both filtering techniques negligibly small. At higher speeds, however, the radio channel changes at a faster rate and requires a highly accurate filtering technique to keep track of the channel conditions.

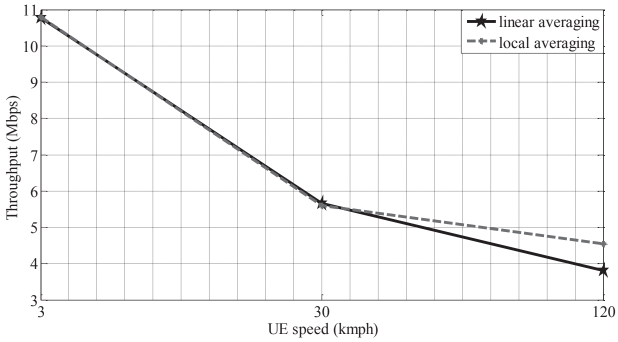

Figure 8: Average user throughput at different UE speeds

Figure 9 presents the results of the cell-edge user throughput at different UE speeds. The cell-edge user throughput performance with the local averaging technique is slightly better than with the linear averaging technique at higher user speeds. Although the cell-edge user throughput for the linear averaging technique is not as high as that of the local averaging technique at low user speeds, the rate of change is not as remarkable as in the local averaging technique. However, the rate of change for the cell-edge throughput based on the local averaging technique is remarkably better than that of the linear averaging technique at higher speeds. This result translates to the perceived QoS experienced by the cell-edge users as the speed increases. The low speed users might experience a sharp change in the QoS when the local averaging technique is used, though this might not be the case for a UE that employs the linear filtering technique. However, the experience is reversed in the case of a UE at higher speeds.

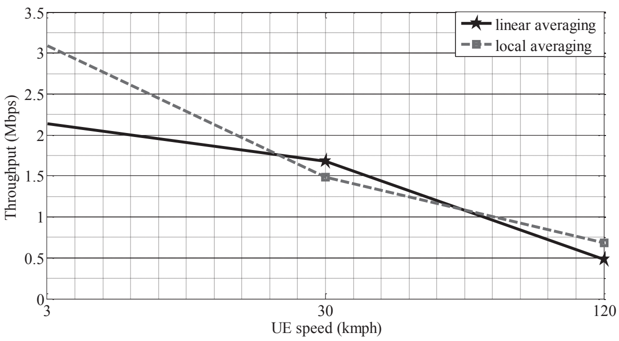

Figure 9: Cell-edge user throughput at different UE speeds

Figure 10 shows the average number of handover failures per UE speed. When the speed is as low as 3 km/h, the rate of handover failures obtained is low for both of the handover filtering techniques. The rate of handover failures due to the linear averaging technique is as low as less than 1.5%. The average number of handover failures observed is also remarkably low for the local averaging technique, with a value less than 1%.

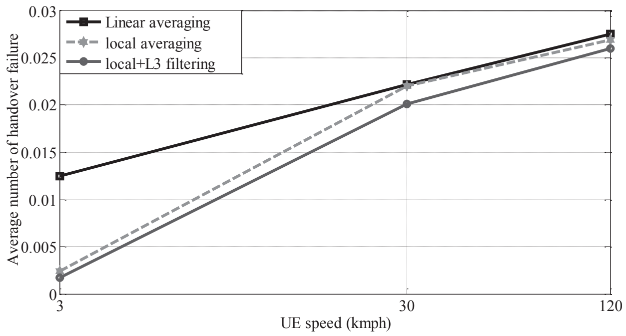

Figure 10: Effect of UE speeds on average number of handover failures

As expected, the average number of handover failures increases as the user speed increases. At higher speeds, the difference in performance of both handover filtering techniques is not particularly significant. However, the effect of L3 filtering on handover failures becomes apparent at a higher speed because L3 algorithms filter output used for triggering a handover decision. In addition, this reduces the L1 estimation error, which becomes higher as user speed increases because of the high uncorrelated nature of the time-varying channel between the UEs and the base stations.

5. CONCLUSION

This paper reports the performance of the local averaging technique in LTE networks. The evaluation metrics of throughput, spectral efficiency and average number of handover failures establish comparison between the local averaging handover technique and the linear averaging handover technique using UEs at various speeds. Performance analysis shows the effect of each handover filtering technique on achievable capacity within the system in terms of spectral efficiency, user throughput and mobility based on the average number of handover failures. The spectral efficiency for pedestrian speed (3 km/h) UEs for the local averaging technique when compared to the linear averaging technique produces, respectively, an increase of 9.1%, 10.8% and 15.1% for cell-edge, average and peak users. From the results obtained at a UE speed of 30 km/h, the comparison between the linear averaging technique and the local averaging technique shows, respectively, increased capacities of about 31.6%, 37.9% and 15.3% for cell-edge, average and peak users. The spectral efficiency at a higher speed of 120 km/h produces, respectively, 52.1%, 68.7% and 40.8% increased capacities for cell-edge, average and peak users. The system throughput for cell-edge users shows, respectively, a 44.8%, 11.7% and 42.8% improvement at UE speeds of 3 km/h, 30 km/h and 120 km/h when the local averaging filtering was employed. The peak user throughput for the linear averaging technique is 4.1% better than that of the local averaging technique. However, the local averaging technique shows, respectively, better performances of about 23.1% and 27.4% at the UE speeds of 30 km/h and 120 km/h.

The results ultimately obtained from the comparison of the average number of handover failures between the two L1 filtering techniques show a significant reduction in the average number of handover failures of about 80.9% for pedestrian users at the speed of 3 km/h using the local averaging technique. The results at the UE speeds of 30 km/h and 120 km/h show, respectively, reductions of about 0.5% and 4.6% in average number of handover failures of the local averaging filtering technique. The application of the L3 filtering in the local averaging technique further improves performance by 26.9%, 8.6% and 0.8% at the UE speeds of 3 km/h, 30 km/h and 120 km/h, respectively.

The results of this study reveal that both handover filtering techniques investigated are suitable for making handover decisions in LTE networks. However, the local averaging technique could ensure the provisioning of higher Quality of Service (QoS) on LTE networks because of the reduced average number of handover failures and improved cell capacity as reflected by the spectral efficiency. As maintaining QoS is particularly germane, diverse sophisticated techniques have been used to maximize the performance of networks for achieving high user throughput. The distribution of user throughput is a clear indicator of QoS. In codicil, it shows data rates experienced by users at different locations within the cell: the 95% user throughput is considered a peak throughput; the mean user throughput is considered a typical data rate achievable within the coverage area of the networks; while the 5% user throughput is termed cell-edge user throughput. The results of user throughput at different speeds as a result of applying two handover filtering techniques have been presented in this paper.

REFERENCES

[1] UMTS Forum: "Mobile Broadband Evolution: the roadmap from HSPA to LTE", white paper from the UMTS Forum, UK, February 2009.

[2] 3GPP: "3rd Generation Partnership Project (3GPP); Technical Specification Group Radio Access Network; Evolved Universal Terrestrial Radio Access (E-UTRA); Physical layer; Measurements (Release 9)", 3GPP TS 36.214 V9.1.0 (2010-03), 2010.

[3] F. Tomatis and S. Sesia: *LTE - The UMTS Long Term Evolution from Theory to Practice*, John Wiley, UK, first edition, chapter 7, pp. 151-164, 2009.

[4] D.T.M. Slock: "Signal processing challenges for wireless communications", in *1st International Symposium on Control, Communication & Signal Processing,* pp. 881-892, 2004.

[5] F. Khan: *LTE for 4G mobile broadband: air interface technologies and performance*, Cambridge University Press, USA, first edition, 2009.

[6] O. Grimlund and B. Gudmundson: "Handoff strategies in microcellular systems", *Proceeding of the 41st IEEE Vehicular Technology Conference,* St. Louis, MO, pp. 505-510, May 1991.

[7] B.L. Mark and A.E. Leu: "Local averaging for fast handoffs in cellular networks", *IEEE Transactions on Wireless Communication,* Vol. 6 No. 3, pp. 866 -874, March 2007.

[8] X. Dai, W. Zhang, J. Xu, J.E. Mitchell and Y. Yang: "Kalman interpolation filter for channel estimation of LTE downlink in high-mobility environments", *EURASIP Journal of Wireless Communication & Networking,* Vol. 2012 No. 1, pp. 1-14, 2012.

[9] J.M. Holtzman and A. Sampath: "Adaptive averaging methodology for handoffs in cellular systems", *IEEE Transactions on Vehicular Technology,* Vol. 44 No. 1, pp. 59-66, February 1995.

[10] R. Vijayan and J. M. Holtzman: "A model for analyzing handoff algorithms [cellular radio]", *IEEE Transaction on Vehicular Technology,* Vol. 42, pp. 351-356, August 1993.

[11] A.H.S. Tamilselvan, and K. Manivannan: "Performance analysis of fast handoff algorithms using Local averaging technique in cellular networks", *Proceeding of the 1st International Conference of Distributed Framework & Applications*, Penang, pp. 183-188, October 2008.

[13] 3GPP: "3rd Generation Partnership Project; Technical Specification Group Radio Access Network; Evolved Universal Terrestrial Radio Access (E-UTRA); Requirements for support of radio resource management (Release 9)", 3GPP TS 36.133 V9.2.0 (2009-12), 2009.

[14] M. Anas, F.D. Calabrese, P.E. Ostling, K.I. Pedersen and P.E. Mogensen: "Performance analysis of handover measurements and layer 3 filtering for UTRAN LTE", *Proceeding of the IEEE 18th International Symposium on Personal, Indoor & Mobile Radio Communications,* Athens, pp. 1-5, September 2007.

[15] 3GPP: "3rd Generation Partnership Project; Technical Specification Group Radio Access Network; Requirements for Evolved UTRA (E-UTRA) and Evolved UTRAN (E-UTRAN) (Release 8)", 3GPP TR 25.913 V8.0.0 (2008-12), 2008.

[16] G. Roche, A.A. Glazunov and B. Allen: *LTE-advanced and Next Generation Wireless Networks: Channel Modelling and Propagation*, John Wiley, Chichester U.K., first edition, 2012.

[17] M. Gudmundson: "Correlation model for shadow fading in mobile radio systems", IET *Electronics Letters,* Vol. 27, pp. 2145-2146, 1991.

[18] J.J. Beek, O. Edfors, M. Sandell, S.K. Wilson and P. Ola Borjesson: "On channel estimation in OFDM systems", *Proceeding of the IEEE 45th Vehicular Technology Conference,* Chicago, IL, pp. 815-819 vol.2, July 1995.

[19] A. Kalakech, L. Brunel, M. Berbineau and D Mottier: "A novel OFDM power based estimation for dynamic channel tracking in downlink LTE", *Proceeding of the IEEE 76th Vehicular Technology Conf*erence, Quebec City, pp. 1-5, September 2012.

[20] G. Matz: "On non-WSSUS wireless fading channels", *IEEE Transaction on Wireless Communications,* Vol. 4 No. 5, pp. 2465-2478, November 2005.

[21] D. J. Thomson: "Spectrum estimation and harmonic analysis", *Proceeding of the IEEE,* Vol. 70 No. 9, pp. 1055-1096, 1982.

[22] D. Percival and A. Walden: *Spectral analysis for physical applications: multitaper and conventional univariate techniques*, Cambridge Univ. Press, New York, 1993.

[23] H. Suzuki: "A statistical model for urban radio propagation", *IEEE Transaction on Communications,* Vol. 25, pp. 673-680, 1977.

[24] M. Anas, F.D. Calabrese, P.E. Mogensen, C. Rosa, and K.I. Pedersen: "Performance evaluation of received signal strength based hard handover for UTRAN LTE", *Proceeding of the IEEE 65th Vehicular Technology Conference,* Dublin, pp. 1046-1050, April 2007.

[25] J.C. Ikuno and M. Taranetz: "Vienna LTE simulators", *System Level Simulators version 1.6r885*, Vienna University of Technology, Austria, 2012.

[26] ITU: "Guidelines for evaluation of radio interface technologies for IMT-Advanced", ITU-R M.2135-1, 2009.

[27] 3GPP: "3rd Generation Partnership Project; Technical Specification Group Radio Access Network; Physical layer aspects for evolved Universal Terrestrial Radio Access (UTRA) (Release 7)", 3GPP TR 25.814 V7.1.0, 2006.

[28] H. Claussen: "Efficient modelling of channel maps with correlated shadow fading in mobile radio systems", *Proceeding of the IEEE 16th International Symposium on Personal, Indoor & Mobile Radio Commun*ications, Berlin, pp. 512-516, September 2005.

[29] L. Hentilä, P. Kyösti, M. Käske, M. Narandzic and M. Alatossava: "MATLAB implementation of the WINNER phase II channel model", [Online]. Available: http://www.ist-winner. org/phase 2 model. html2007, 2007.

[30] J. Gora, A. Gouraud, P. Marsch, N. Gresset, M. Karray, R. Irmer, and T. Svensson: "Scenarios, key performance indicators and evaluation methodology for advanced cellular Systems", *Advanced Radio Interface Technologies for 4G Systems,* EU FP7 INFSO-ICT-247223 ARTIST4G consortium, 2010.

[31] ETSI: "LTE; Evolved Universal Terrestrial Radio Access (E-UTRA); Radio Resource Control (RRC); Protocol specification (3GPP TS 36.331 version 10.5.0 Release 10)", ETSI TS 136 331 V10.5.0 (2012-03), 2012.

[32] H. M. Ramli, K. Sandrasegaran, R. Basukala and L. Wu: "Modeling and simulation of packet scheduling in the downlink long term evolution system", *Proceeding of the 15th Asia-Pacific Conference on Communications,* Shanghai, pp. 68-71, October 2009.

SAIEE AFRICA RESEARCH JOURNAL – NOTES FOR AUTHORS

This journal publishes research, survey and expository contributions in the field of electrical, electronics, computer, information and communications engineering. Articles may be of a theoretical or applied nature, must be novel and must not have been published elsewhere.

Nature of Articles

Two types of articles may be submitted:

- Papers: Presentation of significant research and development and/or novel applications in electrical, electronic, computer, information or communications engineering.
- Research and Development Notes: Brief technical contributions, technical comments on published papers or on electrical engineering topics.

All contributions are reviewed with the aid of appropriate reviewers. A slightly simplified review procedure is used in the case of Research and Development Notes, to minimize publication delays. No maximum length for a paper is prescribed. However, authors should keep in mind that a significant factor in the review of the manuscript will be its length relative to its content and clarity of writing. Membership of the SAIEE is not required.

Process for initial submission of manuscript

Preferred submission is by e-mail in electronic MS Word and PDF formats. PDF format files should be 'press optimised' and include all embedded fonts, diagrams etc. All diagrams to be in black and white (not colour). For printed submissions contact the Managing Editor. Submissions should be made to:

The Managing Editor, SAIEE Africa Research Journal,
PO Box 751253, Gardenview 2047, South Africa.
E-mail: researchjournal@saiee.org.za

These submissions will be used in the review process. Receipt will be acknowledged by the Editor-in-Chief and subsequently by the assigned Specialist Editor, who will further handle the paper and all correspondence pertaining to it. Once accepted for publication, you will be notified of acceptance and of any alterations necessary. You will then be requested to prepare and submit the final script. The initial paper should be structured as follows:

- TITLE in capitals, not underlined.
- Author name(s): First name(s) or initials, surname (without academic title or preposition 'by')
- Abstract, in single spacing, not exceeding 20 lines.
- List of references (references to published literature should be cited in the text using Arabic numerals in square brackets and arranged in numerical order in the List of References).
- Author(s) affiliation and postal address(es), and email address(es).
- Footnotes, if unavoidable, should be typed in single spacing.
- Authors must refer to the website: http: //www.saiee.org.za/arj where detailed guidelines, including templates, are provided.

Format of the final manuscript

The final manuscript will be produced in a 'direct to plate' process. The assigned Specialist Editor will provide you with instructions for preparation of the final manuscript and required format, to be submitted directly to:
The Managing Editor, SAIEE Africa Research Journal, PO Box 751253, Gardenview 2047, South Africa.
E-mail: researchjournal@saiee.org.za

Page charges

A page charge of R200 per page will be charged to offset some of the expenses incurred in publishing the work. Detailed instructions will be sent to you once your manuscript has been accepted for publication.

Additional copies

An additional copy of the issue in which articles appear, will be provided free of charge to authors.
If the page charge is honoured the authors will also receive 10 free reprints without covers.

Copyright

South African Institute for Electrical Engineers (SAIEE)
PO Box 751253, Gardenview, 2047, South Africa
Tel: 27 11 487 3003 | Fax: 27 11 487 3002
E-mail: researchjournal@saiee.org.za | Website: www.saiee.org.za